Bioengineering Notes

June 19, 2001

Contents

1 Biophysics of Nerve and Muscle **1**
1.1 Nerves . . . 1
1.1.1 Cable Theory . . . 1
1.1.2 Ionic Currents . . . 5
1.1.3 The Squid Axon and Hodgkin-Huxley Equations . . . 10
1.2 Muscle . . . 17
1.2.1 Anatomy . . . 17
1.2.2 Properties of muscle contraction . . . 21
1.2.3 Hill model of muscle contraction . . . 27
1.2.4 Sliding filament theory . . . 29
1.2.5 Muscle energetics . . . 33
1.3 Fading Memory Model . . . 38
1.3.1 Finite duration length step . . . 43
1.3.2 Force step response . . . 44

2 Cardiac Electrophysiology **51**
2.1 Cardiac cells . . . 51
2.2 Units . . . 51
2.2.1 Cardiac Ionic Currents . . . 53
2.3 Ion Pumps and Exchanges . . . 54
2.4 diFrancesco-Noble Model . . . 56
2.5 Changes in the action potential . . . 56
2.6 Other membrane models . . . 58
2.6.1 The Beeler-Reuter model . . . 58
2.6.2 The defibrillation Beeler-Reuter model . . . 64
2.6.3 The Luo-Rudy models . . . 68
2.6.4 The Noble 98 model . . . 81

2.7 Simplified models of cardiac cells . . . 82
2.7.1 The polyomial model . . . 82
2.7.2 The FitzHugh-Nagumo model . . . 83
2.7.3 The modified FitzHugh-Nagumo model . . . 84
2.7.4 The van Capelle-Durrer model . . . 85
2.8 The Bidomain Model . . . 88
2.8.1 Definition of the Bidomain Framework . . . 89
2.8.2 Mathematical Derivation of the Bidomain Model . . . 92

3 Electrocardiography **97**
3.1 Cardiac Anatomy and Function . . . 97
3.1.1 Macroscopic description . . . 97
3.1.2 Microscopic description . . . 99
3.1.3 Connective tissue structure . . . 102
3.2 Activation . . . 103
3.2.1 Normal Activation Sequence . . . 104
3.3 History of the ECG . . . 108
3.3.1 The Pathways of Conduction and the ECG . . . 109
3.3.2 Electrodes and Leads . . . 110
3.4 Basic Theory . . . 114
3.5 The Normal ECG . . . 115
3.5.1 The Normal Electrocardiogram . . . 115
3.5.2 The PR Interval . . . 117
3.5.3 The U Wave . . . 121
3.5.4 Some Abnormal ECGs . . . 121
3.6 Usefulness of ECG . . . 125
3.7 Body Surface Potential Mapping (BSPM) . . . 128
3.7.1 BSPM at Halifax, Canada . . . 134
3.7.2 Abnormal Maps . . . 142
3.8 The Forward and Inverse Problems of Electrocardiography . . . 151
3.8.1 Introduction . . . 151
3.9 Theory . . . 153
3.9.1 Transfer Matrices From A Boundary Value Problem Point of View . . . 154
3.9.2 Myocardial Inverse Procedure . . . 160

References **163**

Chapter 1

Biophysics of Nerve and Muscle

1.1 Nerves

1.1.1 Cable Theory

Cable equation

We will consider a nerve as a special case of a conducting cable. Consider a cable as is shown in Figure 1.1.

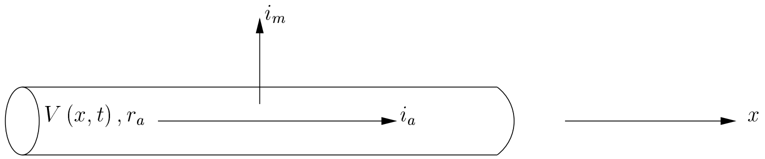

FIGURE 1.1: A standard cable with axial current, i_a (mA), membrane current, i_m (mA/unit length of current), axial resistance r_a (Ω/unit length), and cable potential, $V(x,t)$ (mV).

Ohm's law for the cable is

$$\frac{\partial V}{\partial x} = -r_a i_a$$

and continuity of current is given by

$$i_m = -\frac{\partial i_a}{\partial x}$$

Hence

$$\frac{\partial^2 V}{\partial x^2} = -r_a \frac{\partial i_a}{\partial x} = r_a i_m$$

Now i_m can be broken into a capacitive current, i_c, and an ionic current i_i. For nerves and other biological cables the capacitive current arises as a consequence of a bilipid membrane layer in cells as shown in Figure 1.2.

The capacitive current arises from the separation of charge Q across the bilipid membrane, that is

$$Q = cV = \int_t i_c\, dt \quad \text{or} \quad i_c = c\frac{dV}{dt}$$

where c is the capacitance of the membrane (typically c is about $1\mu\mathrm{F\ cm}^{-2}$ for bilipid membranes).

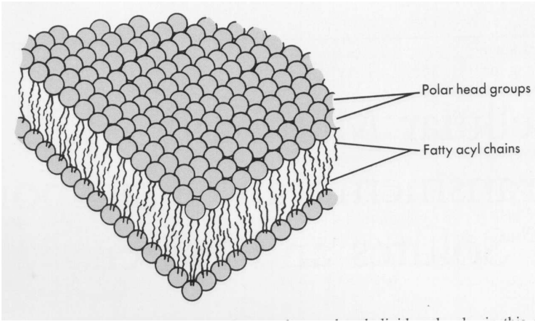

FIGURE 1.2: Structure of a phospholipid bilayer. From Physiology by R.M. Berne and M.N. Levy.

The ionic current component of the membrane current comes about due to the transport of ions through an ionic channel in the membrane as shown in Figure 1.3.

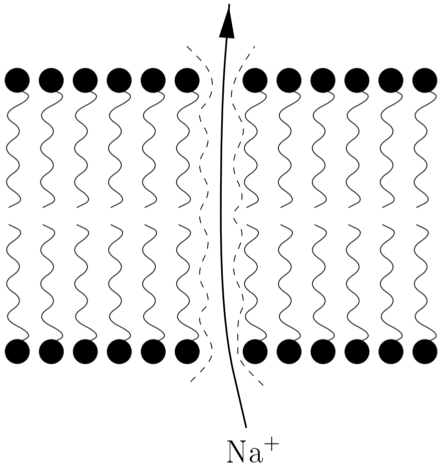

FIGURE 1.3: Ionic channel in a cell membrane.

Substituting the capacitive current we obtain the cable theory equation (Note that i_i would be a leakage current in a normal cable).

$$\frac{1}{r_a}\frac{\partial^2 V}{\partial x^2} = c\frac{\partial V}{\partial t} + i_i \tag{1.1}$$

Two special cases of cable conduction will now be considered:

1. Steady State Passive Current

Consider a steady state passive current given by $i_i = \dfrac{V}{r_m}$. The cable equation now becomes

$$\frac{d^2 V}{dx^2} = \frac{r_a}{r_m}V = \frac{V}{\lambda^2} \quad \text{where} \quad \lambda = \sqrt{\frac{r_m}{r_a}}$$

The solution to this equation is

$$V(x) = Ae^{-x/\lambda} + Be^{x/\lambda} \tag{1.2}$$

Note: for a long cable $B = 0$ and this can be approximated as $V(x) = Ae^{-x/\lambda}$ which gives the relationship shown in Figure 1.4. In this case λ can be interpreted as a *space constant*.

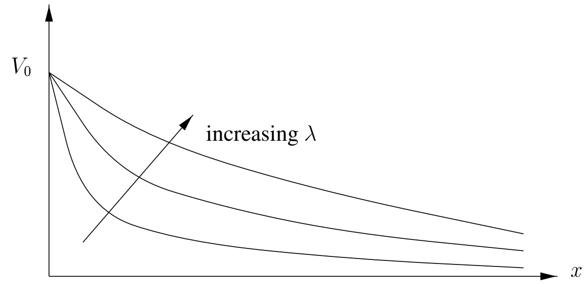

FIGURE 1.4: Voltage relationship for a long cable with a steady state passive leakage current.

2. Constant Conduction Velocity

If θ is the constant conduction velocity of the cable we look for solutions of the form

$$V(x,t) = f(x - \theta t)$$

Therefore

$$\frac{\partial^2 V}{\partial x^2} = f'' = \frac{1}{\theta^2}\frac{\partial^2 V}{\partial t^2}$$

The cable equation hence becomes

$$\frac{1}{r_a\theta^2}\frac{\partial^2 V}{\partial t^2} = c\frac{\partial V}{\partial t} + i_i$$

Now let the axial resistance, $r_a = \dfrac{R_i}{\pi r^2}$, where r is the radius and R_i is the specific resistivity of the intra-cellular fluid. Similarly let the ionic current, $i_i = 2\pi r I_i$, where I_i is the ionic current per unit area of membrane, and let the capacitance, $c = 2\pi r C$, where C is the capacitance per unit area of membrane. The equation now becomes

$$\frac{r}{2R_i\theta^2}\frac{d^2 V}{dt^2} = C\frac{dV}{dt} + I_i \tag{1.3}$$

Since R_i, C and I_i are independent of radius r then θ^2 varies as r or θ varies as $\sqrt{r}$. This dependence is shown in Figure 1.5.

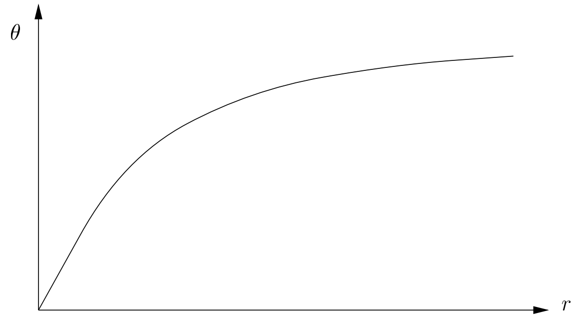

FIGURE 1.5: Dependence of conduction velocity, θ, on cable radius, r.

The implication of this dependence is that you can make signals travel faster by increasing cable radius but at a diminishing rate (see Figure 1.5). Typical conduction velocities are: AV node $\sim$ 0.2 m s^{-1} (7 μm fibres); Purkinje fibres $\sim 4 \text{ m s}^{-1}$ (50 μm fibres). Further increases in θ for large fibres require an increase in r_m. In nerves nature does this by introducing insulation called myelin on the main fast conducting nerves. This is shown in Figure 1.6. Multiple Sclerosis is characterised by the destruction of these myelin sheaths.

1.1.2 Ionic Currents

Membrane potential and current flow

Ionic currents result from the transfer of ions through the cell membrane between the intra-cellular and extra-cellular fluid as shown in Figure 1.7.

In general the cell-membrane will be permeable only to certain ions in certain directions. Hence, in general the intra-cellular concentration for an ion will be different from the extra-cellular concentration for the ion. The concentrations of common ions in the different cell spaces for different tissues are given in Tables 1.1 and 1.2. The different concentrations set up an electro-

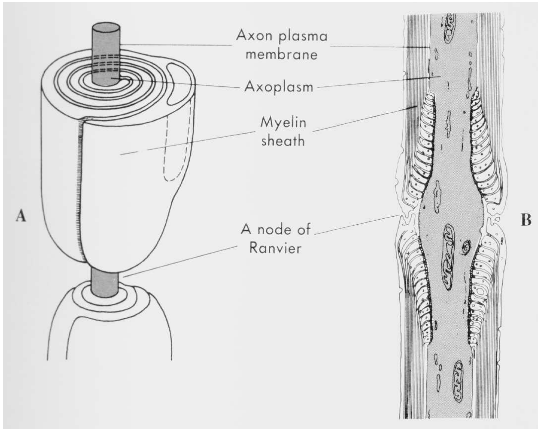

FIGURE 1.6: Myelin sheaths around nerves. (a) Schematic drawing of Schwann cells wrapping around an axon to form myelin. (b) Cross-section through a myelinated axon near a node of Ranvier. From Physiology by R.M. Berne and M.N. Levy.

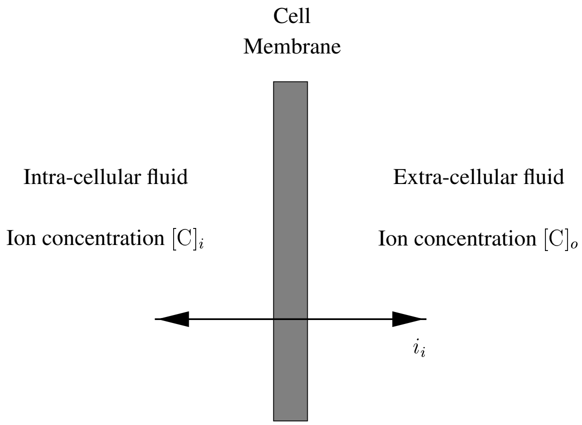

FIGURE 1.7: The cell membrane separating the intra- and extra-cellular spaces.

	Intra-cellular concentration	*Extra-Cellular concentration*	*Equilibrium potential*
Na^+	12 mM	145 mM	$E_{Na^+} = +65$ mV
K^+	155 mM	4 mM	$E_{K^+} = -95$ mV
Ca^{2+}	$< 10^{-7}$ mM	1.5 mM	$E_{Ca^{2+}} = +128$ mV
Cl^-	4.2 mM	123 mM	$E_{Cl^-} = -88$ mV

TABLE 1.1: Intra- and Extra- cellular ion concentrations and equilibrium potentials for mammalian skeletal muscle.

	Intra-cellular concentration	*Extra-Cellular concentration*	*Equilibrium potential*
Na^+	5–34 mM	140 mM	$E_{Na^+} = +51$ mV
K^+	104–180 mM	5.4 mM	$E_{K^+} = -85$ mV
Ca^{2+}	0.0003–0.001 mM	3 mM	$E_{Ca^{2+}} = +133$ mV
Cl^-	8–79 mM	100 mM	$E_{Cl^-} = -22$ mV

TABLE 1.2: Intra- and Extra- cellular ion concentrations and equilibrium potentials for mammalian cardiac muscle.

chemical potential across the cell membrane. This potential is given by the Nernst equation

$$\begin{aligned} E &= \frac{RT}{ZF} \ln \frac{[\mathrm{C}]_o}{[\mathrm{C}]_i} \\ &= 2.303 \frac{RT}{ZF} \log \frac{[\mathrm{C}]_o}{[\mathrm{C}]_i} \end{aligned} \tag{1.4}$$

where R is the gas constant, T the absolute temperature, Z the valency of the ion involved and F is Faraday's constant. Note that at 37 °C $\frac{RT}{F}$ is approximately 26 mV. Hence $2.303\frac{RT}{F}$=60 mV (i.e. 60 mV change for a 10 fold change in concentration). Equilibrium potentials for various ions are shown in Tables 1.1 and 1.2.

Now from Ohm's law the ionic current through a membrane for say, potassium, will be given by

$$\begin{aligned} i_K &= \frac{1}{R} \Delta V \\ &= g_K (V_m - E_K) \end{aligned}$$

where g_K is the membrane *conductance* for potassium ions and V_m is the *membrane potential* (difference in potential between the intra-cellular and extra-cellular spaces). This equation is represented graphically in Figure 1.8.

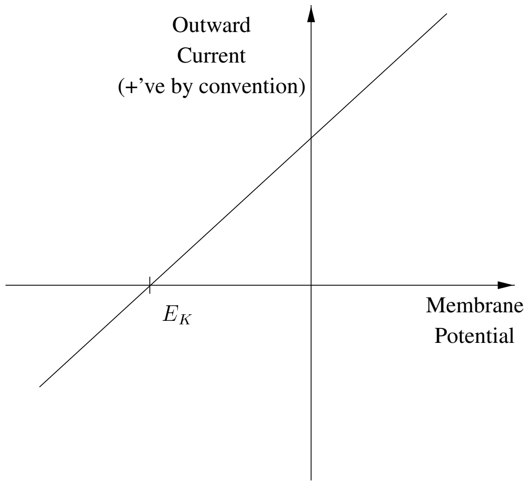

FIGURE 1.8: Potassium ionic current vs. membrane potential.

We should note here that by definition an outward current (from intra- to extra-cellular space) is defined as a positive current. It should also be noted that electrical current flows in the direction that the positive charge carriers move. Hence the potassium current (in which the positive K^+ ions move from inside the cell to outside the cell) is a positive current. Consider now Figure 1.8. As the membrane potential increases above E_K the membrane current changes from a negative current to a positive current, or in order words, the membrane current changes from an inward current to an outward current. The point E_K is hence known as the *reversal potential* as it is at this point that the current reverses its direction.

Membrane conductance for an ion depends on the number of conducting channels (see Figure 1.3) and their properties or *gating*.

Gating mechanism

When a conducting channel is fully open (i.e. all the gates are fully open) the membrane current is given by

$$\overline{i_K} = \overline{g_K}\,(V_m - E_K) \tag{1.5}$$

where $\overline{g_K}$ is constant (i.e. can be used in Ohm's law). Now consider an intermediate state. If the fraction of gates open (or in their α state) is y then the fraction of gates closed (or in their β state) is $1 - y$. The membrane conductance is hence given by

$$g_K = \overline{g_K} y \tag{1.6}$$

and the membrane current by

$$i_K = \overline{i_K} y \tag{1.7}$$

Now if the opening rate coefficient is α_y, and the closing rate coefficient is β_y then the gating mechanism can be depicted as in Figure 1.9.

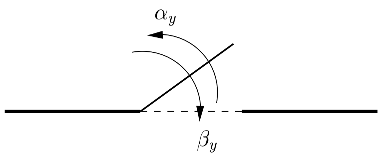

FIGURE 1.9: Gating mechanism.

The change in the fraction of gates open is hence governed by

$$\frac{dy}{dt} = \alpha_y\,(1 - y) - \beta_y y \tag{1.8}$$

The processes of opening and closing of the gates is called *gate kinetics*. The steady state for the gates for this form of gating kinetics is given by

$$\frac{dy}{dt} = \alpha_y\,(1 - y_\infty) - \beta_y y_\infty \quad \Rightarrow \quad y_\infty = \frac{\alpha_y}{\alpha_y + \beta_y} \tag{1.9}$$

From experiment it has been found that both α_y and β_y depend on the membrane voltage e.g. on depolarisation (increasing membrane voltage) α_y might increase and β_y might decrease (as is the case for K^+ ions). This is shown graphically in Figure 1.10.

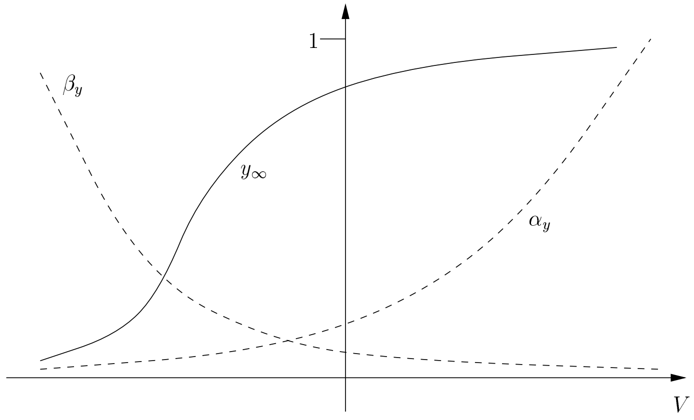

FIGURE 1.10: Dependence of the gating rate constants on membrane voltage for a typical K^+ type channel.

The behaviour of the gates (and hence channel conductance) for a membrane voltage step is shown in Figure 1.11.

1.1.3 The Squid Axon and Hodgkin-Huxley Equations

The squid action potential

In 1952 A.L. Hodgkin and A.F. Huxley performed voltage clamp experiments (like the one shown in Figure 1.11) on giant squid axons (Hodgkin & Huxley 1952). They found that the onset of the K^+ current was sigmoidal in shape not exponential as in Figure 1.11. To explain this the membrane current had to depend on the gates in a non-linear way, i.e.

$$i_y = \overline{i_y} y^\gamma \tag{1.10}$$

where γ is the number of gates (in series) per channel.

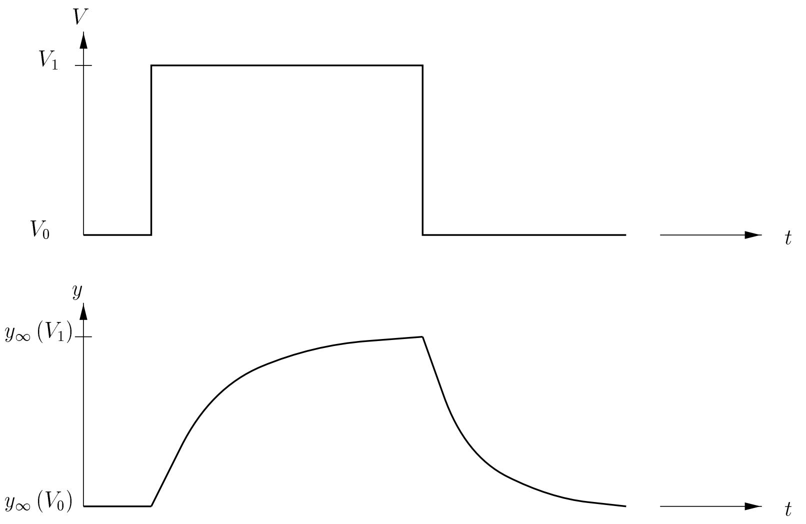

FIGURE 1.11: Behaviour of open gates (and hence channel conductance) for a membrane voltage clamp step experiment.

For example consider two gates ($\gamma = 2$) with $y = \frac{1}{2}$ (i.e. half the gates open). In this case we can average all the gates into one of the four possible states that the two gates can be in, namely (open, open), (open, closed), (closed, open) and (closed, closed). For conduction through the channel both gates have to be in the open state, that is the fraction of conducting gates is $\frac{1}{4} = \left(\frac{1}{2}\right)^2 = y^\gamma$.

Hodgkin and Huxley found that you need $\gamma = 4$ gates for K^+. These gates were called the n gates (or potassium activation variables) and were found to open with increasing membrane potential. Hence the equation for the potassium current is

$$i_K = n^4 \overline{g_K} \left(V_m - E_K\right) \tag{1.11}$$

For the sodium channels the gating mechanisms and kinetics were found to be a bit more complicated. It was found that you needed gates which open with increasing membrane potential *and* gates which close with increasing membrane potential. The gates which open with in-

creasing potential were called the m gates (or sodium activation variables) and the gates which close with increasing potential were called the h gates (or sodium inactivation variables). The equation for the sodium current is

$$i_{Na} = m^3 h \overline{g_{Na}} \left(V_m - E_{Na}\right) \tag{1.12}$$

and the sodium gate voltage relationship for a voltage step is shown in Figure 1.12.

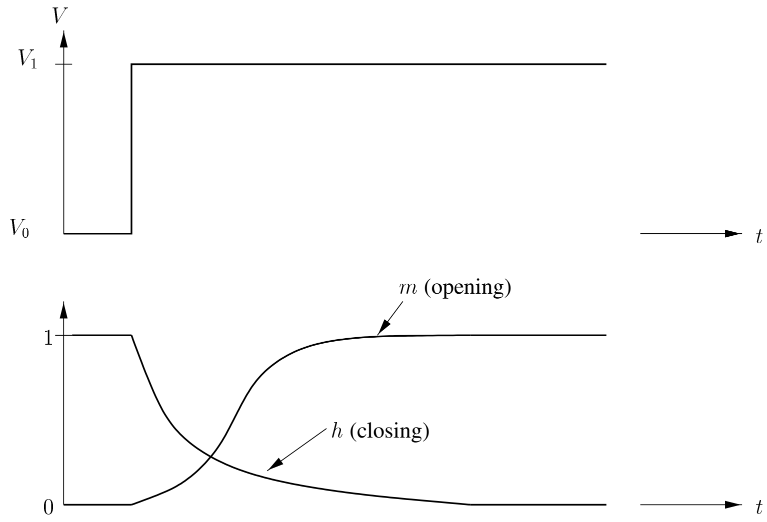

FIGURE 1.12: Behaviour of the sodium gates (and hence channel conductance) for a voltage clamp step experiment.

It should be noted that the mechanisms for the shutting off of the sodium and potassium channels are different. For the potassium channels the process is called *deactivation*. This is characterised by the gates closing only when the membrane potential drops. For the sodium channels the process is called *inactivation*. This is characterised by an inactivation gate that closes when the potential rises. Thus the channel closes even when the membrane potential does not drop. These two processes are shown in Figure 1.13.

Putting the Na^+ and K^+ channels together we obtain the nerve *action potential* shown in Figure 1.14.

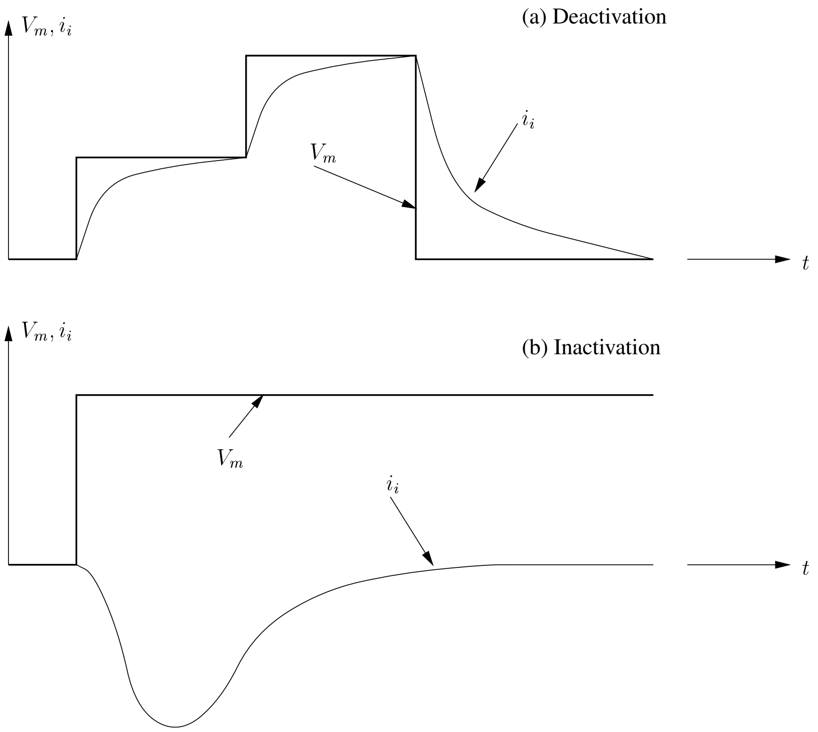

FIGURE 1.13: (a) Deactivation and (b) inactivation of a channel with membrane potential changes.

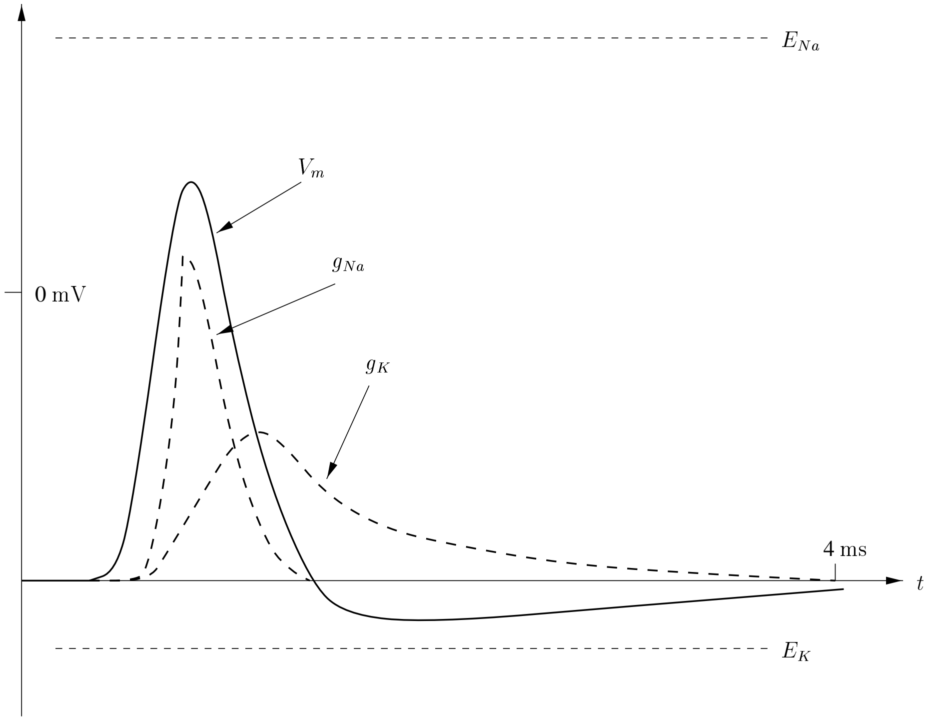

FIGURE 1.14: The squid action potential with the sodium and potassium channel conductances.

Propagating action potentials

When this process happens at one end of a nerve we get a *propagating* action potential. By raising the membrane potential of one end of the nerve (or by injecting current) we generate an axial current along the nerve from the high potential end to the low potential end in accordance with Ohm's law. This current raises the membrane potential (depolarises) to a point whereby the sodium channels open. The point is known as the *threshold voltage*. Once the sodium channels open the sodium ions flood in and cause an inward current which raises the membrane potential even higher. This causes further axial current and a resultant action potential is hence propagated down the nerve. This process is shown in Figure 1.15. It should be noted that this process requires ion pumps in the membrane to restore the intra- and extra-cellular ion concentrations to their resting levels. These pumps require energy (ATP - adenosine tri-phosphate) to operate. Until the ionic concentrations in an area of nerve have been returned to their resting states an action potential will not propagate in this area of nerve. This period after an action potential has passed when the nerve cannot be activated is called the *refractory period*.

The Hodgkin-Huxley equations

The work of Hodgkin and Huxley[1] can be summarised in the Hodgkin-Huxley equations for the action potential.

$$\begin{aligned}
\frac{1}{r_a}\frac{\partial^2 V_m}{\partial x^2} &= C\frac{\partial V_m}{\partial t} + i_K + i_{Na} \\
i_K &= n^4 \overline{g_K}\left(V_m - E_K\right) \\
i_{Na} &= m^3 h \overline{g_{Na}}\left(V_m - E_{Na}\right) \\
\frac{dn}{dt} &= \alpha_n\left(1-n\right) + \beta_n n \\
\frac{dm}{dt} &= \alpha_m\left(1-m\right) + \beta_m m \\
\frac{dh}{dt} &= \alpha_h\left(1-h\right) + \beta_h h
\end{aligned} \tag{1.13}$$

where $\alpha_n, \beta_n, \alpha_m, \beta_m, \alpha_h$ and β_h are all voltage dependent.

[1] Alan Hodgkin, Andrew Huxley and Sir John Eccles were awarded the 1963 Noble prize for Physiology or Medicine for the study of the transmission of nerve impulses along a nerve fibre.

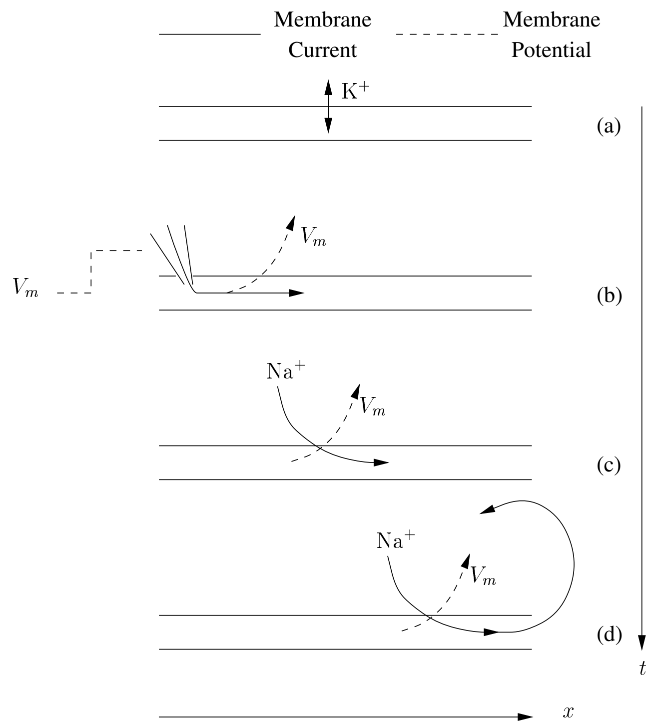

FIGURE 1.15: Propagating action potential. (a) The nerve is initially at rest at -'ve membrane potential with the cell membrane permeable to K^+. (b) The membrane potential is raised (or current is injected into the cell) at the left hand end which depolarises (raises the membrane potential of) the cell. (c) The raised membrane potential opens the Na^+ m gates at the threshold potential and further raises the membrane potential to further increase the axial current. (d) the action potential is propagated via local current loops.

1.2 Muscle

There are three main kinds of muscle found in the body, namely skeletal muscle, cardiac (heart) muscle and smooth muscle (used, for example, in the constriction of the arteries).

1.2.1 Anatomy

Gross anatomy

The gross structure of skeletal muscle is best though of in terms of a hierarchy. From the organ down to the cellular level there are three levels in this hierarchy. These levels are defined by connective tissue (made up of mainly collagen) that encases each muscle level. The first level is that of the whole *muscle organ* which is encased by the *epimysium*. The next level down is called the *fascicle* of the muscle and is encased by the *perimysium*. The final level is that of the *muscle fibre* or muscle cell. This level is encased by the *endomysium*. This hierarchy is shown in Figure 1.16.

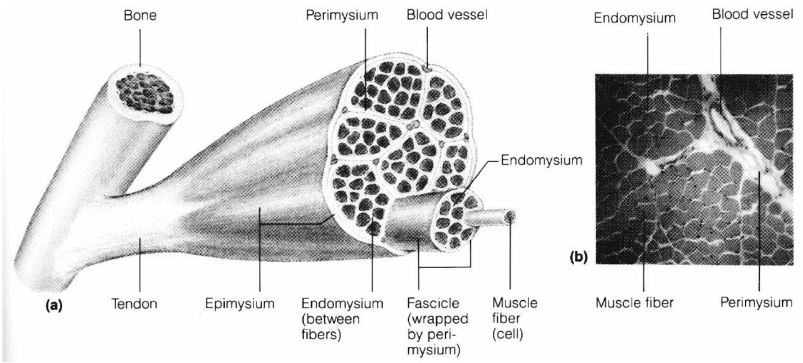

FIGURE 1.16: Gross anatomy of skeletal muscle. (a) The hierarchy of internal muscle structures and connective tissue that encloses them. (b) Photomicrograph of a cross section of skeletal muscle (64 x). From Human Anatomy and Physiology by E. N. Marieb.

Cellular anatomy

The muscle cell differs a little from the idealised cells of the axons or nerves. Firstly the terminology applied to muscle cells is a little different. In muscle cells the cell membrane is known as the sarcolemma. This word comes from the Greek base word *sarc-* which means flesh. A second difference is that muscle cells are *multinuclear*, which means they have more than one nucleus per cell.

The anatomy of the muscle is organised in another hierarchy. Each muscle fibre is made up of a number of smaller units called *myofibrils*. These myofibrils are in turn made up two different proteins called *myofilaments*. The two proteins are distinguished by their size and called the thick and thin filaments. The thick filament is made up of a protein called *myosin*. The thin filament is made up predominately of a protein called *actin*. This hierarchy is shown in Figure 1.17.

Within each myofibril a further part of muscle can be identified. The proteins actin and myosin are arranged in a regular fashion both longitudinally and radially throughout the myofibril. In the longitudinal direction these filaments are arranged so that they overlap in a regular fashion. When viewed under the microscope this regular overlap generates a series of light and dark bands. This pattern of light and dark bands gives muscle a striped appearance. Both skeletal and cardiac (but not smooth) muscle exhibit this striped pattern and are hence known as *striated* (meaning striped) muscle. These striations are shown in Figure 1.17a.

Looking more closely at each band a line can be seen in the middle of each band. The line is named the Z-line in the light (or I-band) and the M-line in the dark (or A-band). As these structure are regular and repeating a further part of muscle can be identified. This unit is known as the *sarcomere* and is defined as the unit of muscle between two consecutive Z-lines. The typical sarcomere length in resting skeletal muscle is $2.2\ \mu\mathrm{m}$. These bands, lines and the sarcomere are shown in Figure 1.17c–e.

The complete anatomical hierarchy of muscle is shown in Figure 1.18.

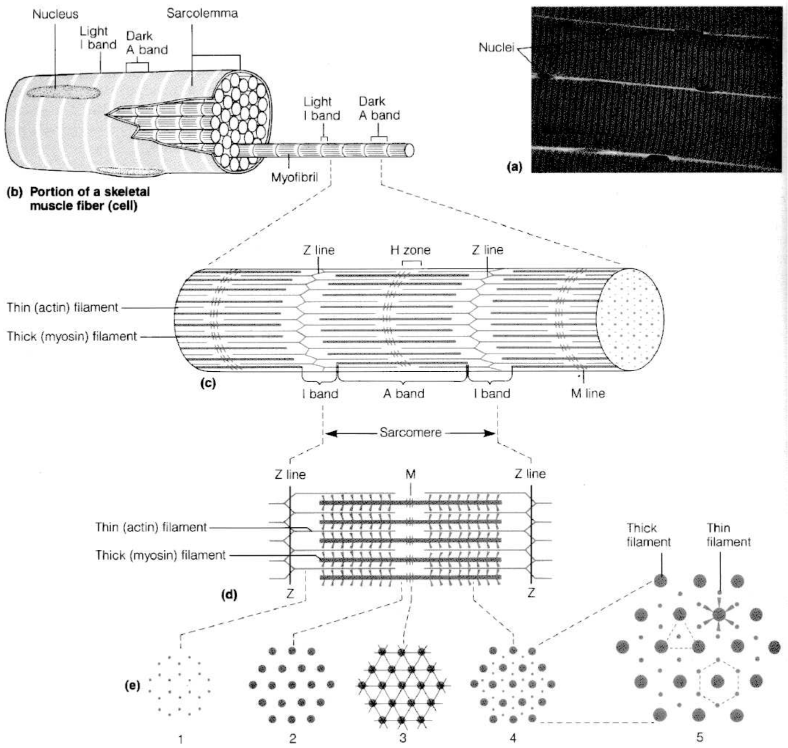

FIGURE 1.17: Anatomy of a muscle cell (fibre). (a) Photomicrograph (x 250) (b) Diagram of muscle fibre (c) Portion of a myofibril (d) Enlargement of a sarcomere (e) Arrangement of the thick and thin filaments. From Human Anatomy and Physiology by E. N. Marieb.

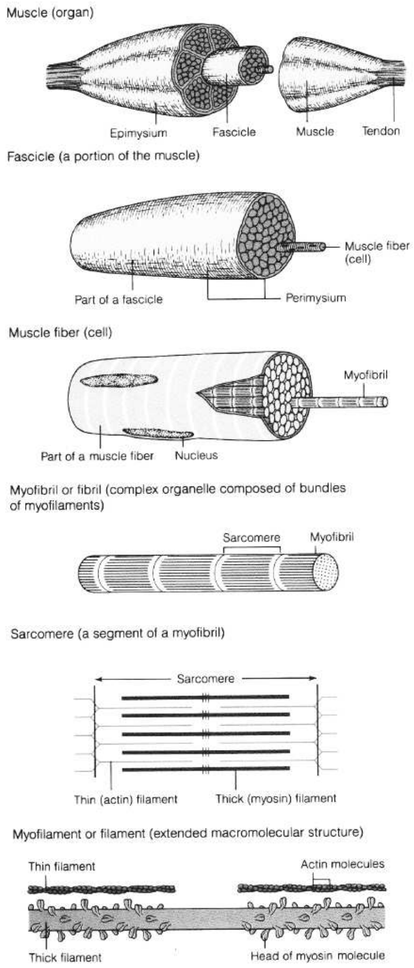

FIGURE 1.18: Organisation of skeletal muscle. From Human Anatomy and Physiology by E. N. Marieb.

The myofilaments

We will now look in more detail at the individual myofilaments as the structures at this level are important when we look at how muscle contracts in Section 1.2.4. The thick filament is made of a number of myosin molecules. Each myosin molecule consists of a long “tail” and a large “head” as shown in Figure 1.19a. These heads are also known as *cross-bridges*, the meaning of which will become clear later.

Each myosin molecule is about $12\ \mathrm{nm}$ in diameter and about $1.6\ \mu\mathrm{m}$ long. Groups of myosin molecules arrange themselves so that in the longitudinal direction of the thick filament the molecules are tail to tail and in the radial direction the heads are in a helical pattern with a pitch of $42.9\ \mathrm{nm}$. This is shown in Figure 1.19b.

The thin filament is more complicated than the thick filament in that it contains three main components. The main component is actin. Actin is a protein that forms a double stranded helix. The overall molecule is about $5\ \mathrm{nm}$ in diameter and extends $1\ \mu\mathrm{m}$ either side of the Z-line. Within the groove defined by the double stranded actin helix runs the second component of the thin filament, a molecule called *tropomyosin*. The final component of the thin filament is a complex called the *troponin* complex. This complex is attached along the tropomyosin molecule at regular intervals. The arrangement of the thin filament is shown in Figure 1.19c and the overall arrangement of the myofibril in Figure 1.19d.

1.2.2 Properties of muscle contraction

Twitch and tetanus

When a muscle is stimulated (electrically) it contracts and generates force. If the muscle is fixed in such a way as then ends cannot move the muscle is said to be contracting *isometrically*, that is contracting at constant length. Another mode of contraction is if the muscle contracts against a constant load. Here the muscle is said to be contracting *isotonically*, that is contracting at constant tension.

For isometric contraction the way force is developed depends on the mode of stimulation. A

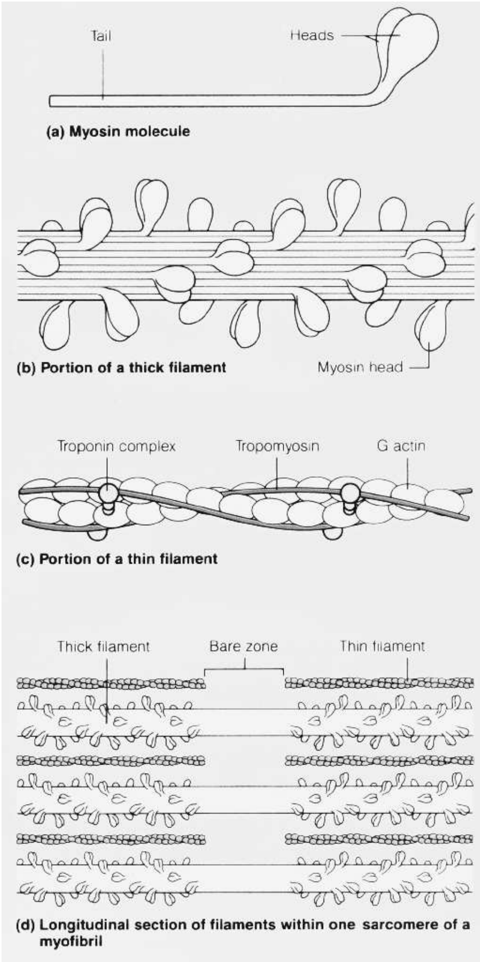

FIGURE 1.19: Structure of the myofilaments. From Human Anatomy and Physiology by E. N. Marieb.

single stimulus produces a *twitch*, in which tension increases rapidly and then declines. If a second stimulus is applied before the first twitch has fallen to zero, the peak tension for the second twitch is higher than that of the first. As the frequency of stimulation is increased the tension generated rises smoothly and the muscle is said to be in *tetanus*. This is shown in Figure 1.20.

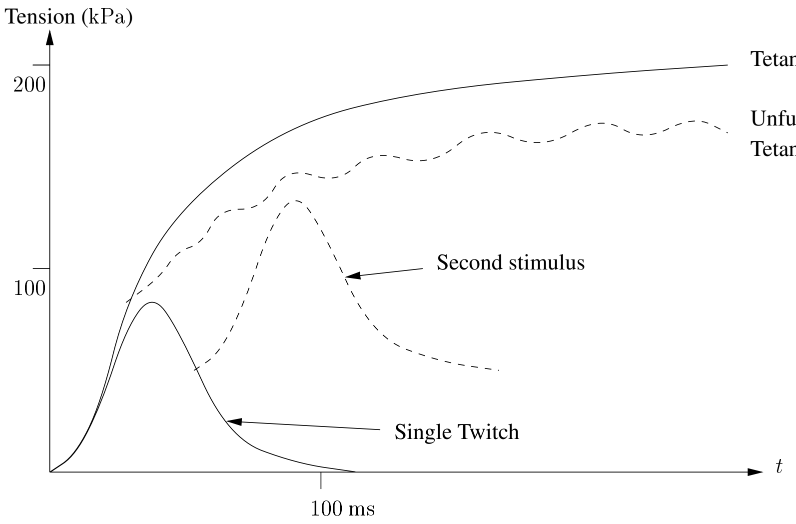

FIGURE 1.20: Isometric force generation in response to stimulus.

The critical frequency for tetanus is about 10 stimulations per second. The maximum force developed in tetanus is about 2–3 times greater than that of a twitch.

Isometric force-length relationship

For isometric contraction an experiment can be performed whereby the amount of force a muscle generates is measured for a number of different lengths of muscle. The results for this experiment are shown in the top solid line of Figure 1.21.

In addition to this passive muscle (that is muscle that is not contracting) resists extension beyond the normal resting length for the muscle. It is hence possible in this experiment to also

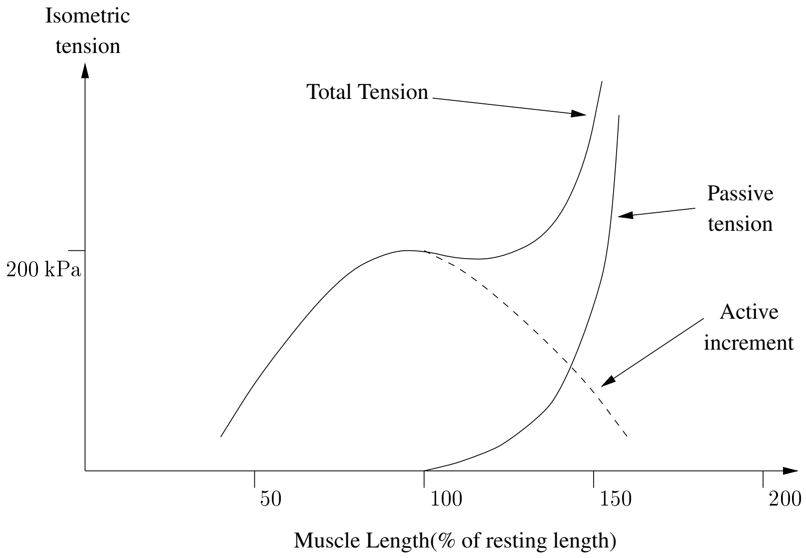

FIGURE 1.21: Isometric force generation as a result of muscle length.

measure the passive force-length behaviour of muscle. This is shown in the bottom solid line in Figure 1.21. By subtracting the passive tension from the total tension we can estimate the amount of tension developed in the muscle through contraction. This is the dashed line in Figure 1.21. As can be seen this active tension is maximum for lengths close to the resting length and declines if the muscle length is either increased or decreased.

Isometric quick release

When a muscle in isometric tetanus is suddenly shortened and clamped at a new fixed length, the tension falls abruptly and sub-sequentially rises to a new maximum level determined by the isometric force-length relationship.

The extent of the shortening (or length step) determines the extent of the initial fall in tension and, in part, the time course of the subsequent recovery.

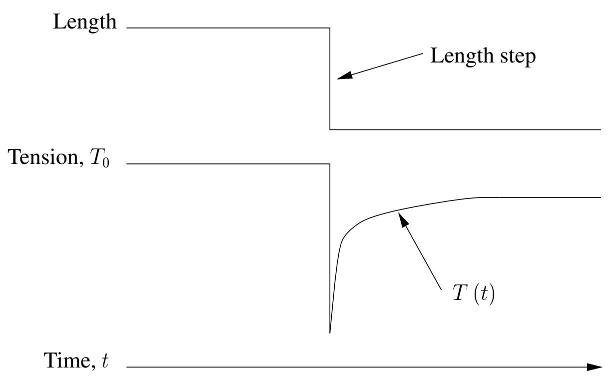

FIGURE 1.22: Isometric quick release experiment.

Isotonic force-velocity relationships

In an isotonic contraction the muscle is allowed to shorten against a constant force or load. This experiment is normally performed with the muscle attached to one end of a lever with a fixed amount of weight on the other end of the lever. The muscle is then allowed to contract at constant length (i.e. initially isometric contraction) and generate force. When the force generated is equal to the applied weight (known as the afterload) the muscle begins to shorten. It has been found that the velocity of this shortening is constant for a given afterload and that the magnitude of this velocity depends on the magnitude of the afterload. This is shown in Figure 1.23.

An experiment can be done whereby the velocity of shortening is measured for a varying amount of afterload. The results of this experiment are known as the isotonic force-velocity relationship and are shown in Figure 1.24. This curve has a characteristic hyperbolic shape. The maximum force generated occurs when the muscle is contracting isometrically (hence at zero velocity) and is denoted T_0. The maximum velocity occurs when there is no after-load and is denoted V_{max} (experimentally this is found from extrapolating the curve from low values of afterload).

Figure 1.24 represents what we would expect from experience with our own muscles. Our muscles are designed to lift small loads quickly or large loads slowly.

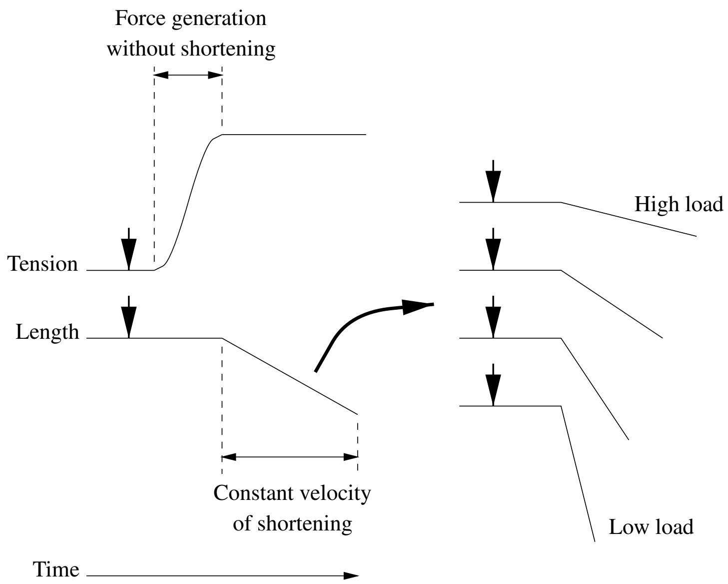

FIGURE 1.23: Isotonic force-length relationship.

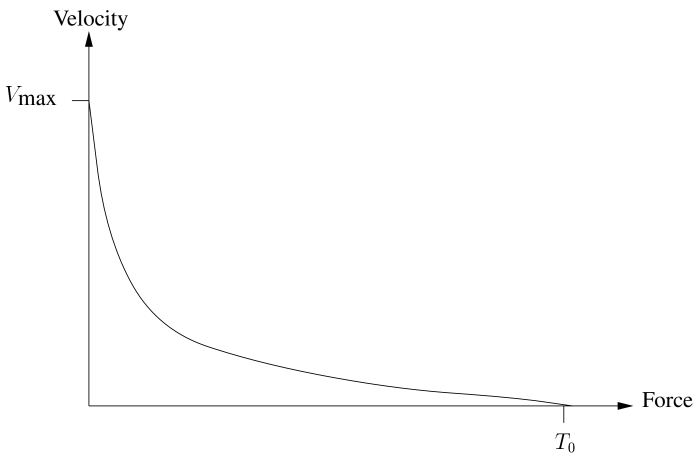

FIGURE 1.24: Isotonic force-velocity relationship.

Isotonic quick release

With this technique the muscle is first caused to contract isometrically and is then abruptly released to shorten against constant afterload. Typical results are shown in Figure 1.25.

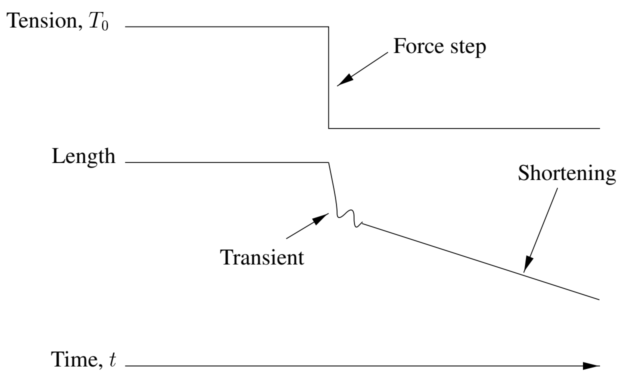

FIGURE 1.25: Isotonic quick release experiment.

One release, the tension falls rapidly to the level of the new afterload. Initially there is an abrupt shortening which coincides with the change in tension. Subsequentally, a slower isotonic shortening occurs at a velocity which is inversely related to the new afterload.

1.2.3 Hill model of muscle contraction

Hill's three component model

Hill (1938) proposed a simple mechanical model that was empirically based. Hill's three component model lumps the mechanical behaviour of muscle into three elements:

1. **The parallel elastic element**: This represents the potential energy stored in relaxed skeletal muscle when it is stretched beyond its resting length. It is assumed that this element represents the passive elastic structures such as connective tissue.

2. **The series elastic element**: This is represented as an undamped spring. It was assumed that the length of this element is dependent only on the force in the muscle and is therefore independent of the kinetics of contraction.

3. **The contractile element**: In this element all the active features of contraction are lumped in a "black-box" approach. It is assumed that this component was freely extensible in the relaxed state and that is was "switched on" at the onset of contraction. Once fully activated the force generated by this contractile element was assumed to be dependent only on its instantaneous length and velocity and independent of time.

This model is shown in Figure 1.26.

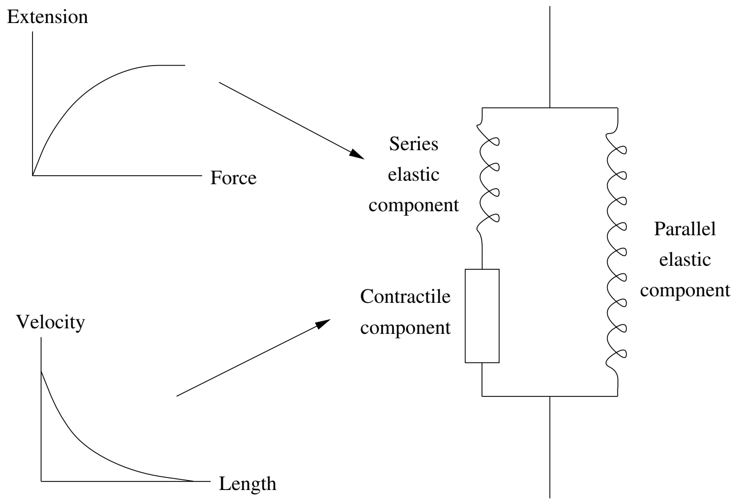

FIGURE 1.26: Hill model of muscle

A.V. Hill proposed the following relationship for the force-velocity relationship for contraction.

$$(V + b)\,(T + a) = b\,(T_0 + a) \tag{1.14}$$

where V is the velocity of shortening, T the tension, T_0 the isometric tension (at zero velocity) and a and b are parameters. This equation can be rewritten as

$$V = \frac{b\,(T_0 - T)}{T + a} \tag{1.15}$$

From experiment it has been found that $\frac{a}{T_0} = 0.28$ and $b = 0.4$ muscle lengths/second ~ 12 $\mathrm{mm\ s^{-1}}$. Hence the maximum velocity of shortening can be found at the point where $T = 0$, i.e.

$$V_0 = V_{\max} = \frac{bT_0}{a} = \frac{0.4}{0.28} \sim 1.43 l_0/s \tag{1.16}$$

where l_0 is the resting length of the muscle.

Limitations of Hill's model

Hill's model for muscle formed the basis of the understanding of muscle for about twenty years. It was eventually discarded because the predictions of the model and experiment differed for two key experiments:

1. The Hill model failed to predict accurately the time course of the rise in force during isometric contraction.
2. The Hill model does not predict the transients following quick isometric and isotonic release.

1.2.4 Sliding filament theory

Sarcomere force-length relation

In 1954 H.E. Huxley observed that during contraction the size of the I-band diminishes. They proposed that this could be explained by allowing the relative sliding of the thick and thin filaments. The myofilaments, themselves were found not to shorten. This process explains the sarcomere force-length relation shown in the top part of Figure 1.27. This theory was known as the *sliding filament theory*.

The shape of the curve in Figure 1.27 can be explained by the different degree of interaction between the thick and thin filaments (also shown schematically in the bottom part of Figure 1.27).

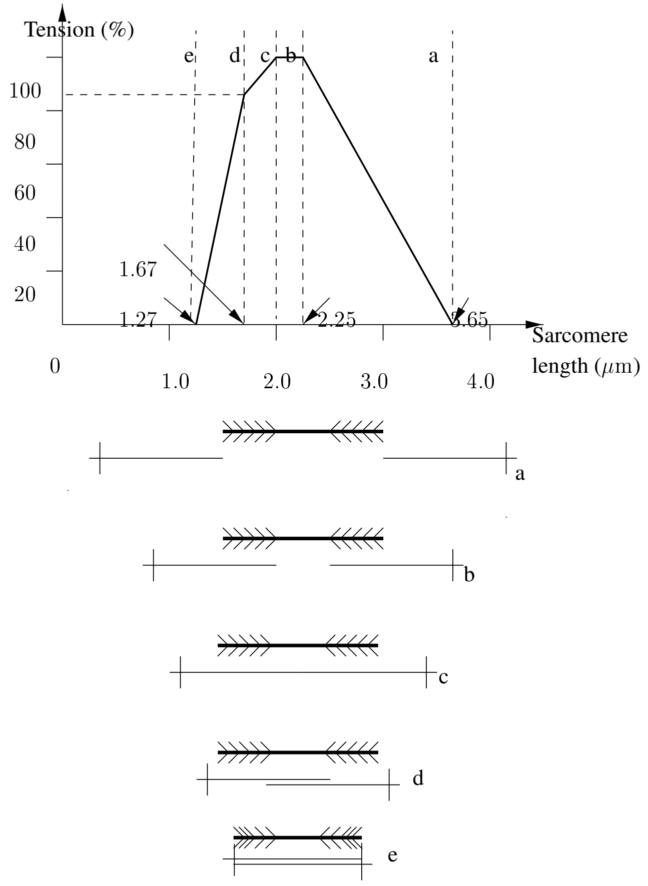

FIGURE 1.27: Sarcomere force-length relationship.

At point (a) no force is generated in the sarcomere as there is no interaction between the thick and thin filaments. At point (b) there is maximum force as there is maximum interaction. This continues up to point (c) when the thin filaments start to interact. At point (d) there is steric interference of the thin filaments limiting the interaction between them and the thick filaments. At point (e) there is interference of both the thick and thin filaments resulting in no force production.

Excitation-Contraction of muscle

We will now look in a bit more detail as to how muscle contracts in response to a stimulus. First consider the schematic of the muscle cell as shown in Figure 1.28.

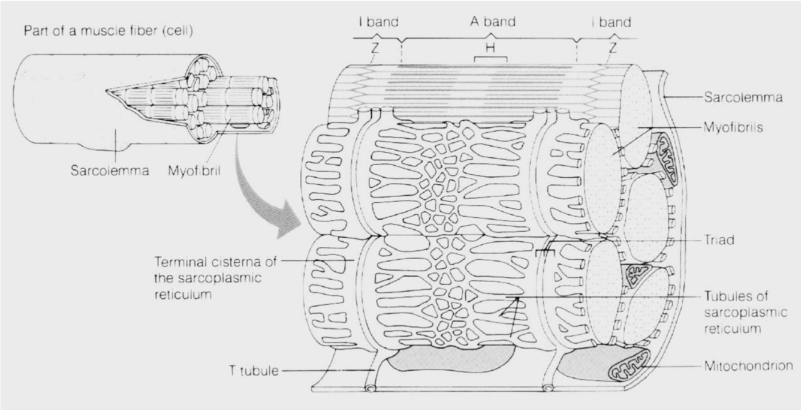

FIGURE 1.28: The muscle cell showing cell membrane details. From Human Anatomy and Physiology by E. N. Marieb.

What should be noted here is the network of "tubes" called the *sarcoplasmic reticulum* just under the sarcolemma (cell membrane). This sarcoplasmic reticulum is "connected" to the sarcolemma through the T-tubules (or transverse tubules) at the *terminal cisterna*. This is shown schematically in Figure 1.29.

The method of contraction for a muscle twitch is then as follows: An action potential propagates along the sarcolemma from a neuro-muscular junction and down the T-tubule to the terminal cisterna of the sarcoplasmic reticulum. The change in the membrane potential from

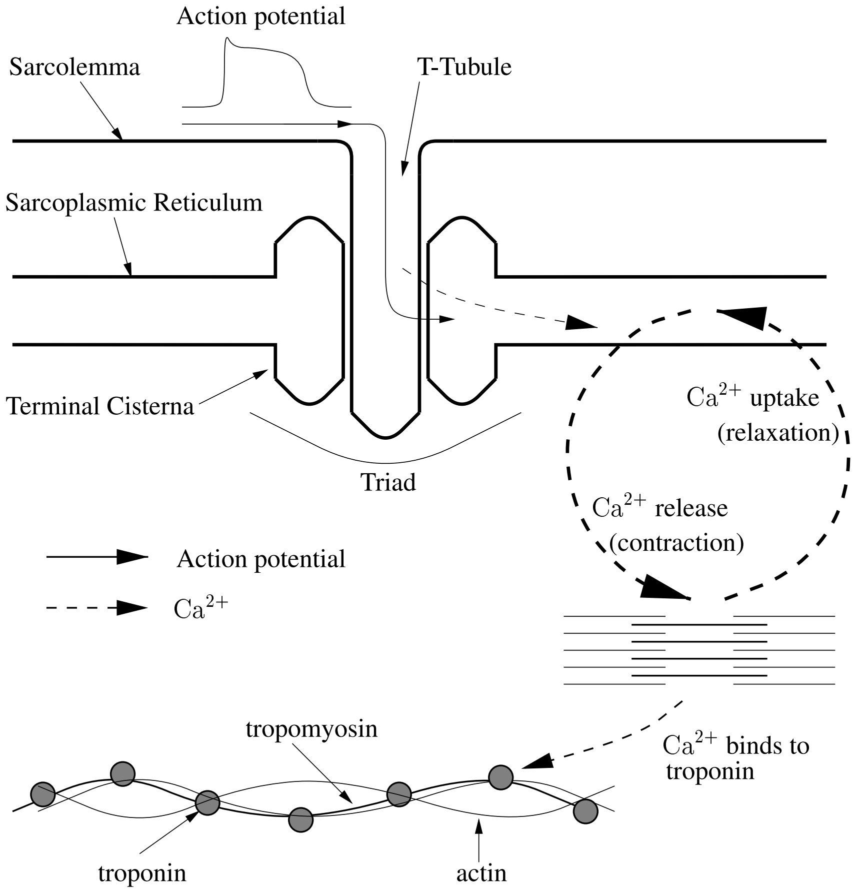

FIGURE 1.29: Excitation contraction coupling in skeletal muscle.

the action potential opens voltage dependent gates and allows a small amount of Ca^{2+} ions to enter the sarcoplasmic reticulum. This triggers a much greater release of Ca^{2+} into the sarcoplasm (the inside of the cell). Calcium then interacts with troponin in the thin filament which then undergoes steric rearrangement. This rearrangement allows a myosin head (cross-bridge) to bind to actin in a reaction that causes the muscle to contract. At the same time the muscle is contracting the intra-cellular calcium also activates pumps in the sarcoplasmic reticulum. These pumps take the calcium out from the cell and back into the sarcoplasmic reticulum. As the level of intra-cellular calcium drops the cross-bridges can not re-attach once they (eventually) detach and the muscle relaxes.

1.2.5 Muscle energetics

Cross-bridge cycling

When muscle contracts it does work. This work hence requires a supply of energy. The main "currency" of energy in the cell is adenosine tri-phosphate or ATP. The equilibrium equation by which ATP generates energy is

$$\mathrm{ATP} \rightleftharpoons \mathrm{ADP} + \mathrm{P} + \mathrm{energy} \tag{1.17}$$

where P is free phosphate and ADP is adenosine di-phosphate.

As explained in Section 1.2.4 a muscle twitch occurs when a myosin cross-bridge attaches to actin and stops when the cross-bridge detaches. For a tetanised muscle, however, the story is a slightly different. During tetanus the cross-bridges are continually attaching, detaching and then re-attaching. This process is known as *cross-bridge cycling* and is shown in Figure 1.30.

The cross-bridge cycle starts at point (1) in Figure 1.30 when the myosin cross-bridge (with ADP and P) attaches to actin. At this point the myosin-head is in it's *high-energy* configuration. The myosin head then rotates to its *intermediate-energy* configuration causing the actin molecule to slide resulting in contraction. As the myosin head rotates the myosin tail is stretched generating force. ADP and P are released from the myosin head during this process. This is point (2) in Figure 1.30. ATP now attaches to the myosin head causing the cross-bridge to deattach from the actin molecule. The myosin molecule is now it's *low-energy* configuration

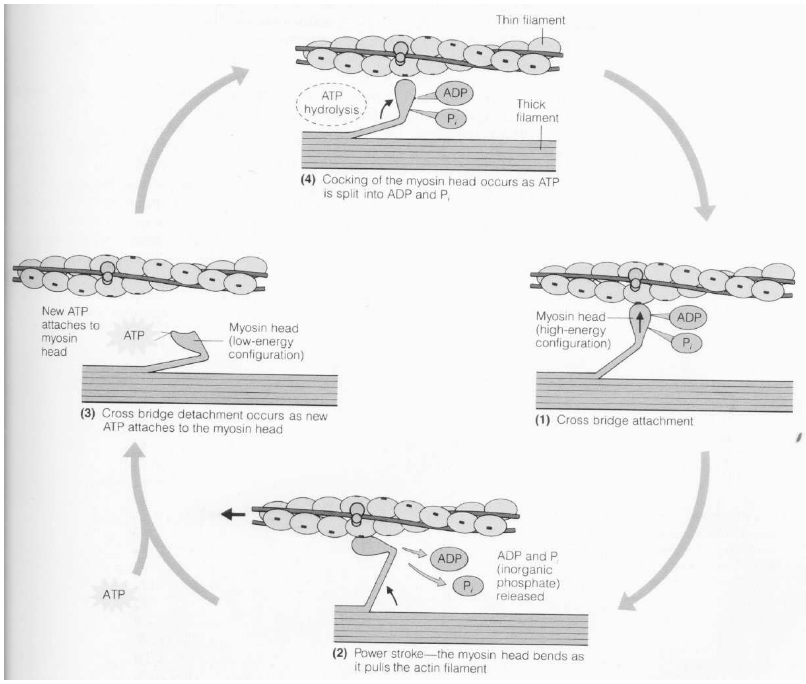

FIGURE 1.30: Cross-bridge energy cycle. From Human Anatomy and Physiology by E. N. Marieb.

as shown in point (3). Hydrolysis of the ATP bound to the myosin head now occurs and the cross-bridge cycle moves to point (4). The cycle is completed when the cross-bridge re-attaches to the actin molecule. Recalling Figure 1.24 we can now interpret V_0 as the maximum turnover rate of cross-bridges.

It should be noted that energy (ATP) is required for *relaxation* not contraction of muscle. This is the reason why *rigor mortis* occurs on death. With death the body ceases the manufacture of ATP. As the stores of ATP run down muscles that are contracted cannot be relaxed and hence the muscle stays in its contracted state.

Muscle Power

We will return now to Hill's model of contraction to consider muscle power. Recall Equation (1.15) for velocity, i.e.

$$V = \frac{b\left(T_0 - T\right)}{T + a}$$

Now power=force x velocity, hence

$$P = Tb\frac{T_0 - T}{T + a} \tag{1.18}$$

Maximum power will occur when $\dfrac{dP}{dT} = 0$, therefore

$$\begin{aligned} 0 &= b\frac{T_0 - T}{T + a} + Tb\frac{\left(T + a\right).1 - \left(T_0 - T\right)}{\left(T + a\right)^2} \\ &= \frac{b\left(T + a\right)T_0 - T - T\left(T_0 + a\right)}{\left(T + a\right)^2} \end{aligned}$$

$$\Rightarrow -T^2 - 2aT + aT_0 = 0 \quad \text{or} \quad T^2 + 2aT - aT_0 = 0$$

hence

$$\begin{aligned} T &= \frac{-2a \pm \sqrt{4a^2 - 4aT_0}}{2} \\ &= \sqrt{a^2 - aT_0} - a \\ &= 0.32T_0 \quad \text{with} \quad \frac{a}{T_0} = 0.28 \end{aligned}$$

that is maximum power occurs when $T \approx \dfrac{1}{3}T_0$ and similarly maximum velocity occurs when $V \approx \dfrac{1}{3}V_0$.

Heat production

Consider now the heat produced during isometric tension, as shown in Figure 1.31.

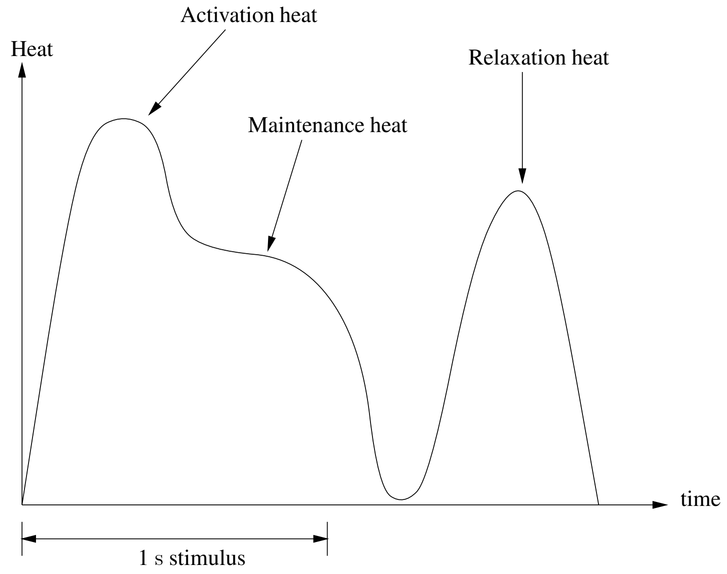

FIGURE 1.31: Heat production during isometric tension.

Heat production in muscle can be broken into the following components.

1. **Heat production due to isometric contraction**: The heat production during isometric tetanus can be further broken into fast and slow, or *labile* and *stable* components. Stable heat rate is maximum at the normal resting length of the muscle and falls either side of this length (i.e. the same trend and the force-length relationship). Stable heat production is due to ATP splitting by two-processes: actin-myosin interaction (which is proportional to filament overlap) and calcium pumping by the sarcoplasmic reticulum. Labile heat, on the other hand, is independent of length and hence it is not associated with actin-myosin interaction. It is thought labile heat production is due to processes associated with the initiation of contraction.

2. **Heat production due to activation**: When muscle is stretched to a length such that there is no actin-myosin interaction stable heat production is not zero (in fact it is about 30% of the stable heat production at resting length). This non-zero stable heat production can not be due to actin-myosin interaction (as there is no filament interaction) and is thought to be due to activation and excitation-contraction coupling.

3. **Heat production due to shortening**: A.V. Hill[2] showed that if a muscle is allowed to shorten more heat is produced than if the muscle was held at a fixed length. Hill showed that this *shortening heat* is dependent only on the extent of shortening and is independent of the time during which shortening occurs, and the load under which the shortening took place. This extra shortening heat is due to the increased velocity of the muscle which increases the turnover of cross-bridges and hence increases the amount of ATP split and energy/heat produced.

4. **Relaxation heat**: As shown in Figure 1.31 as force declines at the termination of a tetanus heat production falls then rises again to a shortlived peak. This secondary rise in heat production is termed *relaxation heat* and is thought to be due to: (1) dissipation in the muscle of work performed on it by external series elasticity; (2) dissipation of work on one region of the muscle as it extended by shortening in another region; (3) thermoelastic effects.

5. **Recovery heat**: Hill described this heat around 1922. He showed that the initial heat from contraction was followed by a *recovery heat* of similar magnitude over the next 20–30 minutes. It is generally accepted that this recovery heat is associated with the resynthesis of phosphocretaine and restoration of glycogen stores. For muscles which are specialised for sustainted activity (e.g. heart muscle) initial and recovery heat occurs almost synchronously and cannot be distinguished.

[2]Archibald Hill was awarded the 1922 Nobel prize for Physiology or Medicine for the discovery relating to heat production in muscles.

6. **Resting heat production**: The heat produced by resting (passive) muscle is appreciable with the resting heat production of skeletal muscle accounting for half of the total body basal metabolic rate. Further, the rate of heat production for cardiac muscle is five times greater than that of an equivalent mass of skeletal muscle. Resting heat production is increased with a muscle is stretched. This is known as the ***Feng*** effect. It is unclear the exact cause of this resting heat but the activity of the background sodium-potassium pump has been shown to contribute only a small amount to this resting heat production. It is argued that resting heat production may be due to protein synthesis.

1.3 Fading Memory Model

We will now move away from biophysical models of muscle (e.g. Huxley (1957) or Huxley & Simmons (1971)) and investigate a continuum model of muscle mechanics. For the moment we will only be concerned with tetanised muscle.

Under steady state conditions muscle has a tension-length relationship as shown in Figures 1.21 and 1.27. We define now the length ratio λ as the actual muscle length divided by the resting length i.e. λ is 1.0 at the muscle resting length. We will derive the model from the point of view of a isometric quick release experiment i.e. a change in the length of muscle whilst at steady state.

Let $Q(T, T_0)$ be some, as yet unspecified, non-linear function of T, T_0 such that $Q(T_0, T_0) = 0$. Consider now the effect of a change in length, $\Delta\lambda$, at a time $\tau(< t)$ on the current response at time t. The change in Q (at time t) resulting from this length step (at time τ) is

$$
\begin{aligned}
\Delta Q &= \Phi(t-\tau)\,\Delta\lambda \\
&= \Phi(t-\tau)\,\frac{d\lambda(\tau)}{dt}dt
\end{aligned}
$$

where $\Phi(t)$ is the material response function, that is $\Phi(t-\tau)$ is the response at time t to a stimulus at time τ. Integrating we have

$$Q(t) = \int_{-\infty}^{t} \Phi(t-\tau)\,\dot{\lambda}(\tau)\; dt \tag{1.19}$$

This type of integral is known as a hereditary integral.

Now if we assume that the overall response depends more on recent events that earlier events — that is the material has a “fading memory” — and if we assume superposition (i.e. linearity) it is customary to put the material responds function to be

$$\Phi(t-\tau) = \sum_{i=1}^{N} A_i e^{-\alpha_i t} \tag{1.20}$$

where α_i are the rate constants for the material. Equation (1.19) now becomes

$$Q(T(t), T_0) = \sum_{i=1}^{N} A_i \int_{-\infty}^{t} e^{-\alpha_i(t-\tau)}\dot{\lambda}(\tau)\; d\tau \tag{1.21}$$

We need to use experimental results to determine what form Q has, how many N’s are needed and what the values of A_i and α_i are. There are four types of tests that can be used to reveal Q, α_i and A_i:

1. Step changes in length — relaxation test (transient response test)
2. Step changes in tension — creep test (transient response test)
3. Frequency response test
4. Wave propagation test

As the length step is the most common in the literature for single fibre experiments we will use this to define the model then we can use other tests to verify the model.

Consider two length step experiments as shown in Figure 1.32. By using a Heavyside and Dirac delta functions we can put $\lambda = \Delta\lambda H_0(\tau) + \lambda_0$ and $\dot{\lambda} = \Delta\lambda\delta(\tau)$.

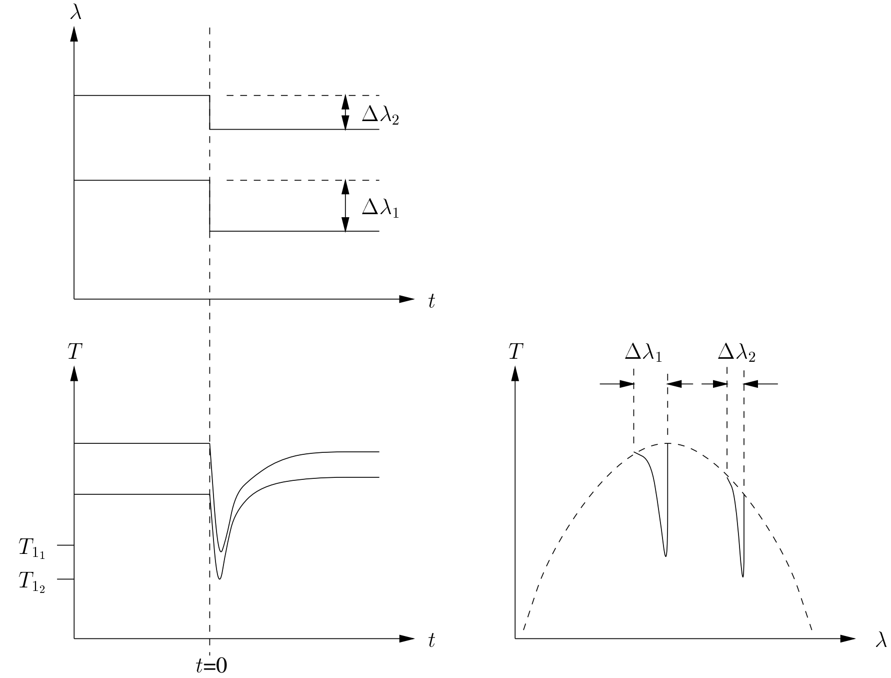

FIGURE 1.32: Two step-length experiments.

Substituting this into Equation (1.19) we obtain

$$Q\left(T\left(t\right), T_0\right) = \Delta\lambda \sum_{i=1}^{N} A_i \int_{-\infty}^{t} e^{-\alpha_i (t-\tau)} \delta\left(\tau\right)\, d\tau$$

Now defining $t = 0$ as the instance of the length step we have

$$Q\left(T\left(t\right), T_0\right) = \Delta\lambda \sum_{i=1}^{N} A_i e^{-\alpha_i t}$$

At $t = 0$ (immediately after the step) $T = T_{1_j}$, that is minimum tension is reached. Hence

$$Q\left(T_{1_j}, T_0\right) = \Delta\lambda_j \sum_{i=1}^{N} A_i \qquad (1.22)$$

Experimentally we find the result as shown in Figure 1.33.

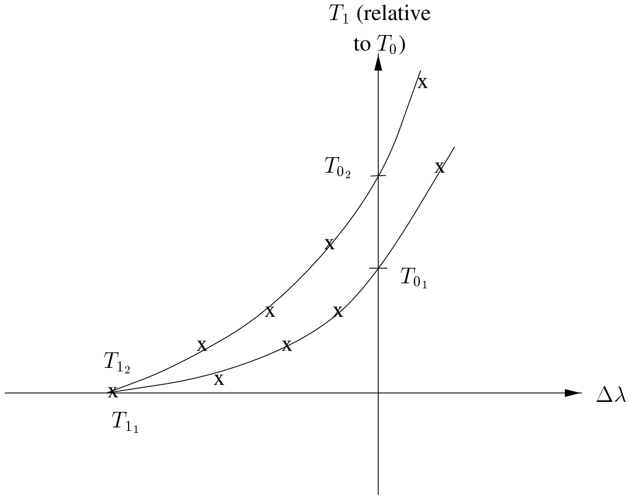

FIGURE 1.33: Experimental results of step length experiments.

It is found that all these curves superimpose if the isometric points are the same (that is all curves are scaled by T_0). This is a consequence of the number of available cross-bridges at different

lengths (i.e. each crossbridge is an independent force generator so tension is proportional to the number of active cross-bridges). We can therefore put

$$Q\left(T_1, T_0\right) = Q\left(\frac{T_1}{T_0}\right)$$

From the experimental data we find we can fit the results with

$$Q\left(T_1, T_0\right) = \frac{T_1/T_0 - 1}{T_1/T_0 + a}$$

where a is a parameter (the curvature of the curve). Hence the general form for the Q function is

$$Q\left(T, T_0\right) = \frac{T/T_0 - 1}{T/T_0 + a} \qquad (1.23)$$

Fitting to data from Huxley and Simmons we find that $a = 2$ and $\sum A_i = 81$ (both non-dimensional).

With Q defined in Equation (1.23), the complete tension recovery following the length step is given by

$$\frac{T/T_0 - 1}{T/T_0 + a} = \Delta\lambda \sum_{i=1}^{N} A_i e^{-\alpha_i t} \qquad (1.24)$$

Consider now a length step of $\Delta\lambda = -0.007$ (i.e. a 0.7% shortening). The results of this experiment are shown in Figure 1.34.

From Figure 1.34 the slow recovery is modelled by Equation (1.24) with $\alpha_1 = 32\ \mathrm{m\,s^{-1}}$ and $A_1 = 17$. The slow recovery phase is associated with cross-bridge cycling. This gives good agreement with the experimental results for $t > 20$ ms.

For $t < 20$ ms we need a 2$^{\text{nd}}$ order process (i.e. α_2, α_3, A_2 and A_3), with $\alpha_2 = 1\ \mathrm{m\,s^{-1}}$, $A_2 = 26$, $\alpha_3 = 5\ \mathrm{m\,s^{-1}}$ and $A_3 = 42$. This fast recovery phase is associated with attached cross-bridge head dynamics (head rotation etc.). The final model is hence

$$\frac{T/T_0 - 1}{T/T_0 + a} = \sum_{i=1}^{3} A_i \int_{-\infty}^{t} e^{-\alpha_i (t-\tau)} \dot{\lambda}\left(\tau\right)\, d\tau \qquad (1.25)$$

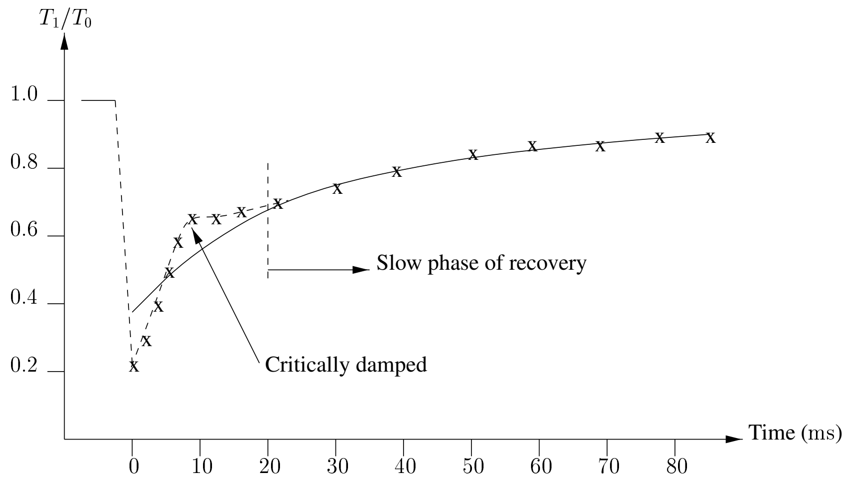

FIGURE 1.34: Time response of tension recovery following a length step.

This model gives good agreement with experiment for a large range of $\Delta\lambda$ (but not too large or fast).

1.3.1 Finite duration length step

In practice the time take for the tension to fall to T_1 following a length step is not zero. We will consider now the case when the muscle takes a finite duration (Δt) for the tension to drop. The velocity of shortening is now given by

$$\dot{\lambda} = \begin{cases} 0 & t < 0 \\ \Delta\lambda/\Delta t & 0 < t < \Delta t \\ 0 & t > \Delta t \end{cases}$$

Equation (1.25) now becomes

$$\begin{aligned} \frac{T/T_0 - 1}{T/T_0 + a} &= \sum_{i=1}^{3} A_i \int_{-\infty}^{\Delta t} e^{-\alpha_i (t-\tau)} \frac{\Delta\lambda}{\Delta t}\, d\tau \\ &= \Delta\lambda \sum_{i=1}^{3} A_i e^{-\alpha_i t} \frac{\left(e^{\alpha_i \Delta t} - 1\right)}{\alpha_i} \Delta t \end{aligned}$$

At $t = \Delta t$ this becomes

$$\frac{T/T_0 - 1}{T/T_0 + a} = \Delta\lambda \sum_{i=1}^{3} A_i \frac{\left(1 - e^{-\alpha_i \Delta t}\right)}{\alpha_i} \Delta t \tag{1.26}$$

The effects of Δt on the tension response are shown in Figure 1.35.

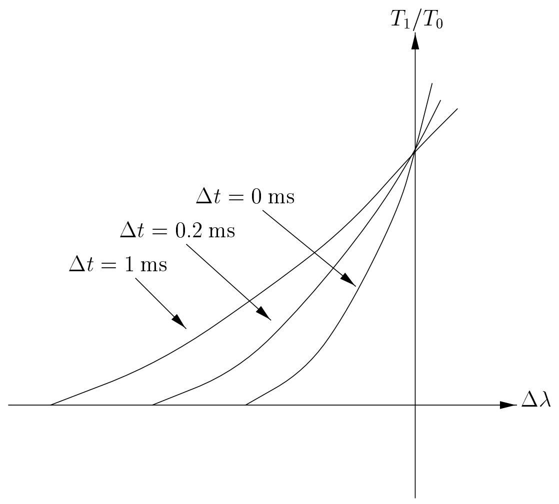

FIGURE 1.35: Effects of the time taken for a length step.

1.3.2 Force step response

Consider now the response to a force step. For the moment we will consider the case were we are initially at the plateau of the force-length relationship (i.e. $\lambda \approx 1$ and $T(\lambda) \approx$constant). The experimental results are shown in Figure 1.36.

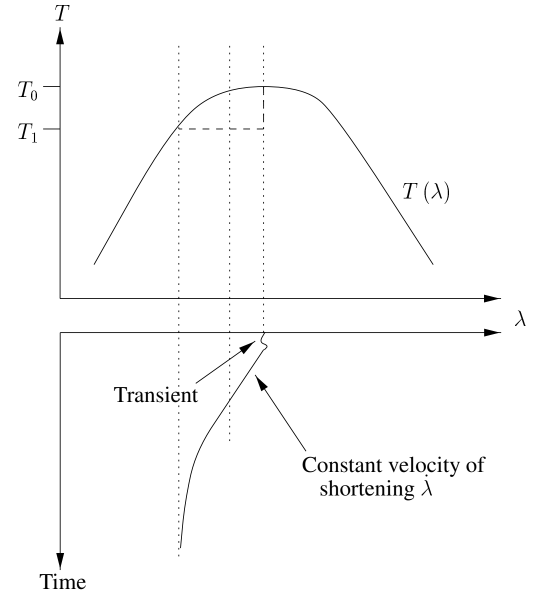

FIGURE 1.36: Effects of the time taken for a force step.

Consider one time constant only (i.e. N=1) and the region where $\dot{\lambda}$ constant. Hence

$$\begin{aligned}\frac{T/T_0 - 1}{T/T_0 + a} &= A_1 \int_{-\infty}^{t} e^{-\alpha_1(t-\tau)}\dot{\lambda}\, d\tau \\ &= A_1 e^{-\alpha_1 t}\dot{\lambda} \int_{-\infty}^{t} e^{\alpha_1 \tau}\, d\tau \\ &= \frac{A_1}{\alpha_1}\dot{\lambda}\end{aligned} \tag{1.27}$$

This is shown in Figure 1.37.

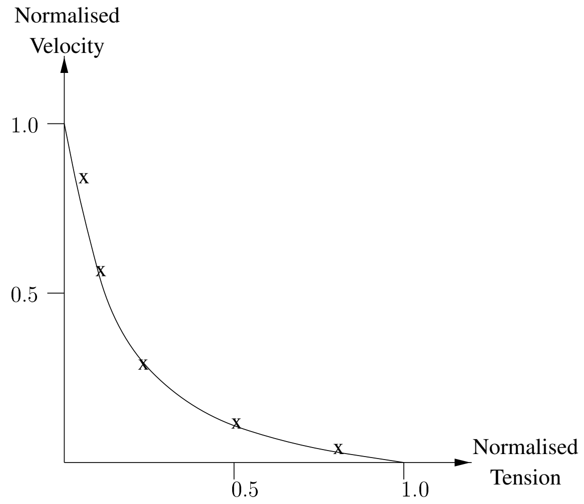

FIGURE 1.37: Force-velocity relationship for the fading memory model.

Now if we let $\hat{a} = aT_0$ and $\hat{b} = -\frac{\alpha_1}{A_1}$ then Equation (1.27) becomes

$$V = \frac{\hat{b}(T_0 - T)}{T + \hat{a}}$$

which is the same as Hill's equation for velocity, Equation (1.15).

Consider now the case when isometric tension $T_0(\lambda)$ varies with length in the region of interest (i.e. we are on the ascendening or descending limb of the force-length relationship). We will consider only one time constant (i.e. $N = 1$) and start with

$$\frac{T/T_0 - 1}{T/T_0 + a} = A_1 \int_{-\infty}^{t} e^{-\alpha_1(t-\tau)} \dot{\lambda}\, d\tau$$

We now differentiate with respect to t, holding T constant to extract an expression for $\dot{\lambda}$. To do this we must make use of *Leibnitz's rule* for differentiating and integral with respect to one of its limits. Leibnitz's rule is

$$\frac{d}{dt}\left\{\int_{g(t)}^{h(t)} f(x,t)\, dx\right\} = \int_{g(t)}^{h(t)} \frac{\partial f(x,t)}{\partial t}\, dx + f(h(t), t)\frac{dh}{dt} - f(g(t), t)\frac{dg}{dt}$$

hence

$$\frac{(T/T_0 + a).1 - (T/T_0 - 1).1}{(T/T_0 + a)^2} \cdot \frac{-T}{T_0^2}\frac{dT_0}{d\lambda}\dot{\lambda} = \alpha_1 \frac{T/T_0 - 1}{T/T_0 + a} + A_1 \dot{\lambda}$$

therefore

$$\dot{\lambda} = \frac{\alpha_1 \dfrac{T/T_0 - 1}{T/T_0 + a}}{A_1 + \dfrac{1+a}{(T/T_0 + a)^2}\dfrac{T}{T_0^2}\dfrac{dT_0}{d\lambda}} \qquad (1.28)$$

Note that Equation (1.28) collapses to Equation (1.27) when $\dfrac{dT_0}{d\lambda} = 0$. This result is shown in Figure 1.38.

It should be noted now that the force-velocity curve depends on λ as shown in Figure 1.39.

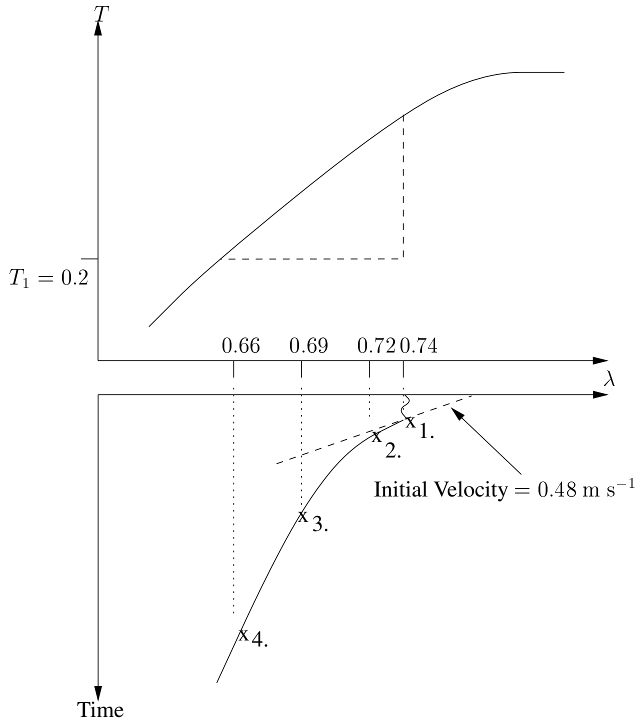

FIGURE 1.38: Effects of the time taken for a force step.

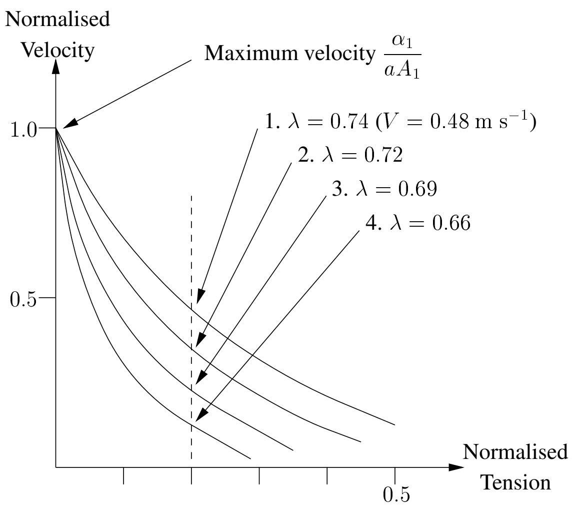

FIGURE 1.39: Fading memory force-velocity relationship for different extension ratios.

Chapter 2

Cardiac Electrophysiology

2.1 Cardiac cells

The cardiac cell membrane is more complicated that that of the squid axon. Consider the idealised cardiac cell shown in Figure 2.1. In addition to the sodium and potassium channels cardiac cells (like other muscle cells) also have calcium channels. Calcium plays an important role in muscle contraction and will be covered in more detail in Section 1.2.4. For now we will just say that the level of contraction of a muscle is directly dependent on the amount of calcium in the cell. The more the calcium the more the contraction.

We will now consider each of the currents and ion pumps in turn. In particular we will interpret the currents in the same manner as DiFrancesco & Noble (1985).

2.2 Units

One of the main difficulties encountered when modelling cardiac electrical activity is that many of the models, both cellular and distributed have different sets of units. The following standard sets of units have been used for models presented here Table 2.1.

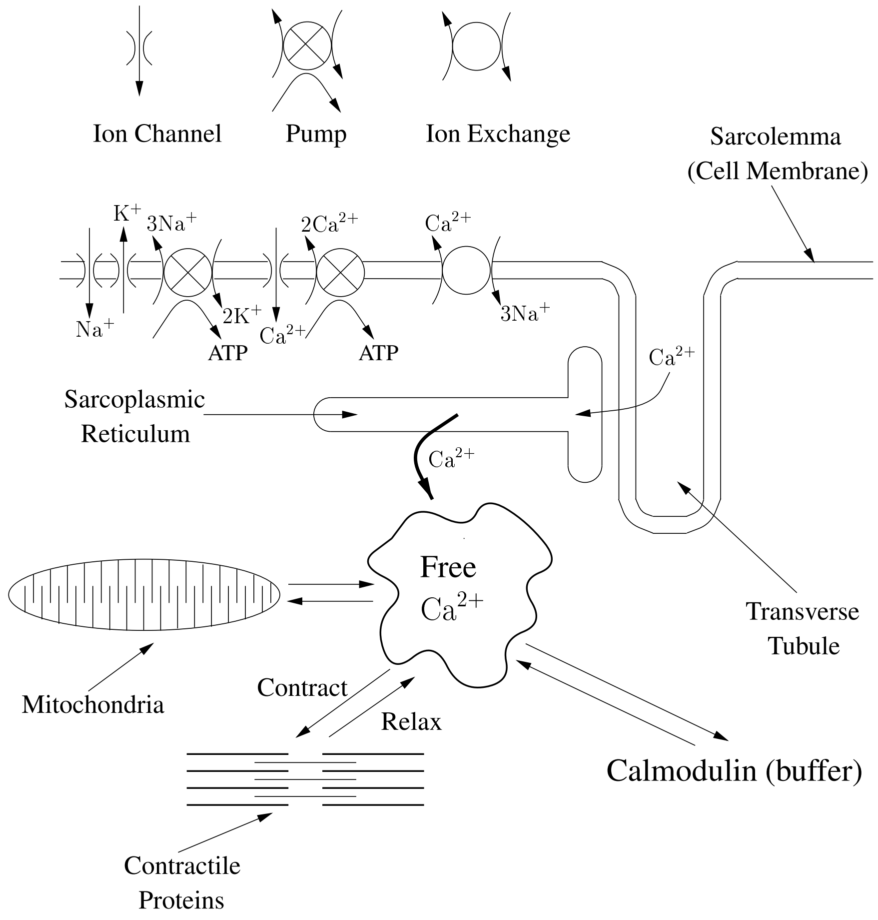

FIGURE 2.1: Idealised cardiac cell.

Parameter	*Units*
Length	mm
Area	mm^2
Volume	mm^3
Time	ms
Voltage	mV
Current	$\mu\mathrm{A}$
Conductivity	mS
Membrane conductance	$\mathrm{mS\ mm}^{-2}$
Tissue conductivity	$\mathrm{mS\ mm}^{-1}$
Current density	$\mu\mathrm{A\ mm}^{-2}$
Volume current	$\mu\mathrm{A\ mm}^{-3}$
Charge	nC
Capacitance	$\mu\mathrm{F}$
Specific capacitance	$\mu\mathrm{F\ mm}^{-2}$
Concentration	$\mathrm{nmol\ mm}^{-3} = \mathrm{mM}$
Energy	pJ
Temperature	K

TABLE 2.1: The consistent set of units chosen for all models

2.2.1 Cardiac Ionic Currents

There are six main ionic currents in the diFrancesco-Noble model of cardiac electrical activity. These currents are shown graphically in Figure 2.2.

1. Fast sodium current, i_{Na}: Inward, fast, time dependent, m^3h gates. Activates at $-60\ \mathrm{mV}$. Inactivation is very fast and is complete by the time the membrane repolarises to $+30$ mV. Blocked by Tetrodotoxin (TTX) from puffer fish.

2. Secondary inward calcium current, i_{si}: Inward, slow, time dependent, d & f gates. Activates at $-40\ \mathrm{mV}$. This current is very small in the Purkinje fibres but is enhanced by nor-adrenaline which enable the Purkinje fibres to support pacemaker activity alone. Blocked by Nifedipine and Verapamil.

3. Time independent background potassium current, i_{K1}: Outward, time independent. Inward rectifier. At membrane potentials between 0 and E_K the current is outward (repolarising), but falls drastically at membrane potentials above $0\ \mathrm{mV}$. This prevents an inefficient loss of K^+ ions during the action potential. This current is not present in the SA node. The high conductance of this channel at -'ve membrane potential is responsible

for the resting potential of $-85\ \mathrm{mV}$ for cardiac cells.

4. Transient outward current, i_{to}: time dependent, r gates. When activated in sufficient quantities it is characterised by a repolarising notch. It involves mainly K^+ ions. It is activated by intra-cellular calcium.

5. Time dependent potassium current, i_K or i_x: Outward, x gates. Activates at +'ve membrane potential and deactivates at -'ve membrane potential. It behaves as a delayed rectifier and hence repolarises membrane. It has slow kinetics which results in a long action potential.

6. Hyperpolarising-activated current, i_f: Inward, Time independent. Activated at -'ve membrane potentials and deactivated at +'ve membrane potentials. Reversal potential at -30 mV hence the current is inward at the resting potential.

2.3 Ion Pumps and Exchanges

There are two main ion pumps and one ion exchanger in cardiac cells.

1. Sodium-Potassium pump , i_{NaK}: Pumps $3\ \mathrm{Na}^+$ ions out of the cell and brings in $2\ \mathrm{K}^+$ ions. It is *electrogenic*, that is there is a net transfer of charge, and ATP (Adenosine Tri-Phosphate) dependent. It is blocked by the cardiac glycosides (e.g. digitalis, ouabain) and vanadium. It is this pump that maintains the resting potential. The density of the sodium pump is about 400 per $\mu\mathrm{m}^2$ of sarcolemma ($\sim 10^6$ in a cell), compared with 16 for the sodium channel and 0.1 for the calcium channel.

2. Calcium pump: Mainly in the sarcoplasmic reticulum. ATP dependent. It is much slower than the sodium-calcium exchange.

3. Sodium-Calcium exchange, i_{NaCa}: Transfers $3\ \mathrm{Na}^+$ ions into of the cell and removes 1 Ca^{2+} from the cell. Works on a concentration gradient and is hence enhanced by increased $[\mathrm{Ca}^{2+}]_i$ or $[\mathrm{Na}^+]_o$. It is not ATP dependent and is faster and about 30 times more effective that the calcium pump. It is voltage dependent and has a reversal potential of $+20\ \mathrm{mV}$.

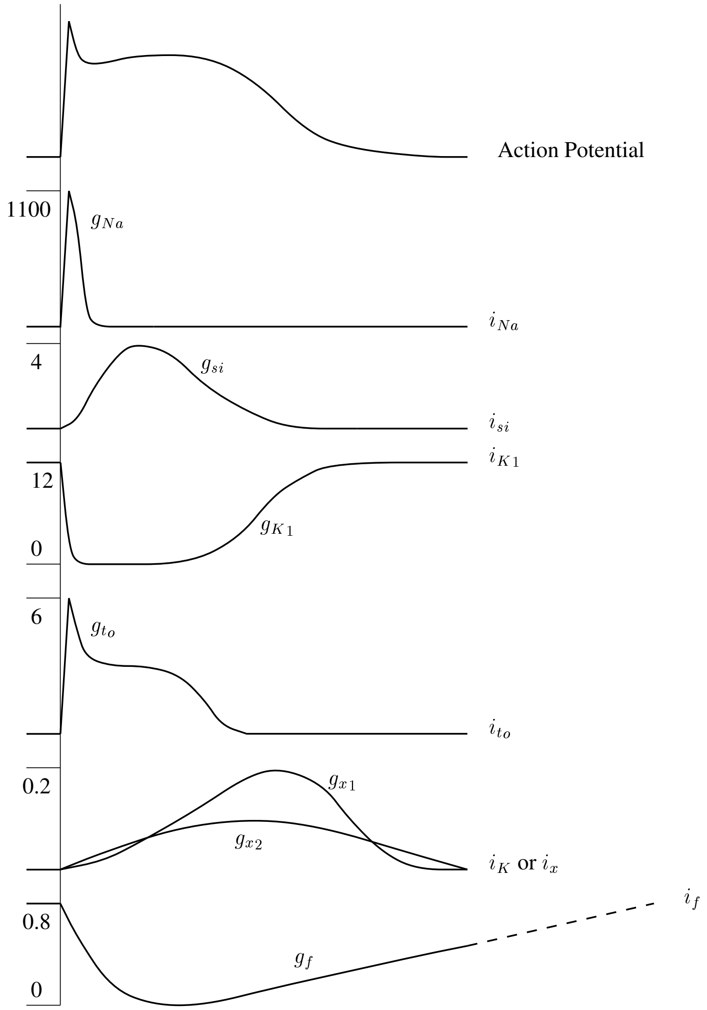

FIGURE 2.2: diFrancesco-Noble currents making up the cardiac action potential. Note all conductances are $10^{-4}\mathrm{S/cm^2}$.

2.4 diFrancesco-Noble Model

The diFrancesco-Nobel model of the cardiac action potential is summarised by Figure 2.3.

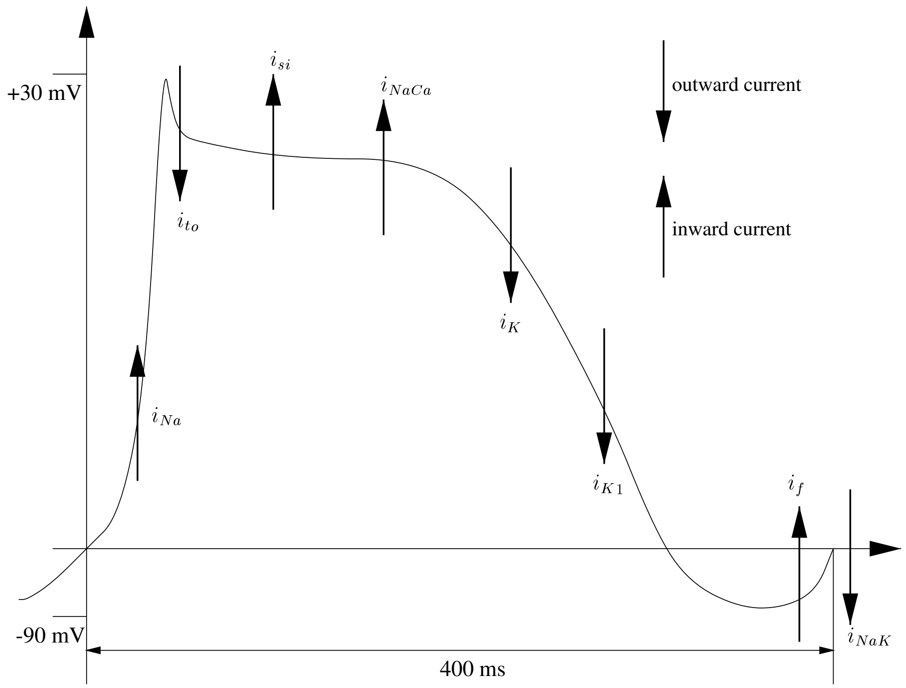

FIGURE 2.3: diFrancesco-Noble action potential currents for cardiac cells.

2.5 Changes in the action potential

Consider the following changes in the action potential

1. Increase in extra-cellular calcium. Intra-cellular calcium is increased as more calcium enters the cell from the extra-cellular space. Force is hence increased due to the increased

intra-cellular calcium. The action potential is prolonged because the intra-cellular calcium is increased. This results in an increase in the sodium calcium exchange current prolonging the plateau of the action potential.

2. Decrease in extra-cellular sodium. Force increases as the sodium-calcium exchange is decreased resulting in increased intra-cellular calcium. The action potential is shortened.

3. Addition of Nifedipine (a calcium channel blocker). Force is decreased as calcium cannot enter the cell to interact with the contractile proteins. The action potential is shortened due to the decrease in the secondary inward calcium current and decrease in the sodium-calcium exchange.

4. Addition of Digitalis (which inhibits the $3\mathrm{Na}^+$/$2\mathrm{K}^+$ pump). Force is increased as intra-cellular sodium is increased which results in a decreased calcium efflux through the sodium-calcium exchange.

5. Addition of caffeine (releases calcium from the mitochondria). Increases the intra-cellular calcium and hence increases force. The action potential plateau is extended as the increased intra-cellular calcium is removed via the sodium-calcium exchange. This is shown in Figure 2.4.

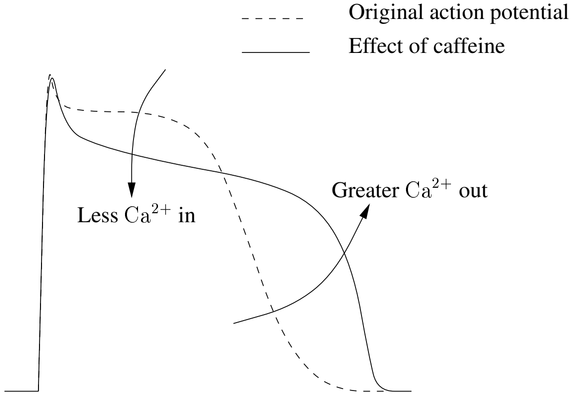

FIGURE 2.4: Effect of caffeine on the cardiac action potential.

2.6 Other membrane models

2.6.1 The Beeler-Reuter model

There are many other models of cellular electrophysiology, and we present some of them here. The Beeler-Reuter is the simplist physiologically-based model. The model developed by Beeler and Reuter (Beeler & Reuter 1977) is specifically a model of mammalian ventricular myocardial cells. The standard model is based around ionic current densities across $1\mathrm{cm}^2$ so it was necessary to convert the units of the ionic currents and also the calcium ion concentration. Four currents are present in the model, they are an fast inward sodium current, I_{Na}, an outward time independent potassium current, I_{K1}, a time dependent outward current based mainly on potassium ions, I_{x1} and a slow inward current I_s which is mainly due to calcium ion transfer. The ionic current model may be written as

$$I_{ion} = I_{Na} + I_{K1} + I_{x1} + I_s \tag{2.1}$$

All currents in the model have been converted into units of $\mu\mathrm{A\ mm}^{-2}$ to maintain consistency

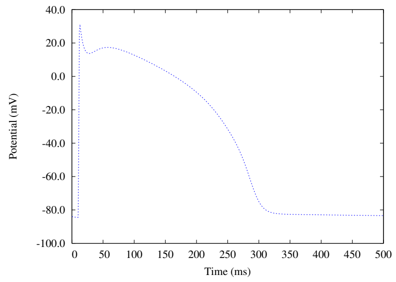

FIGURE 2.5: Action potential trace from the Beeler-Reuter ionic current model.

with the diffusive processes. I_{Na} was responsible for the fast upstroke of the action potential and I_s was responsible for the duration of the plateau phase. The two potassium currents, I_{K1} and I_{x1} were responsible for the repolarization of the cell. The action potential generated by the Beeler-Reuter model is shown in Figure 2.5.

Fast inward sodium current

The fast inward sodium current is controlled by three gating variables which follow the standard Hodgkin-Huxley formulation. The m gate is the activation gate and the h gate is the inactivation gate. In addition to this there is a slow inactivation gate j. The magnitude of this current was defined to be

$$I_{Na} = \left(\overline{g_{Na}} \cdot m^3 \cdot h \cdot j + \overline{g_{NaC}}\right) \cdot (V_m - E_{Na}) \tag{2.2}$$

where E_{Na} is the sodium reversal potential which was set at $50\mathrm{mV}$ and $\overline{g_{Na}}$ is the fully activated sodium conductance at $4 \times 10^{-2}\mathrm{mS\ mm}^{-2}$. $\overline{g_{NaC}}$ is the steady state sodium conductance which was set to be $3 \times 10^{-5}\mathrm{mS\ mm}^{-2}$. The time dependence of the gating variables was defined as

$$\frac{dm}{dt} = \alpha_m \cdot (1 - m) - \beta_m \cdot m \tag{2.3}$$

$$\frac{dh}{dt} = \alpha_h \cdot (1 - h) - \beta_h \cdot h \tag{2.4}$$

$$\frac{dj}{dt} = \alpha_j \cdot (1 - j) - \beta_j \cdot j \tag{2.5}$$

where the rate constants were given by

$$\alpha_m = \frac{-\left(V_m + 47\right)}{\exp\left(-0.1\left(V_m + 47\right)\right) - 1} \tag{2.6}$$

$$\beta_m = 40 \exp\left(-0.056\left(V_m + 72\right)\right) \tag{2.7}$$

$$\alpha_h = 0.126 \exp\left(-0.25\left(V_m + 77\right)\right) \tag{2.8}$$

$$\beta_h = \frac{1.7}{\exp\left(-0.082\left(V_m + 22.5\right)\right) + 1} \tag{2.9}$$

$$\alpha_j = 0.055 \left[\frac{\exp\left(-0.25\left(V_m + 78\right)\right)}{\exp\left(-0.2\left(V_m + 78\right)\right) + 1}\right] \tag{2.10}$$

$$\beta_j = \frac{0.3}{\exp\left(-0.1\left(V_m + 32\right)\right) + 1} \tag{2.11}$$

The fast inward sodium current and the gating variables are shown in Figure 2.6.

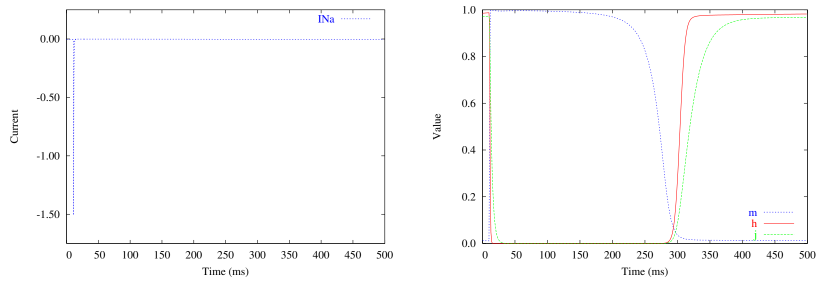

(a) (b)

FIGURE 2.6: Figure(a) shows the fast inward sodium current over time and Figure(b) shows the m, h and j gate variables over time from the Beeler-Reuter model.

Time independent outward potassium current

The magnitude of the time independent outward potassium current, I_{K1} was given by

$$I_{K1} = 0.0035 \left[\frac{4\left(\exp\left(0.04\left(V_m + 85\right)\right) - 1\right)}{\exp\left(0.08\left(V_m + 53\right)\right) + \exp\left(0.04\left(Vm + 53\right)\right)} + \frac{0.2\left(V_m + 23\right)}{1 - \exp\left(-0.04\left(V_m + 23\right)\right)}\right] \tag{2.12}$$

and the temporal trace of the current is shown in Figure 2.7.

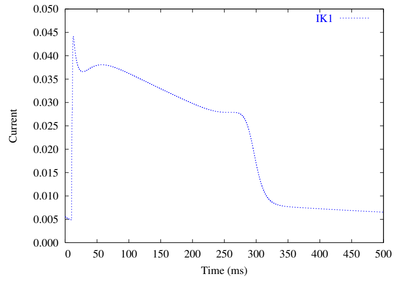

FIGURE 2.7: The time independent outward potassium current from the Beeler-Reuter model.

Time dependent outward potassium current

The time dependent outward potassium current was controlled by a single Hodgin-Huxley type gating variable, x_1.

$$I_{x1} = 8 \times 10^{-3} \cdot x_1 \cdot \left[\frac{\exp\left(0.04\left(V_m + 77\right)\right) - 1}{\exp\left(0.04\left(V_m + 35\right)\right)}\right] \tag{2.13}$$

where the time dependence of x_1 was defined to be

$$\frac{dx_1}{dt} = \alpha_{x1} \cdot (1 - x_1) - \beta_{x1} \cdot x_1 \tag{2.14}$$

The rate constants were calculated from

$$\alpha_{x1} = 5 \times 10^{-4} \left[\frac{\exp\left(0.083\left(V_m + 50\right)\right)}{\exp\left(0.057\left(V_m + 50\right) + 1\right)}\right] \tag{2.15}$$

$$\beta_{x1} = 1.3 \times 10^{-3} \left[\frac{\exp\left(-0.06\left(V_m + 20\right)\right)}{\exp\left(-0.04\left(V_m + 20\right) + 1\right)}\right] \tag{2.16}$$

The size of the current and state of the gating variable over time are shown in Figure 2.8.

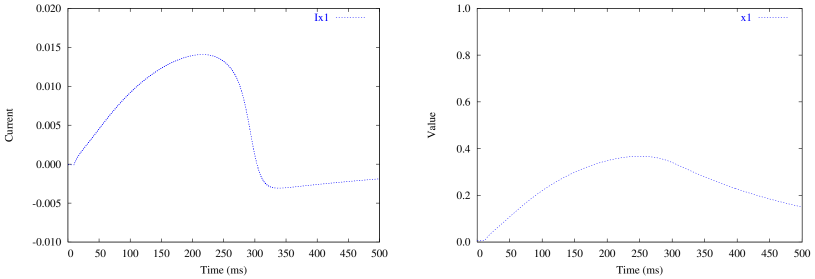

(a) (b)

FIGURE 2.8: Figure(a) shows the time dependent outward potassium current over time and Figure(b) shows the x_1 gate variable over time from the Beeler-Reuter model.

Slow inward current

The slow inward current was based mainly around the uptake of calcium ions into the cell. The current features an activation gate d and an inactivation gate f. The ionic current was represented by

$$I_s = \overline{g_s} \cdot d \cdot f \cdot (V_m - E_s) \tag{2.17}$$

where $\overline{g_s}$ is the fully activated channel conductance which was set to be $9 \times 10^{-4}\mathrm{mS\ mm}^{-2}$. The reversal potential for the current was dependent on the concentration of calcium ions present in the cell.

$$E_s = -82.3 - 13.0287 ln\left(0.001[\mathrm{Ca}^{2+}]_i\right) \tag{2.18}$$

The time dependence of the intracellular calcium concentration was governed by

$$\frac{d[\mathrm{Ca}^{2+}]_i}{dt} = -0.01 I_s + 0.07\left(1 \times 10^{-4} - [\mathrm{Ca}^{2+}]_i\right) \tag{2.19}$$

and the concentration is shown in Figure 2.9. The two gating variables were calculated using

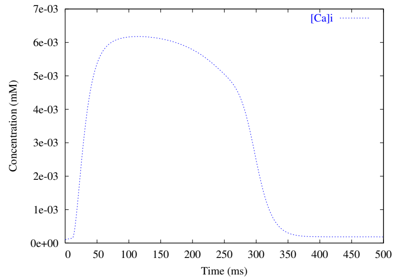

FIGURE 2.9: The intracellular calcium ion concentration from the Beeler-Reuter model.

$$\frac{dd}{dt} = \alpha_d \cdot (1 - d) - \beta_d \cdot d \tag{2.20}$$

$$\frac{df}{dt} = \alpha_f \cdot (1 - f) - \beta_f \cdot f \tag{2.21}$$

The values of the rate constants were found from

$$\alpha_d = 0.095 \left[\frac{\exp\left(-0.01\left(V_m - 5\right)\right)}{\exp\left(-0.072\left(V_m - 5\right)\right) + 1} \right] \tag{2.22}$$

$$\beta_d = 0.07 \left[\frac{\exp\left(-0.017\left(V_m + 44\right)\right)}{\exp\left(0.05\left(V_m + 44\right)\right) + 1} \right] \tag{2.23}$$

$$\alpha_f = 0.012 \left[\frac{\exp\left(-0.008\left(V_m + 28\right)\right)}{\exp\left(0.15\left(V_m + 28\right)\right) + 1} \right] \tag{2.24}$$

$$\beta_f = 0.0065 \left[\frac{\exp\left(-0.02\left(V_m + 30\right)\right)}{\exp\left(-0.2\left(V_m + 30\right)\right) + 1} \right] \tag{2.25}$$

The magnitude of the current and the state of the gating variables over time is shown in Figure 2.10. The initial values of the gating variables were calculated from the initial value of the

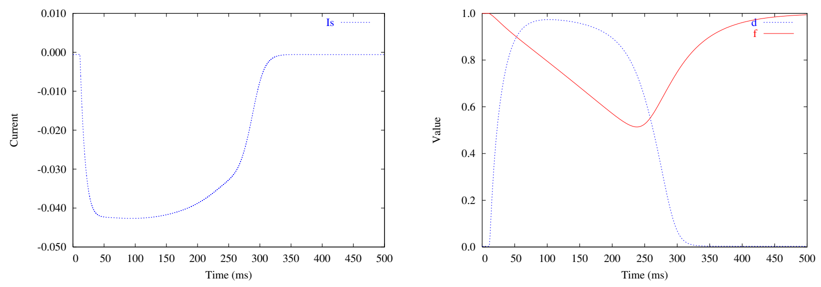

(a) (b)

FIGURE 2.10: Figure(a) shows the slow inward current over time and Figure(b) shows the d and f gate variables over time from the Beeler-Reuter model.

transmembrane potential. The initial value for a gate i was given by

$$i = \frac{\alpha_i}{\alpha_i + \beta_i} \tag{2.26}$$

The values of the other parameters used in the Beeler-Reuter model whose values have not yet been specified are given in Table 2.2.

Parameter	*Value*	*Units*
V_m	-84.0	mV
$[\mathrm{Ca}^{2+}]_i$	1×10^{-4}	nmol mm^{-3}
C_m	0.01	μF mm^{-2}
A_m	200	mm^{-1}

TABLE 2.2: Parameter values used in the Beeler-Reuter model

2.6.2 The defibrillation Beeler-Reuter model

The original Beeler-Reuter model was modified by Drouhard and Roberge to improve the fast sodium current kinetics. This model was then further modified by Skouibine, Trayanova & Moore (1999) to handle voltages outside the range of normal physiological activity for use with defibrillation studies. The action potential for the defibrillation Beeler-Reuter model is shown in Figure 2.11.

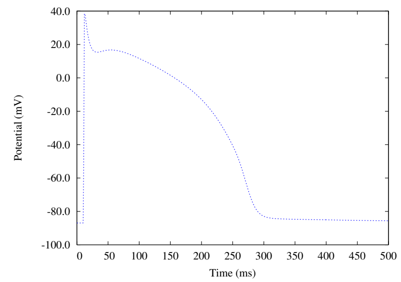

FIGURE 2.11: Action potential trace from the defibrillation Beeler-Reuter ionic current model.

Fast inward sodium current

The steady state sodium conductance, $\overline{g_{NaC}}$ was removed along with the slow inactivation gating variable j leaving the following equation for the fast inward sodium current.

$$I_{Na} = \overline{g_{Na}} \cdot m^3 \cdot h \cdot (V_m - E_{Na}) \tag{2.27}$$

where E_{Na} was set to $40\mathrm{mV}$ which is smaller than the standard Beeler-Reuter model and $\overline{g_{Na}}$ was set to $0.15\mathrm{mS\ mm}^{-2}$, nearly four times larger than in the original model. The gating variables were altered to cope with the large potentials encountered during defibrillation.

$$
\begin{aligned}
\alpha_m &= \begin{cases} 0.9\left[\dfrac{V_m + 42.65}{1 - \exp\left((-0.22V_m - 9.3830)\right)}\right] & \text{if } V_m \le 100\text{mV} \\ 890.9437890\left[\dfrac{\exp\left((0.0486479V_m - 4.8647916)\right)}{1 + 5.93962526\exp\left((0.0486479V_m - 4.8647916)\right)}\right] & \text{if } V_m > 100\text{mV} \end{cases} \\
\beta_m &= \begin{cases} 1.437\exp\left((-0.085V_m - 3.37875)\right) & \text{if } V_m > -85\text{mV} \\ \dfrac{100}{1 + \exp\left((0.2597504V_m + 22.0787804)\right)} & \text{if } V_m \le -85\text{mV} \end{cases} \\
\alpha_h &= \begin{cases} 0.1\exp\left((-0.193V_m - 15.37245)\right) & \text{if } V_m > -90\text{mV} \\ -12.0662845 - 0.1422598V_m & \text{if } V_m \le -90\text{mV} \end{cases} \\
\beta_h &= \begin{cases} \dfrac{1.7}{1 + \exp\left((-0.095V_m - 1.9475)\right)} & \text{for all } V_m \end{cases}
\end{aligned} \tag{2.28}
$$

The fast inward sodium current and the gating variables are shown in Figure 2.12.

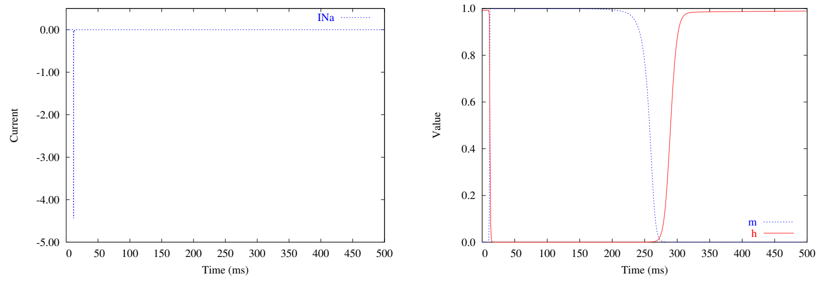

(a) (b)

FIGURE 2.12: Figure(a) shows the fast inward sodium current over time and Figure(b) shows the m, and h gating variables over time from the defibrillation Beeler-Reuter model.

Time independent outward potassium current

The formula for time independent outward potassium current was unchanged. The time course of the current is shown in Figure 2.13

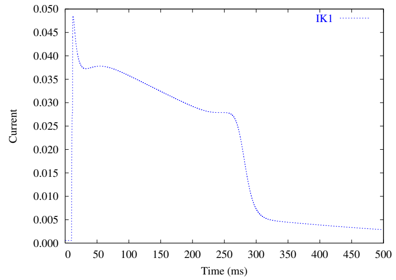

FIGURE 2.13: The time independent outward potassium current from the defibrillation Beeler-Reuter model.

Time dependent outward potassium current

While the governing equations for the time dependent outward potassium current were unchanged, the gating variables were modified to become

$$
\begin{aligned}
\alpha_{x1} &= \begin{cases} 0.0005\left[\dfrac{\exp\left((0.083V_m + 4.150)\right)}{\exp\left((0.057V_m + 2.850)\right) + 1}\right] & \text{if } V_m \le 400\text{mV} \\ 151.7994692\left[\dfrac{\exp\left((0.0654679V_m - 26.1871448)\right)}{1 + 1.5179947\exp\left((0.0654679V_m - 26.1871448)\right)}\right] & \text{if } V_m > 400\text{mV} \end{cases} \\
\beta_{x1} &= \begin{cases} 0.0013\left[\dfrac{\exp\left((-0.06V_m - 1.20)\right)}{\exp\left((-0.04V_m - 0.80)\right) + 1}\right] & \text{for all } V_m \end{cases}
\end{aligned} \tag{2.29}
$$

The size of the current and state of the gating variable over time are shown in Figure 2.14.

Slow inward current

There was a change made to the intracellular calcium ion tracking in order to limit the movement of calcium ions at large potentials.

$$
\frac{d[\text{Ca}^{2+}]_i}{dt} = \begin{cases} -0.01I_s + 0.07\left(1 \times 10^{-4} - [\text{Ca}^{2+}]_i\right) & \text{if } V_m \le 200\text{mV} \\ 0 & \text{if } V_m > 200\text{mV} \end{cases} \tag{2.30}
$$

The time course of the intracellular calcium ion concentration is shown in Figure 2.15.

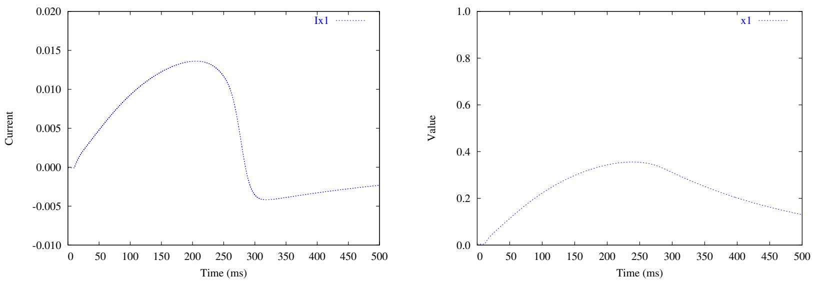

(a) (b)

FIGURE 2.14: Figure(a) shows the time dependent outward potassium current over time and Figure(b) shows the x_1 gate variable over time from the defibrillation Beeler-Reuter model.

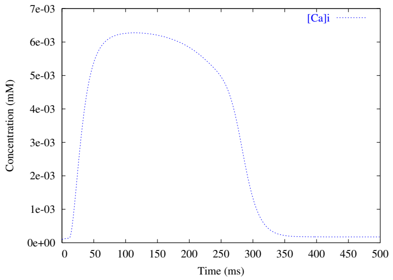

FIGURE 2.15: The intracellular calcium ion concentration from the defibrillation Beeler-Reuter model.

In addition to these changes, in order to simulate ischemic tissue a scale factor was added to the time dependent d and f gates to allow the scaling of the action potential duration. The modified equations became

$$\frac{dd}{dt} = \frac{\alpha_d}{R} \cdot (1 - d) - \beta_d \cdot d \tag{2.31}$$

$$\frac{df}{dt} = \frac{\alpha_f}{R} \cdot (1 - f) - \beta_f \cdot f \tag{2.32}$$

where R was typically in the range of 1 to 8. The slow inward current and associated gating variables are shown in Figure 2.16.

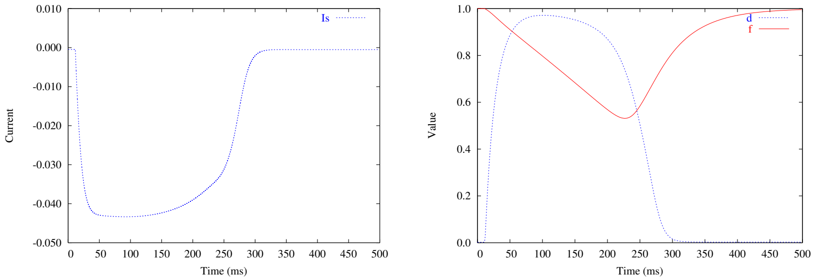

(a) (b)

FIGURE 2.16: Figure(a) shows the slow inward current over time and Figure(b) shows the d and f gate variables over time from the defibrillation Beeler-Reuter model.

2.6.3 The Luo-Rudy models

The Luo-Rudy model (Luo & Rudy 1991) built on the Beeler-Reuter model adjusting the parameters to more recent experimental results and adding more currents to more accurately represent the potassium ion dynamics. Six individual currents were used to describe the cellular processes.

$$I_{ion} = I_{Na} + I_{si} + I_K + I_{K1} + I_{Kp} + I_b \tag{2.33}$$

Three of the currents may be grouped to give an expression for the total time independent potassium current.

$$I_{K1T} = I_{K1} + I_{Kp} + I_b \tag{2.34}$$

A plot of I_{K1T} is shown later in Figure 2.22. In addition to these ionic currents the intracellular calcium ion concentration was tracked due to the calcium uptake by the slow inward current, I_{si}. The action potential produced by the Luo-Rudy model is shown in Figure 2.17.

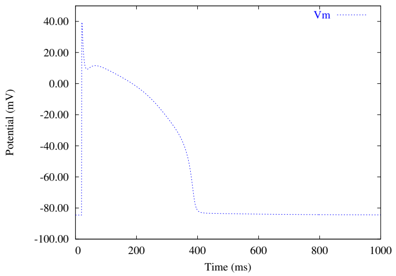

FIGURE 2.17: Action potential trace from the Luo-Rudy ionic current model.

Fast inward sodium current

The general form of the fast inward sodium current is the same as the original Beeler-Reuter model with the omission of the steady state sodium conductance parameter.

$$I_{Na} = \overline{g_{Na}} \cdot m^3 \cdot h \cdot j \cdot (V_m - E_{Na}) \tag{2.35}$$

Here m is the activation gate, h is the fast inactivation gate and j is the slow inactivation gate. The time dependent behaviour of these gates was identical to the Beeler-Reuter model Equations (2.3)–(2.5) but with reformulated rate constants. $\overline{g_{Na}}$ is the maximum sodium conductance and E_{Na} is the reversal potential of the channel as calculated from the Nernst potential for

sodium ions using Equation (2.52). The α and β gating parameters were defined to be

$$\begin{aligned}
\alpha_m &= \frac{0.32(V_m + 47.13)}{1 - \exp(-0.1(V_m + 47.13))} \\
\beta_m &= 0.08 \exp(-V_m/11) \\
\alpha_h &= \begin{cases} 0 & \text{if } V_m \geq -40\text{mV} \\ 0.135 \exp[(-80.0 - V_m)/6.8] & \text{if } V_m < -40\text{mV} \end{cases} \\
\beta_h &= \begin{cases} \frac{1}{0.13(1+\exp[-(V_m+10.66)/11.1])} & \text{if } V_m \geq -40\text{mV} \\ 3.56 \exp(0.079 V_m) + 3.1 \times 10^5 \exp(0.35 V_m) & \text{if } V_m < -40\text{mV} \end{cases} \\
\alpha_j &= \begin{cases} 0 & \text{if } V_m \geq -40\text{mV} \\ \frac{-1.2714\times10^5 \exp(0.2444V_m) - 3.474\times10^{-5} \exp(-0.04391V_m)}{1+\exp(0.311(V_m+79.23))}(V_m + 37.78) & \text{if } V_m < -40\text{mV} \end{cases} \\
\beta_j &= \begin{cases} \frac{0.3 \exp(-2.535\times10^{-7} V_m)}{(1+\exp(-0.1(V_m+32)))} & \text{if } V_m \geq -40\text{mV} \\ \frac{0.1212 \exp(-0.01052V_m)}{(1+\exp(-0.1378(V_m+40.14)))} & \text{if } V_m < -40\text{mV} \end{cases}
\end{aligned} \tag{2.36}$$

The fast inward sodium current and the three gating variables are shown in Figure 2.18.

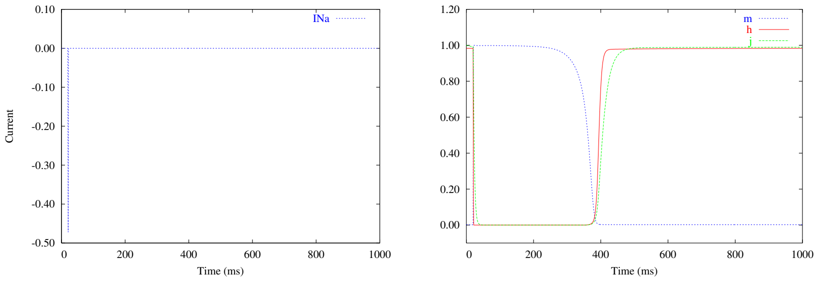

(a) (b)

FIGURE 2.18: Figure(a) shows the fast inward sodium current over time and Figure(b) shows the m, h and j gate variables over time from the Luo-Rudy model.

Slow inward current

The slow inward current was defined by the same formula as the I_s current in the Beeler Reuter model.

$$I_{si} = \overline{g_{si}} \cdot d \cdot f \cdot (V_m - E_{si}) \tag{2.37}$$

The reversal potential was adjusted to be

$$E_{si} = 7.7 - 13.0287 \ln \left([\mathrm{Ca}^{2+}]_i \right) \tag{2.38}$$

and the formulation of the rate constants, α_d,β_d,α_f and β_f were also unchanged. The current trace over time along with the two gates are shown in Figure 2.19.

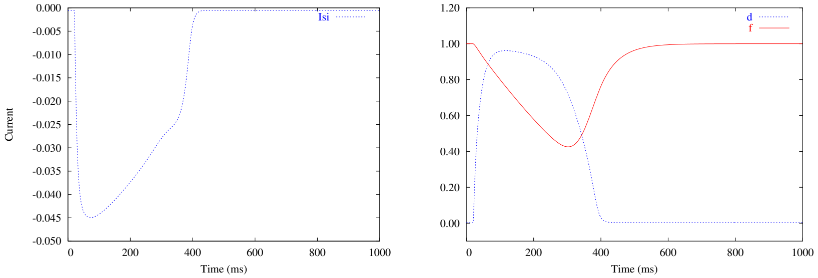

(a) (b)

Figure 2.19: Figure(a) shows the slow inward current over time and Figure(b) shows the d and f gate variables over time from the Luo-Rudy model.

Time dependent potassium current

The time dependent potassium current was controlled by an activation gate, x and an inactivation gate, X_i. The inactivation gate was not formulated as a typical Hodgkin-Huxley differential

equation.

$$I_K = \overline{g_K} \cdot x \cdot X_i \cdot (V_m - E_K) \tag{2.39}$$

where the maximum potassium conductance was calculated from

$$\overline{g_K} = g_K \cdot \sqrt{[\mathrm{K}^+]_o / 5.4} \tag{2.40}$$

The reversal potential was calculated from

$$E_K = \frac{RT}{F} \ln \left(\frac{[\mathrm{K}^+]_o + PR_{NaK} [\mathrm{Na}^+]_o}{[\mathrm{K}^+]_i + PR_{NaK} [\mathrm{Na}^+]_i} \right) \tag{2.41}$$

where PR_{NaK} is a dimensionless permeability ratio. The rate constants for the x gate were defined to be the same as in the Beeler-Reuter model where the gate is referenced as the $x1$ gate. This model introduces a new inactivation gate, X_i, which was given by

$$X_i = \begin{cases} 1.0 & \text{if } V_m \leq -100\mathrm{mV} \\ 2.837 \dfrac{\exp\left(0.04\left(V_m + 77\right)\right) - 1}{\left(V_m + 77\right) \exp\left(0.04\left(V_m + 35\right)\right)} & \text{otherwise} \end{cases} \tag{2.42}$$

The temporal trace of the time dependent potassium current along with the x gating variable is shown in Figure 2.20.

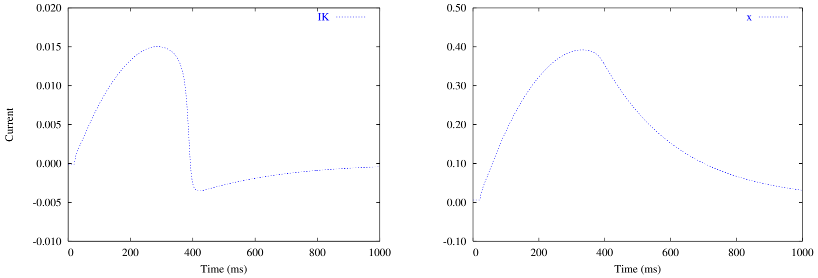

(a) (b)

Figure 2.20: Figure(a) shows the time dependent outward current over time and Figure(b) shows the x gate over time from the Luo-Rudy model.

Time independent potassium current

While present in the Beeler-Reuter model the time independent potassium current has been formulated differently along with the addition of two further potassium based time independent currents, I_{Kp} and I_b. This model uses one gating variable with a time constant small enough that it may be approximated by a steady state formulation.

$$I_{K1} = \overline{g_{K1}} \cdot K_{1\infty} \cdot (V_m - E_{K1}) \tag{2.43}$$

The reversal potential was the Nernst potential for potassium ions found from Equation (2.52). The maximum channel conductance was calculated by

$$\overline{g_{K1}} = g_{K1} \cdot \sqrt{[\mathrm{K}^+]_o / 5.4} \tag{2.44}$$

The steady gating parameter, $K_{1\infty}$ was calculated to be

$$K_{1\infty} = \frac{\alpha_{K1}}{\alpha_{K1} + \beta K1} \tag{2.45}$$

where the rate constants were given by

$$\alpha_{K1} = \frac{1.02}{1 + \exp\left[0.2385\left(V_m - E_{K1} - 59.215\right)\right]} \tag{2.46}$$

$$\beta_{K1} = \frac{0.49124 \exp\left[0.08032\left(V_m - E_{K1} + 5.476\right)\right] + \exp\left[0.06175\left(V_m - E_{K1} - 594.31\right)\right]}{1 + \exp\left[-0.5143\left(V_m - E_{K1} + 4.753\right)\right]} \tag{2.47}$$

A plot of the time independent potassium current is shown in Figure 2.21.

Plateau potassium current

The reversal potential for the plateau potassium current was the same as the reversal potential of the time independent potassium current.

$$E_{Kp} = E_{K1} \tag{2.48}$$

The ionic current was given by

$$I_{Kp} = \overline{g_{Kp}} \cdot K_p \cdot (V_m - E_{Kp}) \tag{2.49}$$

where

$$K_p = \frac{1}{1 + \exp\left(\left(7.488 - V_m\right)/5.98\right)} \tag{2.50}$$

A plot of the plateau potassium current is shown in Figure 2.21.

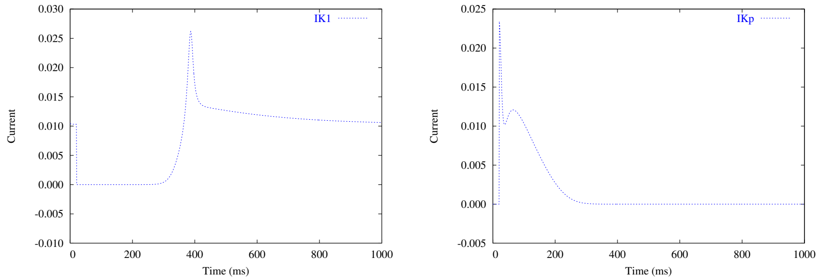

(a) (b)

FIGURE 2.21: Figure(a) shows the time independent outward current over time and Figure(b) shows the plateau current over timefrom the Luo-Rudy model.

Background current

The background current was given by

$$I_b = \overline{g_b} \cdot (V_m + 59.87) \tag{2.51}$$

and a plot of the background current over time is shown in Figure 2.22.

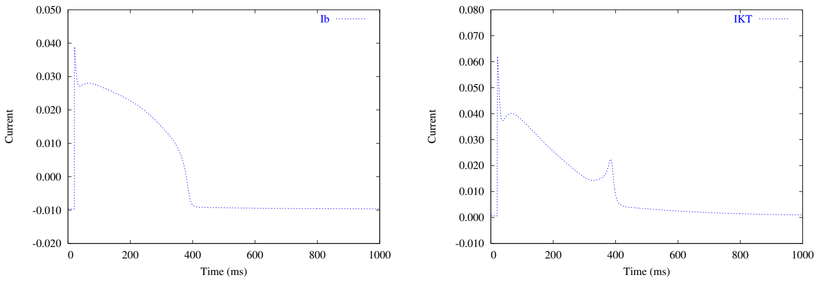

(a) (b)

FIGURE 2.22: Figure(a) shows the background current over time and Figure(b) shows the total time independent potassium current over time from the Luo-Rudy model.

Model parameters

The set of model parameters in consistent units used with the Luo-Rudy model are given in this section. The initial value of the transmembrane potential was set to be $-84.5\mathrm{mV}$. The initial values of the gating variables which were also time dependent are shown in Table 2.3. The other time dependent quantity is the intracellular calcium concentration. All of the other

Gate	*Initial value*
m	1.67×10^{-3}
h	9.38×10^{-1}
j	1.0
d	2.98×10^{-3}
f	1.0
x	6.02×10^{-3}

TABLE 2.3: Initial gate values for the Luo-Rudy I model

concentrations were constant over time. The intracellular and extracellular ion concentrations for the three ions included in the model are shown in Table 2.4. All concentrations are given in $\mathrm{nmol\ mm^{-3}} = \mathrm{mM}$. Where in the Beeler-Reuter model the reversal potentials of a given channel were directly set, in this model they were calculated from the ion concentrations. The

Ion	*Initial value*
$[\mathrm{Ca}^{2+}]_i$	1.78×10^{-4}
$[\mathrm{Ca}^{2+}]_o$	1.8
$[\mathrm{K}^{+}]_i$	1.45×10^{2}
$[\mathrm{K}^{+}]_o$	5.4
$[\mathrm{Na}^{+}]_i$	1.8×10^{1}
$[\mathrm{Na}^{+}]_o$	1.4×10^{2}

TABLE 2.4: Initial ion concentrations for the Luo-Rudy I model

reversal potential of a particular ion x was defined by its Nernst potential to be

$$E_x = \left(\frac{RT}{z_x F}\right) \ln \frac{[\mathrm{x}]_o}{[\mathrm{x}]_i} \tag{2.52}$$

where R is the gas constant, T is temperature, F is Faradays constant z_x is the valence of ion x and $[\mathrm{x}]_o$,$[\mathrm{x}]_i$ were the extracellular and intracellular concentrations of ion x respectively. The maximum conductance values used are shown in Table 2.5. All conductances are given in

Parameter	*Value*
$\overline{g_{Na}}$	2.3×10^{-1}
$\overline{g_{si}}$	9.0×10^{-4}
g_K	2.82×10^{-3}
g_{K1}	6.047×10^{-3}
$\overline{g_{Kp}}$	1.83×10^{-4}
$\overline{g_b}$	3.921×10^{-4}

TABLE 2.5: Conductance values for the Luo-Rudy I model

$\mathrm{mS\ mm^{-2}}$. It should be noted that the maximum conductances for g_K and g_{K1} are calculated elsewhere in the model using these values. The values for the other parameters used in the model are shown in Table 2.6. Here C_m is the membrane capacitance and A_m is the surface to volume ratio.

Parameter	*Value*	*Units*
C_m	1.0×10^{-2}	$\mu\mathrm{F\ mm^{-2}}$
A_m	1.0×10^{2}	$\mathrm{mm^{-1}}$
R	8.314472×10^{3}	$\mathrm{pJ\ nmol^{-1}\ K^{-1}}$
T	3.1×10^{2}	K
F	9.648534×10^{4}	$\mathrm{nC\ nmol^{-1}}$
PR_{NaK}	1.833×10^{-2}	$dimensionless$

TABLE 2.6: Parameter values for the Luo-Rudy I model

The Luo-Rudy II model

The second model published by Luo and Rudy (Luo & Rudy 1994) has become a widely used model in the field of cellular cardiac activation and while designed for mammalian ventricular cells was based mainly on the guinea pig. Again the units of the model parameters where adjusted to retain unit consistency. One of the main features of the model was the inclusion of more detailed calcium dynamics. The model used 15 ionic currents to generate action potentials.

$$\begin{aligned} I_{ion} =& I_{Na} + I_{Ca(L)} + I_K + I_{K1} + I_{Kp} + I_{NaCa} + I_{NaK} + I_{ns(Ca)} \\ &+ I_{p(Ca)} + I_{Ca,b} + I_{Na,b} + I_{rel} + I_{up} + I_{leak} + I_{tr} \end{aligned} \tag{2.53}$$

Initial ion concentrations

The initial intracellular and extracellular ion concentrations for the three ions included in the model are shown in Table 2.7. All concentrations are given in $\mathrm{nmol\ mm^{-3}} = \mathrm{mM}$. As is

Ion	*Initial value*
$[\mathrm{Ca}^{2+}]_i$	1.2×10^{-4}
$[\mathrm{Ca}^{2+}]_o$	1.8
$[\mathrm{K}^{+}]_i$	1.45×10^{2}
$[\mathrm{K}^{+}]_o$	5.4
$[\mathrm{Na}^{+}]_i$	1.0×10^{1}
$[\mathrm{Na}^{+}]_o$	1.4×10^{2}

TABLE 2.7: Initial ion concentrations for the Luo-Rudy II model

the case with the Luo-Rudy I model, the reversal potential of a particular ion x is defined by Equation (2.52).

Fast inward sodium current

The general form of the fast inward sodium current is the same as the original Luo-Rudy model.

$$I_{Na} = \overline{g_{Na}} m^3 hj\,(V_m - E_{Na}) \tag{2.54}$$

Here m is the activation gate, h is the inactivation gate and j is the slow inactivation gate. The time dependence of these gates was identical to the Beeler-Reuter model Equations (2.3)–(2.5). $\overline{g}_{Na}$ is the maximum sodium conductance which was set to be $1.6 \times 10^{-1}\mathrm{mS\ mm^{-2}}$ and E_{Na} is the reversal potential of the channel which was calculated from the sodium ion concentration using Equation (2.52). The α and β gating parameters were defined to be

$$\begin{aligned}
\alpha_m &= \frac{0.32(V_m + 47.13)}{1 - \exp(-0.1(V_m + 47.13))} \\
\beta_m &= 0.08\exp(-V_m/11) \\
\alpha_h &= \begin{cases} 0 & \text{if } V_m \geq -40\mathrm{mV} \\ 0.135\exp[(-80.0 - V_m)/6.8] & \text{if } V_m < -40\mathrm{mV} \end{cases} \\
\beta_h &= \begin{cases} \frac{1}{0.13(1+\exp[-(V_m+10.66)/11.1])} & \text{if } V_m \geq -40\mathrm{mV} \\ 3.56\exp(0.079V_m) + 3.1 \times 10^5\exp(0.35V_m) & \text{if } V_m < -40\mathrm{mV} \end{cases} \\
\alpha_j &= \begin{cases} 0 & \text{if } V_m \geq -40\mathrm{mV} \\ \frac{-1.2714\times10^5\exp(0.2444V_m)-3.474\times10^{-5}\exp(-0.04391V_m)}{1+\exp(0.311(V_m+79.23))}(V_m + 37.78) & \text{if } V_m < -40\mathrm{mV} \end{cases} \\
\beta_j &= \begin{cases} \frac{0.3\exp(-2.535\times10^{-7}V_m)}{(1+\exp(-0.1(V_m+32)))} & \text{if } V_m \geq -40\mathrm{mV} \\ \frac{0.1212\exp(-0.01052V_m)}{(1+\exp(-0.1378(V_m+40.14)))} & \text{if } V_m < -40\mathrm{mV} \end{cases}
\end{aligned} \tag{2.55}$$

L-type calcium currents

The current associated with the L-type calcium channel was divided into three separate currents for the three ions which pass through the channel.

$$I_{Ca(L)} = I_{Ca(L),Ca} + I_{Ca(L),Na} + I_{Ca(L),K} \tag{2.56}$$

where

$$I_{Ca(L),Ca} = df\,f_{Ca}\overline{I_{Ca(L),Ca}} \tag{2.57}$$

$$I_{Ca(L),Na} = df\,f_{Ca}\overline{I_{Ca(L),Na}} \tag{2.58}$$

$$I_{Ca(L),K} = df\,f_{Ca}\overline{I_{Ca(L),K}} \tag{2.59}$$

The activation gate, d and the inactivation gate, f are controlled by Hodgkin-Huxley type differential equations Equations (2.20) and (2.21) and a further inactivation gate, f_{Ca} is governed by the following equation.

$$f_{Ca} = \frac{1}{1 + \left(\frac{[\mathrm{Ca}^{2+}]_i}{K_{m,Ca}}\right)^2} \tag{2.60}$$

where $K_{m,Ca}$ is the half activation concentration for Ca^{2+} which was set to be $6.0 \times 10^{-4}\mathrm{mM}$. The rate constants for the d and f gates were defined to be

$$\alpha_d = d_\infty / \tau_d \tag{2.61}$$
$$\beta_d = (1 - d_\infty) / \tau_d \tag{2.62}$$
$$\alpha_f = f_\infty / \tau_f \tag{2.63}$$
$$\beta_f = (1 - f_\infty) / \tau_f \tag{2.64}$$

where

$$d_\infty = \frac{1}{1 + \exp\left(-\frac{V_m+10}{6.24}\right)} \tag{2.65}$$
$$\tau_d = d_\infty \frac{1 - \exp\left(-\frac{V_m+10}{6.24}\right)}{0.035\,(V_m + 10)} \tag{2.66}$$

and

$$f_\infty = \frac{1}{1 + \exp\left(\frac{V_m+35.06}{8.6}\right)} + \frac{0.6}{1 + \exp\left(\frac{50-V_m}{20}\right)} \tag{2.67}$$
$$\tau_f = \frac{1}{0.0197 \exp\left(-\left[0.0337\,(V_m + 10)\right]^2\right) + 0.02} \tag{2.68}$$

The three fully activated current terms, $\overline{I_{Ca(L),x}}$ were calculated from

$$\overline{I_{Ca(L),x}} = P_x z_x^2 \frac{V_m F^2}{RT} \frac{\gamma_{xi}[\mathrm{x}]_i \exp(z_x V_m F/RT) - \gamma_{xo}[\mathrm{x}]_o}{\exp(z_x V_m F/RT) - 1} \tag{2.69}$$

where the Ca^{2+}, Na^+ and K^+ ions are substituted for x where appropriate. P_x is the permeability of the membrane to ion x, z_x is the valence of ion x and γ_{xi},γ_{xo} are the intracellular and extracellular activity coefficients of ion x. Table 2.8 shows the coefficients which were used for each ion.

Quantity	*Value*
P_{Ca}	$5.4 \times 10^{-6}\mathrm{mm\ ms}^{-1}$
P_{Na}	$6.75 \times 10^{-9}\mathrm{mm\ ms}^{-1}$
P_K	$1.93 \times 10^{-9}\mathrm{mm\ ms}^{-1}$
γ_{Cai}	1.0
γ_{Nai}	7.5×10^{-1}
γ_{Ki}	7.5×10^{-1}
γ_{Cao}	3.41×10^{-1}
γ_{Nao}	7.5×10^{-1}
γ_{Ko}	7.5×10^{-1}

TABLE 2.8: L-type calcium channel constants

Time independent potassium current

This current features a single squared activation gate, X and a time independent inactivation gate X_i. The current is formulated to be

$$I_K = \overline{g}_K X_i X^2 (V_m - E_K) \tag{2.70}$$

where $\overline{g}_K$ was set to be

$$\overline{g}_K = 0.00282\sqrt{\frac{[\mathrm{K}^+]_o}{5.4}} \tag{2.71}$$

and the reversal potential, E_K was

$$E_K = \frac{RT}{F} \ln\left(\frac{[\mathrm{K}^+]_o + P_{NaK}[\mathrm{Na}^+]_o}{[\mathrm{K}^+]_i + P_{NaK}[\mathrm{Na}^+]_i}\right) \tag{2.72}$$

where P_{NaK} is the Na/K permeability ratio and was set to be $1.833 \times 10^{-2}(dimensionless)$. The gating variable X is governed by a standard Hogkin-Huxley differential equation.

$$\begin{aligned} \alpha_X &= \frac{7.19 \times 10^{-5}\,(V_m + 30)}{1 - \exp(-0.148\,(V_m + 30))} \\ \beta_X &= \frac{1.31 \times 10^{-4}\,(V_m + 30)}{-1 + \exp(0.0687\,(V_m + 30))} \end{aligned} \tag{2.73}$$

The time independent inactivation gate was calculated to be

$$X_i = \frac{1}{1 + \exp\left(\frac{V_m - 56.26}{32.1}\right)} \tag{2.74}$$

Time independent potassium current

This channel contains a single inactivation gate whose time constant is small enough that it may be approximated as steady state.

$$\overline{g}_{K1} = 0.0075\sqrt{\frac{[\mathrm{K}^+]_o}{5.4}} \tag{2.75}$$

2.6.4 The Noble 98 model

One of the features of this model is that it was designed with a mind to incorporating other processes such as mechanics,metabolism, pH dependence and drug receptor interactions. This model was also designed to be solved rapidly allowing it to be used in large scale tissue simulations. The model incorporates subspaces within the cell. These are the sarcoplasmic reticulum (SR) which was divided into two parts, the network SR (NSR) and the junctional SR (JSR), and a diadic space (DS) which lies between the JSR and the T-tubules of the cell. The ionic current term is made up of 27 individual currents.

$$\begin{aligned} I_{ion} =& I_{K1} + I_{to} + I_{Kr1} + I_{Kr2} + I_{Ks} + I_{K,Na} + I_{b,K} + I_{K,ATP} + I_{K,ACh} \\ &+ I_{Na} + I_{b,Na} + I_{p,Na} + I_{CaL,K} + I_{CaL,Na} + I_{CaL,Ca} + I_{Cal,KDS} + I_{CaL,NaDS} \\ &+ I_{CaL,CaDS} + I_{b,Ca} + I_{NaK} + I_{NaCa} + I_{NaCaDS} + I_{K,stretch} + I_{Na,stretch} \\ &+ I_{Ca,stretch} + I_{Ns,stretch} + I_{An,stretch} \end{aligned} \tag{2.76}$$

2.7 Simplified models of cardiac cells

Often it is not necessary to model the ionic currents of a cell with the accuracy and complexity inherent in the biophysically based models. With a view to investigating phenomena on a larger spatial and temporal scale several ionic current models have been developed which do not seek to model subcellular processes but only to provide an action potential with minimal computational cost. The simplest of these models is a polynomial model with just one variable.

2.7.1 The polyomial model

The most common polynomial model used to describe activation processes is a cubic polynomial model developed by Hunter, McNaughton & Noble (1975) as shown in Equation (2.77). Because there is only a single variable the model is very fast to compute so may be used on large geometries. The cubic model generates cellular depolarisation but it does not attempt to model repolarisation making it unsuitable for modelling any reentrant phenomena. It is possible to generate an analytic solution for the conduction velocity of the cubic model along a one dimensional fibre. The cubic ionic current model is defined to be

$$I_{ion} = g\left[V_m\left(1 - \frac{V_m}{V_{th}}\right)\left(1 - \frac{V_m}{V_p}\right)\right] \tag{2.77}$$

where all potentials are expressed as deviations from a resting potential V_r. V_m is the transmembrane potential, V_{th} is the threshold potential, V_p is the plateau potential and g is the membrane conductance. Typical values for these parameters are given in Table 2.9. The cubic model may

Parameter	*Units*	*Value*
V_r	mV	-85.0
V_{th}	mV	-75.0
V_p	mV	-15.0
g	mS mm^{-2}	0.004
C_m	μF mm^{-2}	0.01
A_m	mm^{-1}	200

TABLE 2.9: Typical parameters for the cubic ionic current model

be extended to a higher order polynomial ($5th$, $7th$ etc.) using the following formula to generate different depolarisation profiles

$$I_{ion} = g\left[V_m\left(1-\left(\frac{V_m}{V_{th}}\right)^n\right)\left(1-\left(\frac{V_m}{V_p}\right)^n\right)\right] \tag{2.78}$$

where n is a positive integer. The activation profile generated using the cubic ionic current model is shown in Figure 2.23. The polynomial models have roots at V_r, V_{th} and V_p causing

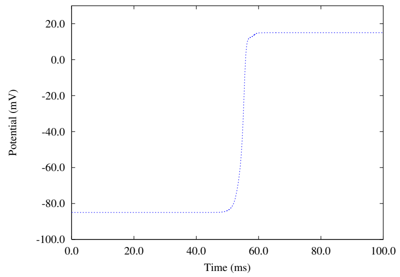

FIGURE 2.23: Potential trace from a single cell using the cubic ionic current model

any stimulus under V_{th} to return to rest and any suprathreshold stimulus to move to the plateau potential V_p.

2.7.2 The FitzHugh-Nagumo model

The FitzHugh-Nagumo model is based on the cubic excitation model but also includes a recovery variable so both depolarisation and repolarisation may be modelled. The form of the model used was adapted from Rogers & McCulloch (1994). The model normalises potential values to be between zero and one. The transmembrane potential has been denoted by u and is calculated as

$$u = \frac{V_m - V_r}{V_p - V_r} \tag{2.79}$$

where V_p is the plateau potential and V_r is the resting potential. The threshold potential, V_{th} was normalised in the same way. and the threshold potential in the same way.

$$\alpha = \frac{V_{th} - V_r}{V_p - V_r} \tag{2.80}$$

A cubic polynomial is used to describe the course of excitation

$$I_{ion} = c_1 u\,(u-\alpha)\,(u-1) + c_2\nu \tag{2.81}$$

where c_1 is an excitation rate constant and c_2 is an excitation decay constant. The α parameter represents the normalised threshold potential value. The variable ν is a dimensionless time dependent recovery variable and is calculated from the equation

$$\frac{d\nu}{dt} = b\,(u - d\nu) \tag{2.82}$$

where b is a recovery rate constant and d is a recovery decay constant. Both of these constants are dimensionless. The parameter values which were used in the FitzHugh-Nagumo model have been adapted to maintain unit consistency and are shown in Table 2.10. Traces of both the

Parameter	*Units*	*Value*
V_r	mV	-85
V_{th}	mV	-75
V_p	mV	15
c_1	μA mm^{-2}	0.175
c_2	μA mm^{-2}	0.03
b	ms^{-1}	0.011
d	$dimensionless$	0.55
C_m	μF mm^{-2}	0.01
A_m	mm^{-1}	200

TABLE 2.10: Typical parameters for the FitzHugh-Nagumo ionic current model

action potential and the recovery variable for the FitzHugh-Nagumo model over time are shown in Figure 2.24.

2.7.3 The modified FitzHugh-Nagumo model

In the same paper as the original model was described Rogers & McCulloch (1994) described some modifications to the model designed to generate a more realistic action potential increasing the velocity of the upstroke and removing the large hyperpolarization at the end of the action potential. The equation for the ionic current was changed by multiplying the c_2 term by the

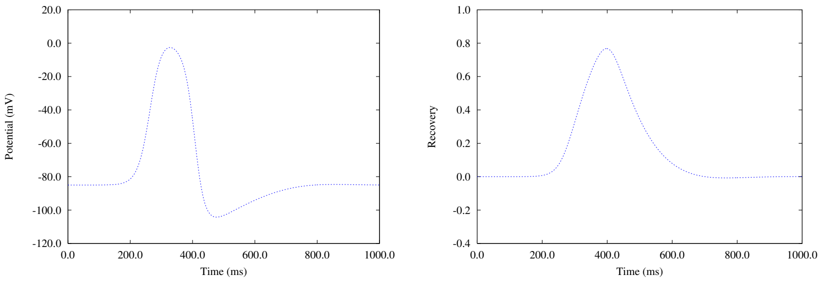

(a) Transmembrane potential

(b) Recovery variable

FIGURE 2.24: Traces from a single cell using the FitzHugh-Nagumo ionic current model. Figure(a) shows the generated action potential and Figure(b) shows the recovery variable.

normalised potential.

$$I_{ion} = c_1 u \left(u - \alpha\right)\left(u - 1\right) + c_2 u \nu \tag{2.83}$$

The parameters which were used in the model were also updated. Alterations are shown in Table 2.11. The resulting action potential and recovery variable traces are shown in Figure 2.25.

Parameter	*Units*	*Value*
c_1	μA mm^{-2}	0.26
c_2	μA mm^{-2}	0.1
b	ms^{-1}	0.013
d	$dimensionless$	0.8

TABLE 2.11: Adjusted parameters for the modified FitzHugh-Nagumo ionic current model

2.7.4 The van Capelle-Durrer model

The van Capelle-Durrer model (van Capelle & Durrer 1980) follows the same general form as the FitzHugh-Nagumo model with a single activation variable and a single recovery variable but has the ability to add more complexity to the representation of the parameters. The ionic current

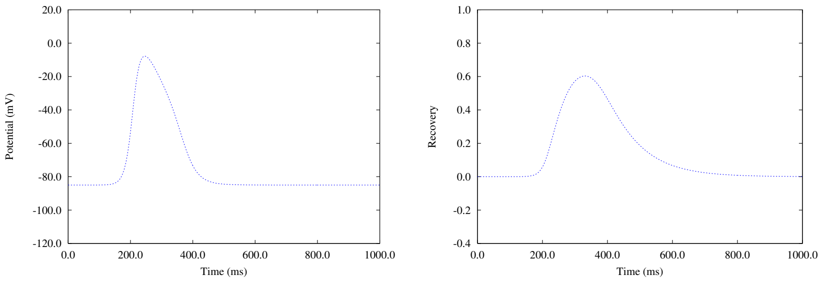

(a) Transmembrane potential

(b) Recovery variable

FIGURE 2.25: Traces from a single cell using the modified FitzHugh-Nagumo ionic current model. Figure(a) shows the generated action potential and Figure(b) shows the recovery variable.

from the van Capelle-Durrer model is defined to be

$$I_{ion} = -Y i_1\left(V_m\right) - \left(1 - Y\right) i_0\left(V_m\right) \tag{2.84}$$

where $i_0\left(V_m\right)$ and $i_1\left(V_m\right)$ are defined to be voltage dependent currents and Y is a dimensionless excitability parameter defined to be

$$\frac{dY}{dt} = \frac{1}{T}\left(Y_\infty\left(V_m\right) - Y\right) \tag{2.85}$$

The T parameter is a dimensionless time constant which may be used to easily scale the duration of the action potential and $Y_\infty\left(V_m\right)$ is a voltage dependent dimensionless variable which is the final value of the Y parameter. In this implementation of the model the $Y_\infty\left(V_m\right)$ was defined to be a piecewise function.

$$Y_\infty\left(V_m\right) = \begin{cases} 0 & \text{if } V_m < -80\text{mV} \\ 1 & \text{if } V_m > -60\text{mV} \\ \left(V_m + 80\right)/20 & \text{otherwise} \end{cases} \tag{2.86}$$

A piecewise function was also chosen to represent $i_1(V_m)$.

$$i_1(V_m) = \begin{cases} 0.05 + 0.005(V_m + 70) & \text{if } V_m < -70\text{mV} \\ 0.06 + 0.00425V_m & \text{if } V_m > 0\text{mV} \\ 0.05 + 0.01(V_m + 70)/70 & \text{otherwise} \end{cases} \tag{2.87}$$

The $i_0(V_m)$ was not represented directly, instead it was defined to be $i_0(V_m) = i_1(V_m) + f(V_m)$ where $f(V_m)$ was defined by a piecewise function.

$$f(V_m) = \begin{cases} 0.0784 + 0.02(V_m + 74.3) & \text{if } V_m < -74.3\text{mV} \\ -0.9884 + 0.0171(V_m + 27.8) & \text{if } V_m > -27.8\text{mV} \\ a_f V_m^3 + b_f V_m^2 + c_f V_m + d_f & \text{otherwise} \end{cases} \tag{2.88}$$

where

$$\begin{aligned} a_f &= 3.837854 \times 10^{-5} \\ b_f &= 5.84649 \times 10^{-3} \\ c_f &= 0.2531834 \\ d_f &= 2.356256 \end{aligned}$$

In this model $i_0(V_m)$, $i_1(V_m)$ and $f(V_m)$ have units of $\mu\text{A mm}^{-2}$. The parameters used in the model are given in Table 2.12.

Parameter	*Units*	*Value*
$V_m\,(initial)$	mV	-78.6
$Y\,(initial)$	$dimensionless$	0.07
T	ms	50
C_m	$\mu\text{F mm}^{-2}$	0.01
A_m	mm^{-1}	200

TABLE 2.12: Typical parameters for the van Capelle-Durrer ionic current model

Traces of both the action potential and the recovery variable Y are shown in Figure 2.26.

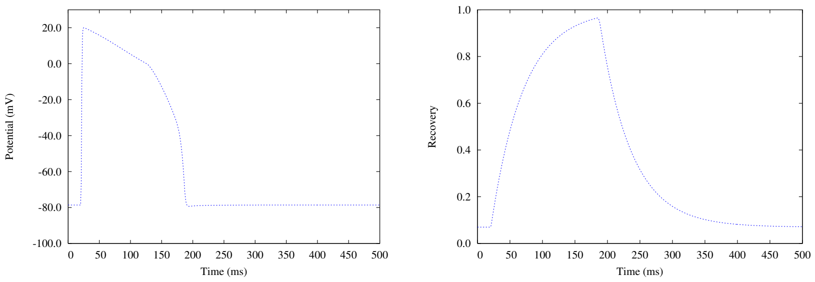

(a) Transmembrane potential

(b) Recovery variable

FIGURE 2.26: Traces from a single cell using the van Capelle-Durrer ionic current model. Figure(a) shows the generated action potential and Figure(b) shows the recovery variable.

2.8 The Bidomain Model

The complete model of cardiac activation would be one in which an accurate model is formulated for each type of muscle cell. The model would completely describe the structure of the cell and detail every aspect of its electrophysiological function down to a molecular level, as well as the mechanical and energetic processes involved if this information was required. This cellular model would then be inserted into an anatomically accurate description of the global cardiac geometry, and solved on a cell-by-cell basis over the cardiac volume. There are many reasons why such a model has not yet been constructed. Firstly, it is difficult to obtain an accurate model of cell function. Many of the membrane processes are still being quantified, if they are known at all. Secondly, an anatomically accurate definition of the cardiac geometry is still incomplete. Difficulties exist in measuring the position of the ventricular endocardium, and many models only describe the ventricular myocardium but not the atrial tissue or accessory structures. Coupled with this is a lack of a complete description of the cellular structure. The Auckland model is the most detailed and accurate ventricular microstructural model to date, yet it has little information on the Purkinje network, and none at all on the atrial tissues. The process of propagation is again only partially understood, and a model describing even the conductivities in the orthogonal microstructural directions is yet to be formulated. Similar models of the energetic function and the passive and active mechanics are still under construction, and the concept of being able to couple the various components together in a total model is only beginning to be looked at. Even given the availability of this vast amount of information, there would still be one requirement lacking. Existing computational resources are barely adequate to solve a small region of tissue. Spach & Heidlage (1993) have developed a model solving activation equations for individual cells for a two-dimensional sheet model containing between 25,000 and 85,000 cells. Even though there is only a small number of cells in a 2D preparation, and the ionic model used is not the most complex presently available, the model requires the use of a high-performance supercomputer in order to solve the problem. While computational speeds are doubling approximately every eighteen months, a complete model involving all cardiac processes is still a long way from being computationally tractable. Given that the current state of knowledge and the current computational capabilities preclude the use of a model completely representing the current state of knowledge of cardiac activation, we need to determine what level of detail is feasible yet sufficiently realistic so as to allow the investigation of various abnormal phenomena. The empirical models are no longer appropriate as they ignore the cellular processes. One commonly used method is to use a macroscopic model which uses a volume-averaged approach, known as the *bidomain model*. This model averages the electrical properties over some length scale which is greater than that of a single cell. In doing this with an appropriate choice of length scale, the effect of cell junctions on propagation can be ignored, and the discrete cellular structure may be replaced with a uniformly continuous structure. There are problems with this approach. If discrete cellular effects play a significant role in the propagation of activation, then either this will need to be incorporated or a new model will need to be constructed. Alternatively, if a macroscopic model can provide results which are a reasonable approximation to the explicit microscopic model then the averaged model may be justified.

2.8.1 Definition of the Bidomain Framework

The physical arrangement of cardiac cells has led to the belief that the heart has electrical properties that are the same as a syncytium. Experimental work by Weidmann (1970) and Clerc (1976) on mammalian cardiac tissue confirmed that propagation either along the fibre axis or transverse to it produced results like a one-dimensional cable. Cable theory defines propagation along a membrane between two distinct spaces. By extending standard one-dimensional cable theory to two or three dimensions gives rise to the bidomain model.

The concepts behind the bidomain model were first proposed by Schmitt (1969) who suggested that two interpenetrating domains could be used to describe cardiac tissue, one representing volume-averaged quantities in the intracellular space and one for those of the extracellular space.

A mathematical formulation of this proposal was constructed in several theses and papers by Tung (1978), Plonsey & Barr (1984), Miller & Geselowitz (1978) and others. The bidomain model has been adopted by many other researchers in one form or another due to its convenience and simplicity. The model is discussed more fully in review papers by Henriquez (1993) and Plonsey & Barr (1987).

Different papers give different names to the various regions that are part of the bidomain model. The names that we have chosen reflect the generally accepted definitions (as given by Krassowska & Neu (1994)) which tie in with those that physiologists would use to describe cellular structure. When developing an activation model which is designed to be coupled with other models, it is necessary to maintain consistent definitions and distinctly identify each region.

The bidomain framework defines two domains which make up the cellular matrix. The *intracellular domain*, given the subscript "i", is the region inside the cells, and the *extracellular domain* with subscript "e" is the region between cells. These two domains are interpenetrating which means that they coexist at all points in space. Therefore the properties and state of the tissue at each point have separate components related to each domain with appropriate subscripts. For example, a single point in space will have a tensor quantity associated with it defining the conductivity in each of the intracellular and extracellular spaces. The intracellular and extracellular domains are separated by the cell membrane at all points, and all current flow between the two domains occurs solely through the cell membrane. Because of the continuum approach to the physiology of the tissue, this transmembrane current is volume-averaged. This averaging approach is required so that a length scale can be chosen such that the averaging produces little loss of information. Additionally, a third domain may be defined consisting of all regions outside of the cardiac muscle, such as the bath that the tissue is in, or the tissues within the torso cavity. This domain is referred to as the *extramyocardial (outside) region* and given the subscript "o". Krassowska & Neu's (1994) paper simply refers to this region as "outside", but in a coupled problem it is unsure whether this should refer to a region outside the heart or outside the body. This naming convention is illustrated in Figure 2.27.

Some authors (including Pollard, Hooke & Henriquez (1993), Henriquez (1993), Plonsey & Barr (1987) and others), define the regions differently. In particular, what we term the extramyocardial region is defined as the extracellular space, and what we call the extracellular domain is called the *interstitial domain*, often with "extracellular" also written in parentheses afterwards. This causes some confusion in the definitions of what constitutes extracellular space, and is inconsistent with the standard physiological definition of the extracellular matrix being the con-

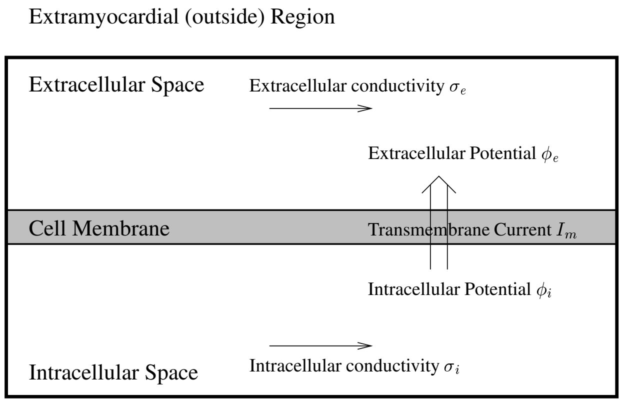

FIGURE 2.27: The bidomain model.

nective support structure and myoplasm surrounding cells. Therefore it seems best not to use the term "interstitial" at all, but to reserve the word "extracellular" for use in describing structure that is part of the extracellular matrix, and use another term for the medium surrounding the tissue, which in this case we have chosen to call "extramyocardial". This agrees also with the tissue definitions of Clerc (1976) in his study of tissue conductivities which is cited as a definition for these terms by Pollard et al. (1993). It is true that the extramyocardial space is also technically extracellular, but it is not (by definition) part of the cardiac tissue structure, and because it is often not used in many bidomain simulations, it is sensible to use another name for this region. Some authors(Plonsey & Barr 1987) also use the subscript "o" for the extracellular space, but this seems much less standard, and is similarly confusing.

The bidomain model describes current flow through the cell membrane in a space-averaged sense. Instead of modelling a discrete cellular structure, the bidomain constructs a continuum model with effective conductivity tensors which is governed by continuous partial differential equations.

2.8.2 Mathematical Derivation of the Bidomain Model

The most substantial mathematical description of the bidomain model is found in the review paper by Henriquez (1993), which presents a formal definition of the model from its origins in the core conductor model, and outlines many of the approximations that can be made under certain assumptions.

The bidomain equations may be derived in several ways depending on what variables are wanted to solve for. This derivation yields equations for the extracellular potential and the transmembrane potential while it is also possible to generate equations for the intracellular and extracellular potentials. The key definition in the bidomain equations is the definition of the potential difference across the cell membrane which is known as the transmembrane potential and given the symbol V_m.

$$V_m = \phi_i - \phi_e \tag{2.89}$$

Here ϕ_i is the potential in the intracellular domain and ϕ_e is the potential in the extracellular domain. A schematic diagram of a bidomain system is shown in Figure 2.27. Ohm's law was used to calculate the intracellular and extracellular current densities. It is assumed that the only current flow between the extracellular and extramyocardial space occurs through the boundary conditions imposed on the domains.

$$\begin{aligned} V &= JR \\ J &= \frac{1}{R}V \end{aligned} \tag{2.90}$$

Here V is a voltage, J is a current and R is a resistance. Voltages result from potential gradients so $V = \nabla\phi$ may be substituted. In addition to this the $\frac{1}{R}$ term may be written as a conductivity, σ which has units of mS. Equation (2.90) is then written for the two domains as

$$J_i = -\sigma_i \nabla\phi_i \tag{2.91}$$

$$J_e = -\sigma_e \nabla\phi_e \tag{2.92}$$

The negative signs in Equation (2.91) and Equation (2.92) are necessary to ensure that current flows are in the correct direction from regions of high potential to areas of low potential. Any current which leaves one domain must cross the cell membrane and flow into the other domain. This means that the change in current density in each of the domains must be equal in magnitude but opposite in sign. The change in current density in each domain is also equal to the current density across the membrane.

$$-\nabla \cdot J_i = \nabla \cdot J_e = A_m I_m \tag{2.93}$$

Here A_m is defined to be the surface to volume ratio of the cell membrane with units of mm^{-1} and I_m is the transmembrane current density per unit area which has units of $\mathrm{mS\ mm}^{-2}$. Combining Equation (2.91), Equation (2.92) and Equation (2.93), two equations were generated which represent the conservation of current densities.

$$\nabla \cdot (\sigma_i \nabla \phi_i) = A_m I_m \tag{2.94}$$
$$\nabla \cdot (\sigma_e \nabla \phi_e) = -A_m I_m \tag{2.95}$$

This implies that

$$\nabla \cdot (\sigma_i \nabla \phi_i) = -\nabla \cdot (\sigma_e \nabla \phi_e) \tag{2.96}$$

Subtracting $\nabla \cdot (\sigma_i \nabla \phi_e)$ from both sides yields

$$\nabla \cdot (\sigma_i \nabla \phi_i) - \nabla \cdot (\sigma_i \nabla \phi_e) = -\nabla \cdot (\sigma_e \nabla \phi_e) - \nabla \cdot (\sigma_i \nabla \phi_e) \tag{2.97}$$

Using Equation (2.89), Equation (2.97) can be rewritten as

$$\nabla \cdot (\sigma_i \nabla V_m) = -\nabla \cdot ((\sigma_i + \sigma_e) \nabla \phi_e) \tag{2.98}$$

This equation is usually refered to as the one of the two bidomain equations which is used to solve for the extracellular potential given a transmembrane potential distribution. The current flow across the membrane, I_m may be described by a time dependent capacitive current and an ionic current

$$I_m = C_m \frac{\partial V_m}{\partial t} + I_{ion} \tag{2.99}$$

where C_m is a membrane capacitance per unit area and I_{ion} is the sum of all ionic currents. The models used to represent the ionic current component are presented in Section 2.6 and Section 2.7. Combining Equation (2.94) and Equation (2.99) gives the following equation.

$$\nabla \cdot (\sigma_i \nabla \phi_i) = A_m \left(C_m \frac{\partial V_m}{\partial t} + I_{ion} \right) \tag{2.100}$$

To convert Equation (2.100) to have V_m as the dependent variable, $\nabla \cdot (\sigma_i \nabla \phi_e)$ is added and subtracted from the left hand side of the equation.

$$\nabla \cdot (\sigma_i \nabla \phi_i) - \nabla \cdot (\sigma_i \nabla \phi_e) + \nabla \cdot (\sigma_i \nabla \phi_e) = A_m \left(C_m \frac{\partial V_m}{\partial t} + I_{ion} \right) \tag{2.101}$$

Using Equation (2.89) Equation (2.101) may be expressed as

$$\nabla \cdot (\sigma_i \nabla V_m) + \nabla \cdot (\sigma_i \nabla \phi_e) = A_m \left(C_m \frac{\partial V_m}{\partial t} + I_{ion} \right) \tag{2.102}$$

which is known as the second of the bidomain equations and is used to update the transmembrane potential at each time. It is possible for an external stimulus current to be applied to either domain which gives the two bidomain equations as

$$\nabla \cdot ((\sigma_i + \sigma_e) \nabla \phi_e) = -\nabla \cdot (\sigma_i \nabla V_m) + I_{s1} \tag{2.103}$$
$$\nabla \cdot (\sigma_i \nabla V_m) + \nabla \cdot (\sigma_i \nabla \phi_e) = A_m \left(C_m \frac{\partial V_m}{\partial t} + I_{ion} \right) - I_{s2} \tag{2.104}$$

The extracellular domain is sometimes assumed to be highly conducting or the domains are assumed to be equally anisotropic in an effort to reduce the bidomain equations to a single domain hence reducing the amount of computational effort required to solve the problem. The reduced equation is known as the monodomain equation and is written as

$$\nabla \cdot (\sigma \nabla V_m) = A_m \left(C_m \frac{\partial V_m}{\partial t} + I_{ion} \right) - I_s \tag{2.105}$$

where the transmembrane potential is equal to the intracellular potential as the extracellular potential is effectively zero. The conductivity values in both the monodomain and bidomain equations are represented at each point in space by a tensor containing conductivities in the fibre, sheet and cross sheet directions allowing spatially varying fully orthotropic conductivities to be modelled.

Boundary conditions

There has been some differences in the literature in the boundary conditions which have been applied to the bidomain model Krassowska & Neu (1994). The boundary conditions used here are the original boundary conditions specified by Tung (1978) and confirmed by Krassowska &

Neu (1994). There is assumed to be no current flow between the intracellular and extramyocardial domains so the boundary condition applied to the boundaries on intracellular space may be written as

$$\sigma_i \nabla \phi_i \cdot \boldsymbol{n} = 0 \tag{2.106}$$

where n is a unit outward normal vector. The ϕ_i parameter was not explicitly represented in the formulation of the bidomain equations so the boudary condition was modified to become a boundary condition on V_m using Equation (2.89). Taking gradients, multiplying through by σ_i and then taking dot products with a normal vector, Equation (2.89) becomes

$$\sigma_i \nabla V_m \cdot \boldsymbol{n} = \sigma_i \nabla \phi_i \cdot \boldsymbol{n} - \sigma_i \nabla \phi_e \cdot \boldsymbol{n} \tag{2.107}$$

where Equation (2.106) demonstrates the ϕ_i term to be zero so the actual boundary condition on the transmembrane potential becomes

$$\sigma_i \nabla V_m \cdot \boldsymbol{n} = -\sigma_i \nabla \phi_e \cdot \boldsymbol{n} \tag{2.108}$$

The boundary conditions on the extracellular domain were set up as a current balance between the domain and the surrounding extramyocardial regions.

$$\sigma_e \nabla \phi_e \cdot \boldsymbol{n} = -\sigma_o \nabla \phi_o \cdot \boldsymbol{n} \tag{2.109}$$

The negative sign accounts for the direction of current flow where both sides of the equation use the same unit normal vector. The boundary extracellular potentials must also match the boundary extramyocardial potentials.

$$\phi_e = \phi_o \tag{2.110}$$

If the tissue is not surrounded by a medium combinations of flux and potential boundary conditions may be used to represent the desired setup. For a bidomain simulation with equal anisotropy ratios an analytic potential boundary condition Henriquez (1993) may be set which is equal to

$$\phi_e = -\frac{\sigma_{if}\sigma_{ef}}{\sigma_{if} + \sigma_{ef}} \tag{2.111}$$

where σ_{if} is the intracellular conductivity in the fibre direction and σ_{ef} is the extracellular conductivity in the fibre direction. The boundary condition which was applied to the monodomain

equation stated that there was no current flow out of the myocardial domain because no connection exists between the intracellular domain and any surrounding medium.

$$\sigma \nabla V_m \cdot \boldsymbol{n} = 0 \tag{2.112}$$

Chapter 3

Electrocardiography

3.1 Cardiac Anatomy and Function

The description of cardiac physiology given here is only a basic outline, with greater detail only on a few points which are relevant to the problem of activation modelling. For a more in-depth coverage of this subject, a textbook such as PHYSIOLOGY Section V: The Cardiovascular System (Berne & Levy 1988) should be consulted, or for a more specific look at only the heart, refer to PHYSIOLOGY OF THE HEART (Katz 1992).

3.1.1 Macroscopic description

The heart is situated near the centre of the chest cavity between the right and left lungs, and is supported inside a membranous structure, the pericardial sac. There are four major chambers in the heart and various accessory tissues as shown in Figure 3.1. The heart is divided into left and right halves by the interventricular septal wall, such that that there are no internal connections between the opposing chambers. The larger lower chambers are the *ventricles* (the left and right ventricles are abbreviated as "LV" and "RV" respectively) and the smaller upper chambers are the left and right *atria* (given abbreviations "LA" and "RA"). The bottom of the ventricles is called the *apex* and the top of the ventricles is known as the *base*.

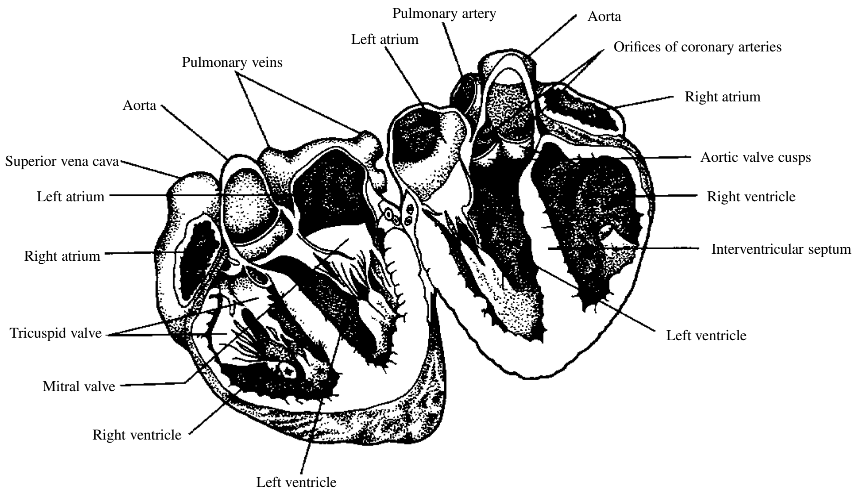

FIGURE 3.1: Longitudinal cross-section of the heart. From Katz (1992, Fig 1.1, p. 3).

Blood returns to the heart from the rest of the body via the superior and inferior vena cava and enters the right atrium. It flows from this chamber into the right ventricle which pumps the blood to the lungs via the pulmonary artery where the blood is oxygenated through the diffusion of oxygen across the alveolar membrane. The blood then returns to the heart through the pulmonary vein and enters the left atrium, passes into the left ventricle, and is subsequently pumped via the aorta to the rest of the body. For this reason the left ventricle is considerably larger than the right, and exhibits a greater change in pressure during the cardiac cycle. The period during which the heart is being filled with blood is called *diastole*, and the period of contraction during which blood is pumped from the heart into the lungs and circulatory system is called *systole*. The flow of blood from the RA to the RV is controlled by the tricuspid valve, and the mitral valve controls blood flow between the LA and LV. The pulmonary valve is at the outflow tract of the RV into the pulmonary artery, and the aortic valve at the connection of the aorta to the LV.

Papillary muscles in both the LV and RV tether the mitral and tricuspid valves to the ventricular wall during systole. The LV papillary muscles are large protrusions from the endocardial wall, and occupy a significant portion of the cavity, whereas the RV muscles are relatively small, and attached only by their bases to the ventricular wall. These muscles prevent the valves from inverting and entering the atria during systole, but the opening of the valves is solely due to the pressure difference between the chambers. The pulmonary and aortic valves are not tethered because they are only preventing blood flow during the slower passive filling phase.

3.1.2 Microscopic description

Cardiac muscle cells or *myocytes* are roughly cylindrical with a length in human ventricular tissue of 80 to $100\mu\mathrm{m}$ and a diameter of 10 to $20\mu\mathrm{m}$, and are bounded by the cell membrane or *sarcolemma*. A diagrammatic representation of the cell is given in Figure 3.2 and has been reconstructed from an electron micrograph.

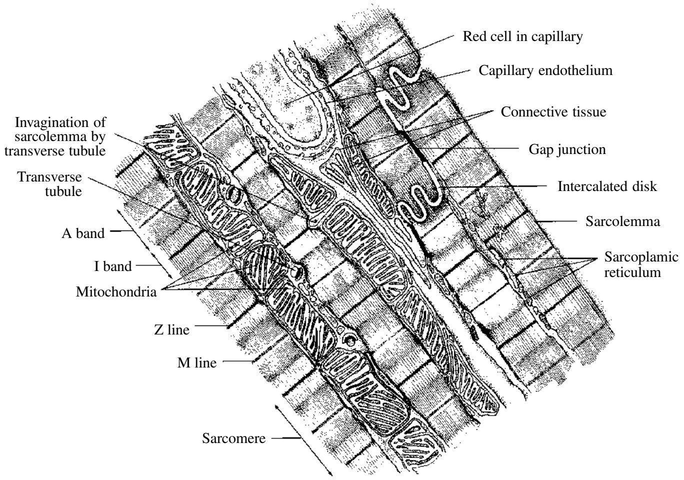

FIGURE 3.2: Diagram showing the structure of a cardiac muscle cell. A capillary runs between two adjacent cells. From Berne & Levy (1988, Fig 28–2, p. 432).

There are two sets of filaments present in muscle cells: *thin filaments* composed of a globular protein called *actin*, and *thick filaments* formed as an aggregate of a much larger protein called *myosin*. The thick and thin filaments interdigitate to form a *sarcomere* between the thin filament tethering points at Z lines, and this sarcomere is the basic contractile unit. The myosin molecule is composed of a pair of heavy chains which hinge outwards near the end of the chain and attached to the end of this "tail" are two globular "heads" and two pairs of light chains. The tail

and heads are hinged with respect to the rest of the molecule which is buried within the filament. According to the most common theory of contraction, these appendages, or *crossbridges*, cause the thick and thin filaments to move relative to each other according to the four-stage *crossbridge cycle*. An important compound involved in this process is ATP (adenosine triphosphate) which is usually bound to myosin to its resting state due to the very high affinity between them. ATP inhibits the interaction of myosin with actin. The first stage of contraction is the hydrolysis of ATP to form ADP (adenosine diphosphate) and $\mathrm{P_i}$ (inorganic phosphate), both of which remain associated with myosin. In this state, the myosin head interacts with the actin to form the active complex *actomyosin*. The chemical energy expended by dissociation of ADP and $\mathrm{P_i}$ from the complex performs mechanical work: the motion of the crossbridge. This allows ATP to bind again to the myosin and dissociates the crossbridge and the thin filament, returning to the resting state. Each cycle causes the thick and thin filaments to move by about 10 nm relative to each other.

A large number of sarcomeres are present in a single cell. Cells are joined end-to-end with other cells through intercalated disks and also branch and interconnect with neighbouring, nearly parallel cellular strands. Electrical connection between adjacent cells is through gap junctions which are located in the intercalated disks. Additionally, there are several important internal structures. Due to the almost constant energy requirements of repeated cellular contraction in the cardiac cell there are a large number of mitochondria which provide oxygen to the cell. A network of sarcoplasmic reticulum (SR) provides a large region of uptake pumps which remove Ca^{2+} from the cellular matrix and stores it in the junctional SR (JSR) awaiting release for enabling contraction. Deep invaginations of the sarcolemma into the fibre are known as the transverse tubular system or T-tubules. This system is used primarily to conduct the action potential down into the cell, and additionally to transport components from the interstitial fluid surrounding the cell deep into the cell, and is of particular importance in the excitation-contraction coupling.

An averaged myocyte direction can be defined at any point, which is known as the *local fibre orientation*. Early papers by MacCallum (1900) and Mall (1911) investigating the muscular architecture of the heart suggest that ventricular myocardium is an assembly of discrete muscle layers arranged in nested shells, or discrete fibre bundles(Le Grice 1992). This view of the microstructure was generally accepted until Hort (1957) and Streeter & Bassett (1966) performed the first quantitative measurements of fibre orientation and found a smooth transmural variation in fibre angle, which led to the predominant view being that myocardium is a *uniformly continuous, transversely isotropic* medium. A uniformly continuous medium is one in which there are no discontinuous changes in the local fibre orientation. A transversely isotropic medium is one in which the material structure is isotropic in all directions orthogonal to the fibre. In other words, the fibre orientation is the only local measure of microstructural composition, and can be regarded as a local axis of symmetry.

Later studies by Streeter, Spotnitz, Patel, Ross & Sonnenblick (1969) and others were more thorough and tended to confirm this view. Streeter (1979) did acknowledge, however, that the muscular architecture is discontinuous at both a macroscopic and microscopic level. There were some problems associated with the methods used to produce these results, as measurements were made only at a limited number of sites, and the measurement points could not be accurately located within a standard ventricular geometry.

Measurements of fibre orientation at a large number of sites spread throughout the ventricular myocardium were made by Nielsen (1987) and McLean & Prothero (1987). Their approaches involved cutting the ventricles into thick serial slices transverse to the base-apex axis. These techniques have problems, including difficulty in spatial registration between slices due to distortion, and loss of detail through averaging. McLean, Ross & Prothero (1989) measured fibre angles from both transverse and longitudinal slices, though the fibre orientation could not, of course, be measured from two orthogonal slices taken from the same heart.

Many of the problems associated with earlier studies have been overcome in the work of Le Grice (1992), which, building on the techniques developed by Nielsen (1987), is probably the most comprehensive and thorough quantitative study of cardiac microstructure to date. The approach used was to progressively remove thin layers of myocardium from a mounted intact myocardium, preserving spatial registration. This technique allows measurement of fibre orientation throughout the ventricular wall, and the absolute coordinates of each measurement point can be recorded for alignment with the measured geometry. This technique is a time-consuming process when performed manually. Details of this method and results are outlined more fully in a paper by Nielsen, Le Grice, Smaill & Hunter (1991).

Measurements obtained by Le Grice and coworkers are broadly consistent with those reported by Streeter and others, but also reveal a new understanding of the global nature of cardiac microstructure. Their studies suggest that the ventricular myocardium is not a uniform continuum, but rather a composite of discrete layers of fibres, which are called *sheets* (Le Grice 1992, Le Grice, Smaill, Chai, Edgar, Gavin & Hunter 1995, Smaill & Hunter 1991). Recorded fibre angles are the edges of these branching sheets, and because fibres traverse the sheets at a small

angle, these measured angles are only projections of the true angle. However, Streeter (1979) reports *imbrication angles*[1] at the epicardium (where the angles are greatest) of only $3°$ to $5°$, so this variation is often ignored.

The sheets are on average four cells thick, and branching occurs between layers, and the sheets are surrounded by a matrix of collagenous connective tissue. The nature and arrangement of the branching and of the connective structure varies according to position within the ventricular wall. Sheet orientation is generally radial to the ventricular surfaces, though they appear to become almost tangent to the epicardial surface. A simple structural model describing these features of the myocardium has been developed by the Cardiac Research Group at the University of Auckland[2], and details of the model are presented in several papers, (Hunter, Nielsen, Smaill, Le Grice & Hunter 1993, Hunter, Smaill, Nielsen & Le Grice 1996). Hunter et al. (1996, p.3) outline the model of ventricular myocardium, which

> ... is represented as an interconnected hierarchy of muscle layers whose three-dimensional orientation varies through the ventricular wall. The extent of coupling between adjacent layers or sheets also varies transmurally to accommodate the changes in sheet orientation. For a section cut tangential to the epicardial ventricular surface, the cut edges of the sheets define the fibre orientation. Alternately, the cleavage planes revealed in transmural base-apex sections indicate the radial orientation of the sheets.

Figure 3.3 shows a schematic view of the cardiac microstructure as predicted by this model. No similar studies have yet been made in which the nature of atrial tissue is investigated.

3.1.3 Connective tissue structure

There also exists a comprehensive organisation of extracellular connective tissue, including a substantial hierarchy of collagen structures which constrain the movement of the muscle fibres and sheets. This constraining network is more important when modelling mechanical behaviour than it is when modelling electrical activation. However, the constraints it places

[1]The imbrication angle (or sometimes *embrication angle*) at the epicardium is the angle at which the fibre intersects the epicardial surface. A value of $0°$ indicates a fibre orientation parallel to the surface.

[2]Department of Engineering Science, University of Auckland, New Zealand

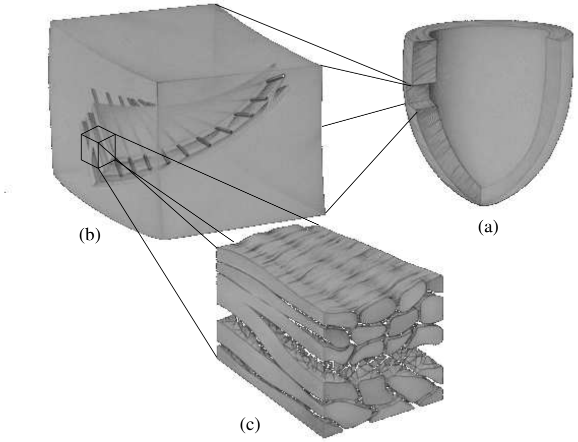

FIGURE 3.3: Schematic of cardiac microstructure. (a) Ventricular wall. (b) A transmural block showing fibre orientation and branching sheet structures. Note the transmural variation of fibre angle. (c) The muscle fibres are bound by collagen fibres into sheets 3 to 4 cells thick.

on the microstructure will become significant as the electro-mechanical coupling is investigated. Various studies have begun to quantify the nature of the connective tissues (Caulfield & Borg 1979, MacKenna 1994).

3.2 Activation

Mechanical contraction of the heart is caused by the electrical activation of the myocardial cells. The heart is electrically self-contained, having the ability to initiate its own beat with a regular period, and will continue to beat after being removed from the body. Cells capable of initiating electrical activity are called *pacemaker* cells, and exist in several places throughout the heart.

3.2.1 Normal Activation Sequence

The normal sequence of activation is shown diagrammatically in Figure 3.4. Only those pace-

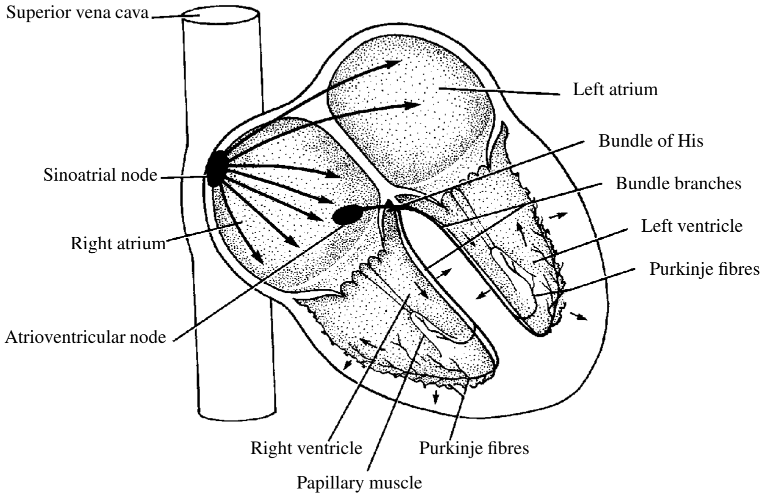

FIGURE 3.4: Schematic of the activation sequence. From Berne & Levy (1988, Fig 27–23, p. 414)

maker cells with the fastest rate of pacemaker discharge control the electrical activity of the entire heart. The region of tissue with the shortest period of spontaneous electrical activity is the *sinoatrial* (SA) node, which is located on the atrial wall near the junction of the superior vena cava and the right atrium, and consists of a group of pacemaker cells. Action potentials are normally generated here at the rate of 60 to 100 per minute. From the SA node, the action potential is propagated from cell to cell through firstly the right atrium, followed closely by the left atrium at a conduction velocity of approximately $1\ \mathrm{m\ s^{-1}}$ until it reaches the *atrioventricular* (AV) node. The AV node consists of similar pacemaker-type cells as are found in the SA node, but because they beat spontaneously at a slower rate (approximately 40 to 55 beats per minute) they are governed by the propagation from the SA node. In the event that the SA node is removed or destroyed, or that conduction is slowed through the atria, the cells in the AV node will take over as pacemaker for the heart.

Conduction through the AV node is at a much slower rate (around $0.05\ \mathrm{m\ s^{-1}}$) giving time for

NORMAL SEQUENCE OF ACTIVATION	CONDUCTION VELOCITY ($\mathrm{m \cdot sec^{-1}}$)	TIME FOR IMPULSE TO TRAVERSE STRUCTURE (sec)	RATE OF PACEMAKER CELL DISCHARGE ($\mathrm{min^{-1}}$)
SA node	< 0.01	$\top$	60–100
$\downarrow$		~ 0.15	
Atrial myocardium	1.0–1.2	$\perp$	None
$\downarrow$			
AV node	0.02–0.05	$\top$	Most rapid in
$\downarrow$		:	lower fibres:
Bundle of His	1.2–2.0	:	40–55
$\downarrow$		~ 0.08	
Bundle branches	$\top$	:	$\top$
$\downarrow$	2.0–4.0	:	25–40
Purkinje network	$\perp$	$\perp$	$\perp$
$\downarrow$			
Ventricular myocardium	0.3–1.0	~ 0.08	None

TABLE 3.1: Normal activation sequence. (From Katz (1992, Table 20.1, p. 475))

the atria to contract and pump blood into the ventricles before the action potential conducts through the ventricles and causes them to contract. The AV node is normally the only electrical connection between the atria and the ventricles. From the AV node, the electrical propagation enters the *bundle of His* which is the upper portion of the ventricular conduction system and runs down the right side of the septum, and this common bundle divides after a short distance into right and left *bundle branches*. The right branch continues down the right septal wall, and the left perforates the septum and splits into two further main branches on the left septal wall. All of these branches continue to subdivide into a complex network of fibres called the *Purkinje fibre network*, spreading across the endocardial surface of both ventricles and into the subendocardial region of the ventricular myocardium. Due to this arrangement of connecting fibres the septum is activated first and normally pushes in towards the left ventricular wall (Durrer, van Dam, Freud, Janse, Meijler & Arzbaecher 1970). The papillary muscles are also activated early so that they can prevent the AV valves from inverting during systole. Due to the faster conduction of approximately $2\ \mathrm{m\,s^{-1}}$ through the bundle and Purkinje fibres, the entire endocardium is excited almost simultaneously. The apical regions contract first and the basal regions are usually the last regions to be excited. Excitation spreads outwards through the ventricular wall at a rate of about 0.3 to $0.4\ \mathrm{m\,s^{-1}}$, and the first epicardial region to be excited is the thinnest portion of the right ventricular wall. This activation process is summarised in Table 3.1.

The pressure and volume changes of the cardiac cycle are illustrated in Figure 3.5. They fall into a number of phases: Isovolumetric contraction (the mitral valve closes and the pressure in the ventricle rises rapidly. Until the aortic valve opens, the volume of the ventricle remains unchanged). Ejection (as soon as the aortic valve opens, blood is rapidly ejected from the ventricle into the aorta. This is followed by a phase of relatively slow ejection). Isovolumetric relaxation (after ejection finishes, the aortic valve closes. As the ventricle relaxes, the pressure within it falls rapidly, but until it has fallen to the level present in the left atrium the volume in the ventricle remains unchanged). Ventricular filling (when the pressure in the ventricle falls below that in the atrium, the mitral valve opens and a period of rapid ventricular filline ensues. This is followed by a slow phase, or diastasis, during which the pressure rises slowly. This continues until artial contraction propel more blood through the mitral valave and causes a small increae in left ventricular volume and pressure prior to the onset of the next ventricular systole).

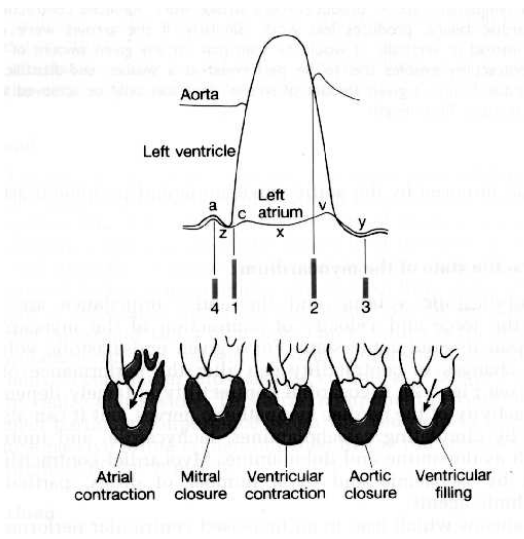

FIGURE 3.5: Pressure pulses in the left atrium, left ventricle and aorta

The relation between the pressure and the electrical impulse is shown in Figure 3.6.

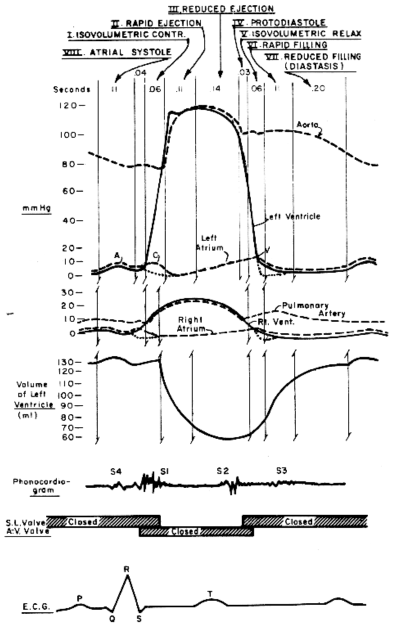

Fig. 3.120. Events of the cardiac cycle. *Upper*, Left heart; *lower*, right heart. Redrawn from Selkurt and Bullard.

FIGURE 3.6: Events of the cardiac cycle - pressure, volume and ECG

3.3 History of the ECG

The bioelectric sources which arise during the heart's excitation process produce a flow of electric current in the surrounding tissues. It is therefore possible to detect, with a pair of electrodes external to the heart, time-varying potential differences known as electrocardiograms.

The first recording of a human ECG was by Waller (1887). The electrical activity of the exposed heart was already known (and galvanometers had been invented) but Waller decided to investigate the possibility of recording potentials from the limbs of animals and from man. He dipped his right hand and left foot into a couple of basins of salt solution which were connected to two poles of an electrometer and "at once had the pleasure of seeing the mercury column pulsate with the pulsation of the heart".

Waller demonstrated this at St Mary's Laboratory in 1887 and Professor Willem Einthoven was in the audience (Waller often demonatrated the ECG on his dog Jimmie standing in buckets of salt solution). It is Einthoven[3] that most people credit with the birth of the ECG (Einthoven acknowledges Waller as the first person to use the word ECG) and Waller is overlooked.

Einthoven's major achievement was the invention of a device sensitive enough to record *potentials* from the body (as oppoesed to Waller who detected *voltages*). Einthoven's first ECG machine weighed approximately 600 poinds and required 5 operators.

Einthoven is responsible for developing the theory on which the ECG is based (e.g. Einthoven triangle, leads I, II, III, Einthoven equation). Einthoven's notation for the ECG wave is still used. A schematic ECG waveform is given in Figure 3.7. The letters P to U are used to denote certain parts of the waveform and, as we will see in more detail later, they can be attributed to different parts of the underlying cardiac activation.

An ECG is recording (1) the spread of stimulus throught the heart muscle (depolarisation) and (2) the return of the stimulated heart muscle to the resting state (repolarisation).

[3] Willem Einthoven was awarded the 1924 Nobel prize for Physiology or Medicine for the discovery of electrocardiogram mechanism

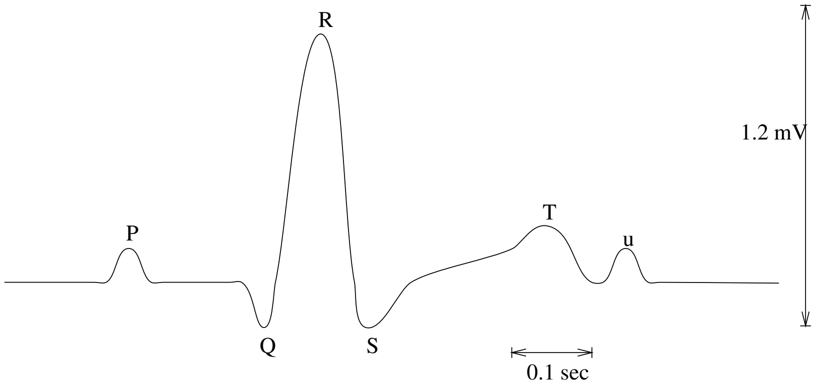

FIGURE 3.7: 'Standard' ECG (lead II waveform)

3.3.1 The Pathways of Conduction and the ECG

As noted above, in the usual sequence of events, the electrical impulse arises in the sinus node and spreads across the atria to reach the AV node. It can then only reach the ventricles by passing into the rapidly conducting AV bundle and its branches.

The first part of the ventricles to be activated is the septum, followed by the endocardium. Finally, the impulse spreads outwards to the epicardium.

The spread of the cardiac impulse gives rise to the main deflections of the ECG: P, QRS and T waves.

- the *P wave* is the first deflection of the cardiac cycle and represents atrial depolarisation;
- the *PR interval* represents the time taken for the cardiac impulse to spread over the atrium and through the AV node and His-Purkinje System;
- the *QRS complex* represents the spread of the depolarisation through the ventricles'
- the*T wave* represents the ventricular repolarisation.

There is still debate over the existence and interpretation of the U wave.

3.3.2 Electrodes and Leads

A conventional ECG consists of tracings from 12 leads. The term 'lead' refers to the ECG obtained as a result of recording the difference in potential between a pair of electrodes.

The bipolar (standard) leads

In these leads, the electrodes are attached to the limbs. In lead I the positive electrode is attached to the left arm and the negative to the right arm. In lead II the positive electrode is atttached to the left leg and the negative to the right arm. In lead III the positive is attached to the left leg and the negative to the left arm. They may thus be depicted as :

- lead I = left arm minus right arm (LA -RA)
- lead II = left leg minus right arm (LL-RA)
- lead III = left leg minus left arm (LL-LA).

i.e.

$$\begin{aligned} I &= E_L - E_R \\ II &= E_F - E_R \\ III &= E_F - E_L \end{aligned}$$

These leads were the original leads that were used by Eintoven in his early recordings. It can be deduced from these equations that lead II should be equal to the sums of lead I and III i.e.

$$I + III = II \qquad \text{(Einthoven's law)}$$

.

Einthoven regarded each limb used in the recording of the bipolar ECG as an apex of an equilateral triangle, equidistant electrically form the heart at the centreFigure 3.8. This idea is still used today in the interpretation of ECGs, despite its obvious limitations (e.g. the body is not an electrically homogenoeous sphere).

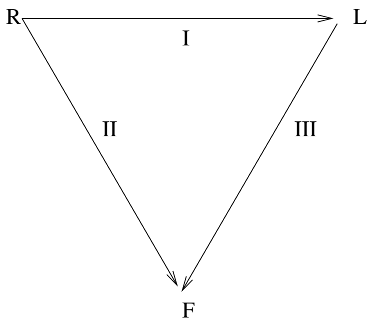

FIGURE 3.8: Orientation of leads I,II,II - Eintovens triangle

Unipolar leads

1934 saw the introduction of unipolar leads - so called because they represent the potential variation of a single point. In 1942 Goldberger modified these to produce the so called augmented unipolar lead (done so the voltages were easier to detect. The unipolar leads have an exploring electrode placed on a chosen site linked with an indifferent electrode with a very small potential. In an attempt to obtain a central terminal with ‘zero potential’, Wilson connected all three limb electrodes through 5000 Ω resistances to form the indifferent electrode.

Unipolar chest leads When unipolar leads are recorded from the chest wall, the exploring electrode is connected to the positive pole of the ECG and the negative to the central terminal. By convention, the following sites for the exploring electrode are normally selected (shown inFigure 3.9, Figure 3.10):

- V1, the fourth intercostal space just to the right of the sternum;
- V2, the fourth intercostal space just to the left of the sternum;

- V3, midway between V2 and V4;
- V4, the fifth intercostal space in th emidclavicular line;
- V5, the left anterior axillary line at the same horizontal level as V4;
- V6, the left mid-axillary line at the same horizontal level as V4

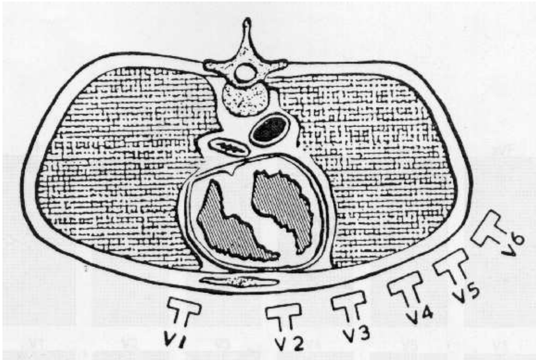

FIGURE 3.9: Diagram showing the orientation of the unipolar chest leads

Additional leads can be taken from V3R and V4R, sites on the right side of the chest equivalent to V3 and V4. Occasionally, leads may be placed at higher levels, e.g. the second, third or fourth intercostal spaces or further laterally (V7 and V8).

Unipolar limbleads In these leads, the exploring electrode is placed on one limb, and the negative pole is connected to Wilson’s central terminal, modified by the ommission of the connection from the limb under study to the central terminal Figure 3.11.

This modification “augments the voltage of the ECGs”, and the leads so derived are referred to as ’a’ leads. They are designated as follows:

- aVR, augmented voltage from the right arm;
- aVL, augmented voltage from the left arm;
- aVF, augmented voltage from the left foot.

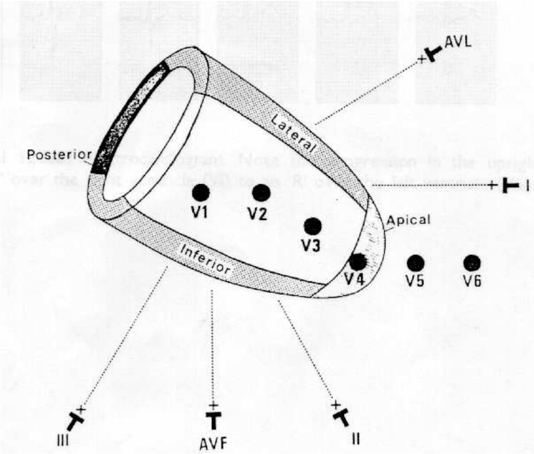

FIGURE 3.10: Diagram showing the orientation of the various leads to the left ventricular 'cone'. Note that there is no lead which is oriented directly to the posterior wall of the heart

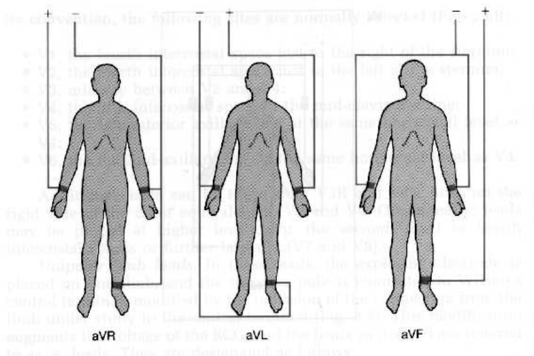

FIGURE 3.11: The attachment of unipolar limb leads. Note that the limb under study is not attached to the central (negative) terminal

If we consider each of these leads in a bit more detail then for aVR the central terminal consists of the average of the voltages from L and F and aVR is therefore

$$aVR = E_R - \frac{1}{2}(E_L + E_F) = -\frac{1}{2}(I + II)$$

If an average of the potentials from V, L and F is used as the central terminal (as in the original unipolar leads) then the voltage recorded, VR, is only $\frac{2}{3}aVR$ - hence the name "augmented" VR. Similarly

$$\begin{aligned} aVL = &\; E_L - \tfrac{1}{2}(E_F + E_R) &= I - \frac{1}{2}II \\ aVF = &\; E_F - \tfrac{1}{2}(E_L + E_R) &= I \mp \frac{1}{2}I \end{aligned}$$

It can be seen, that once any 2 of the 6 extremity leads (I, II, III, aVR, aVF, aVL) have been recorded the others can be deduced.

So the six extremity leads (I,I,II, aVR, aVL, aVF) show electrical voltage of the heart transmitted onto a vertical plane while the 6 precordial leads show voltages transmitted onto the horizontal plane.

3.4 Basic Theory

Einthoven's original model has proven extremely useful and still dominates much of electrocardiography. Einthoven used a dipole to represent the heart and postulated that the potentials at the limbs were related to the heart in the same way that the potential at the 3 vertices of an equilateral triangle places in an unbounded homogenous two dimensional volume conductor would be related to a dipole source at the centre of the triangle. That is the heart was modelled as a dipole and the body as part of a homogenous infinite conductor.

More detailed models have been developed (taking into account inhomogeneities, etc.) but the dipole model is still widely used (it is simple and reasonably accurate).

The ECG shows *projections* of this dipole in the direction of the leads. At position 1, projection onto lead II is small and negative (Q wave). As the "heart vector" sweeps through positions 2,3 and 4 the projection onto lead II is large and positive (the R complex). From 4 back to 0 the deflection becomes small and negative (see Figure 3.12).

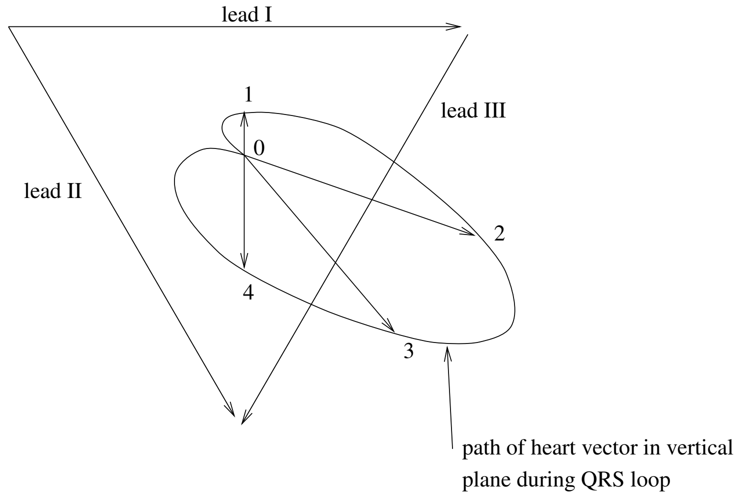

FIGURE 3.12: Heart vector projections

More complicated models (which used quadrupoles, solid angles, etc.) give rise to approximately the same thing.

The 12 different lead sites show the projection of the dipole along 12 different directions.

3.5 The Normal ECG

3.5.1 The Normal Electrocardiogram

A normal 12 lead ECG recording is given in Figure 3.13. We discuss below the significance of each part.

The P Wave

The normal P wave (Figure 3.14 A) results from the spread of electrical activity across the atria (the activity of the sinus node itself cannt be detected in the ECG). Because the impulse spreads from right to left, the P wave is upright in leads I,II and aVF, is inverted in aVR and may be upright, biphasic or inverted in lead III,aVL and V1. It should not be higher than 3mm in the bipolar leads or 2.5mm in the unipolar leads, or greater than 0.10 s in duration.

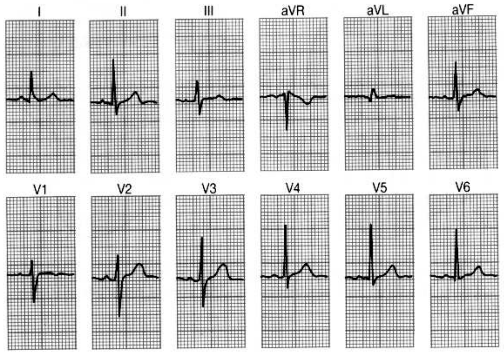

FIGURE 3.13: Normal 12-lead electrocardiogram. Note the progression in the upright deflection from 'r' over the right ventricle (V1) to an 'R' over the left ventricle V6.

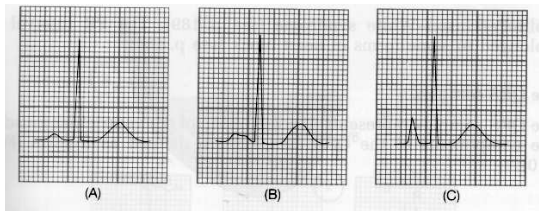

FIGURE 3.14: P wave appearance in lead II. (A) Normal. (B) Broadened and notched (P mitrale). (C) C Tall and peaked (P pulmonale).

When abnormal (Figure 3.14 B, C), the P wave may become:

- *inverted* (i.e. negative in the leads in which it is usually positive). This indicates depolarisation of the atria in an unusual direction, and that the pacemaker is not in the sinus node, but situated either elsewhere in the atrium, in the AV node or below this; or there is dextrocardia;

- *broadened and notched*, due to delayed depolarisation of the left atrium when this chamber is enlarged (P mitrale) (Figure 3.14 B). In V1, the P wave is then usually biphasic with a small positive wave preceding a deep and broad negative one;
- *tall and peaked*, exceeding 3mm, as a result of right atrial enlargement (P pulmonale) (Figure 3.14 C);
- *absent* or invisible due to the presence of junctional rhythm or sino-atrial block;
- replaced by flutter or fibrillation waves.

3.5.2 The PR Interval

This is measured from the beginning of the P wave to the beginning of the QRS complex (i.e. to the onset of the Q wave if there is one, and to the onset of the R wave if there is not). This interval corresponds to the time taken for the impulse to travel from the sinus node to the ventricular muscle. There is an iso-electric segment between the end of the P wave and the beginning of the QRS complex, whilst the impulse is passing through the AV node and specialised conducting tissue, as an insufficient amount of tissue is being electrically stimulated to produce a deflection detectable on the body surface.

The PR interval varies with age and with heart rate. The upper limit in children is 0.16, in adolescents 0.18 and in adults 0.20s, although it may be even longer in a few normal individuals. The faster the heart rate the shorter is the PR interval. It is regarded as abnormally short if it is less than 0.01s. A shortened PR interval is seen when the impulse originates in the junctional tissues and in the Wolff-Parkinson-White syndrome (see later). The PR interval is prolonged in some forms of heart block.

The QRS Complex

The QRS complex represents depolarisation of ventricular muscle. The components of the QRS complex are defined as follows (figure 3.15:

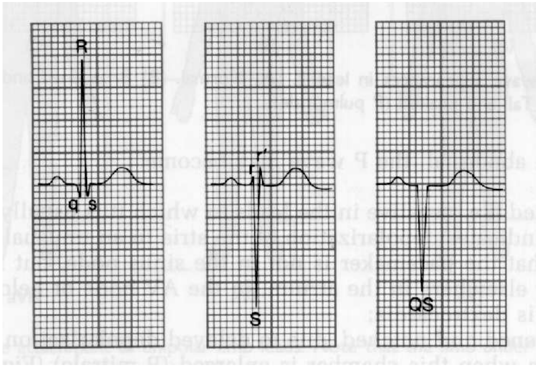

FIGURE 3.15: Variations in the QRS complex (see text)

- the R wave is any positive(upward) deflection of QRS complex. If there is more than one R wave, the second is denoted R'; and R wave of small voltage may be denoted r;
- a negative (downward) deflection preceding an R wave is termed Q;
- a negative (downward) deflection following an R wave is termed S
- if the ventricular complex is entirely negative (i.e. there is no R wave), the complex is termed QS.

The whole complex is often referred to as the QRS complex irrespective of whether one or two of its components are absent.

Ventricular depolarisation starts in the middle of the left side of the septum and spreads across to the right (phase 1 of ventricular depolarisation) (Figure 3.16). Subsequently, the main free walls of the ventricles are activated, the impulse spreading from within outwards and from below upwards. Because of the dominating bulk of the left ventricle, the direction of the vector of phase 2 is to the left and posteriorly. Finally, the base of both ventricular walls and the interventricular septum are depolarised. The appearances of the QRS in different leads can be largely explained by the major vectors of these phases as seen in Figure 3.16. In leads facing the left ventricular surface, there is a small Q wave due to septal depolarisation and a large R wave due to left ventricular depolarisation. On the right side of the heart, as seen by V1, there is usually an r wave due to septal depolarisation and a large S wave due to left ventricular forces directed away from the electrode.

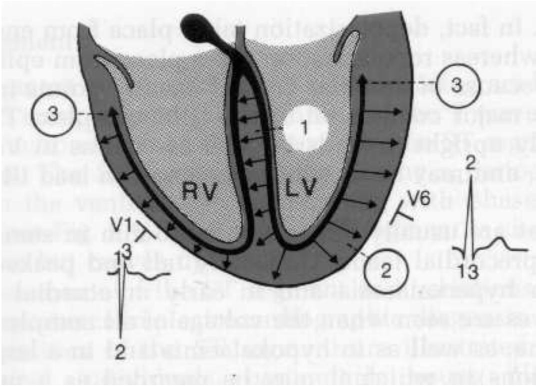

FIGURE 3.16: Genesis of QRS complex. Note that the first phase, directed from left to right across the septum, produces a Q wave in $V6$ and an R wave in V1. The second phase, due mainly to depolarisation of the left ventricle from endocardium to epicardium, results in a tall R wave in V6 and a deep S wave in V1. Finally, depolarisation of the basal parts of the ventricles may produce a terminal S wave in V6 and a terminal R wave in V1

Pathological Q waves As mentioned, small, narrow Q waves are normally to be found in leads facing the left ventricle, e.g. lead I, aVL, aVF, V5 and V6. These Q waves do not normally exceed 2mm in depth, or 0.03s in width. It should be noted that QS waves are normal in aVR, and are common in V1. Abnormally broad and deep Q waves are often a feature of myocardial infarction. Q waves in lead III are difficult to evaluate but can be ignored if there are no Q waves either in lead II or in aVF, or if they do not exceed 0.03s. Usually a 'normal' Q wave in lead III diminishes or disappears on deep inspiration because of an alteration in the position of the heart, whilst the 'pathological' Q wave of infarction persists.

The QRS complex should not exceed 0.10s duration, and usually is in the range 0.06-0.08s. Broad QRS complexes occur in bundle branch block, in ventricular hypertrophy and in ventricular ectopic beats.

The T Wave

The T wave is due to depolarisation of the ventricles. If repolarisation (the T wave) occurred in the same direction as depolarisation (the QRS complex) the T wave would be directed in an

opposite way to that of the QRS complex. In fact, depolarisation takes place from endocardium to epicardium, whereas repolarisation takes place from the epicardium to endocardium. Because of this, the T wave usually points in the same direction as the major component of the QRS complex. Thus, the T wave is normally upright in leads I and II as well as in V3 to V6, is inverted in aVR, and may be upright or inverted in lead III, aVL, aVF and V1 and V2.

The T waves are usually not taller than 5m in standard leads and 10mm in praecordial leads. Unusually tall and peaked T waves may be seen in hyperkalaemia and in early myocardial infarction. Flattened T waves are seen when the voltage of all complexes is low, as in myxoedema, as well as in hypokalaemia and in a large number of other conditions in which it may be regarded as a non-specific abnormality. Slight T wave inversion is also often non-specific , and may be due to such influences as hyperventilation, posture and smoking. The most important casuses of T wave inversion are:

- myocardial ischaemia and infarction;
- ventricular hypertrophy;
- bundle branch block.

The QT Interval

The QT interval represents the total time from the onset of ventricular depolarisation to the completion of repolarsation. It is measured from the beginning of the Q wave (or R wave if there is no Q wave) to the end of the T wave. Its duration varies with heart rate, becoming shorter as the heart rate increases. In general, the QT interval at heart rates between 60 and 90 per minute does not exceed in duration half the preceding PR interval. The measurement of the QT interval is often difficult as the end of the T wave cannot always be clearly identified, and the relationship between heart rate and duration of the QT interval is a complex one. Tables are available in textbooks of electrocardiography giving normal QT intervals. In practice, the main importace of a prolonged QT interval is that it is associated with a risk of ventricular tachycardias (particularly torsades de pointes), and sudden death. A long QT is sometimes an inherited abnormality but may result from such drugs as quinidine, procainamide, disopyramide, amiodarone and tricyclic antidepressants.

The ST Segment

The ST segment is that part of the electrocardiogram between the end of the QRS complex and beginning of the T wave. The point of junction between the S wave and the ST segment is known as the J point. The ST segment occurs during the period of unchanging polarity in the ventricles, corresponding with phase 2 of the action potential. The normal ST segment is situated on the iso-electric line but curves upwards.

Displacements of the ST segment and variations in its shape are of great importance in electrocardiographic diagnosis. ST segment elevation occurs because repolarisation of the injured tissue occurs more rapidly than that of normal tissue and a potential gradient exists.

ST elevation is caused by	- acute myocardial infarct (dead tissue with injured tissue surrounding it) - pericarditis (inflammation of the pericardium - ventricular hypertrophy (enlarged ventricle) - myocardial ischaemia (detected as ST depression) (deficiency of blood to part of the myocardium) can lead to myocardial infarcts - sinus tachycardia (fast heart beat, $>$100/ min, with its origin in the sinus node

3.5.3 The U Wave

The U wave is a broad, low-voltage wave present in most normal ECGs. Its cause is unknown; it may become unusually prominent in hypokalaemia and with digitalis therapy.

3.5.4 Some Abnormal ECGs

Names of clinical conditions:

- Left ventricular hypertrophy

- Right ventricular hypertrophy Figure 3.17
- Left bundle branch block Figure 3.18 (Purkinje fibres in the LV are interrupted Figure 3.19)
- Right bundle branch block Figure 3.20 (Purkinje fibres in the RV are interrupted Figure 3.21)
- WPW (Wolff-Parkinson-White syndrome)

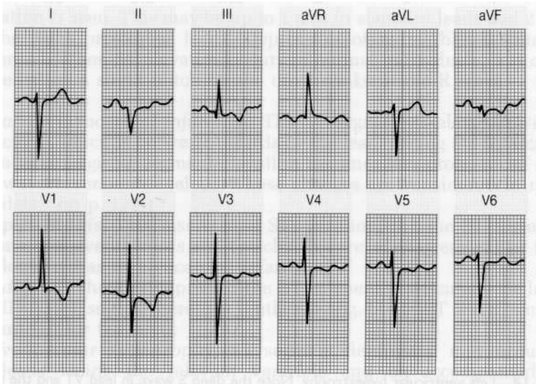

FIGURE 3.17: Right Ventricular Hypertrophy. Note the deep S wave in lead VI and the tall R waves in lead V5 and V6

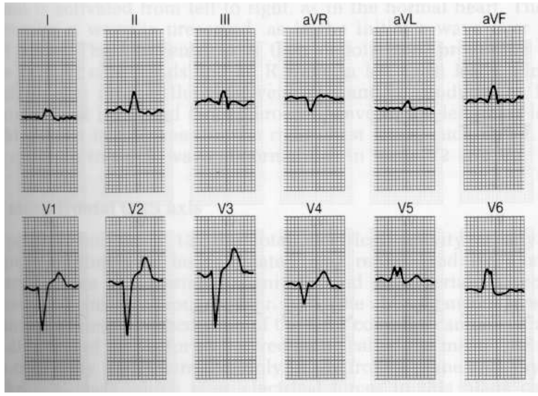

FIGURE 3.18: Left Bundle branch block ECG

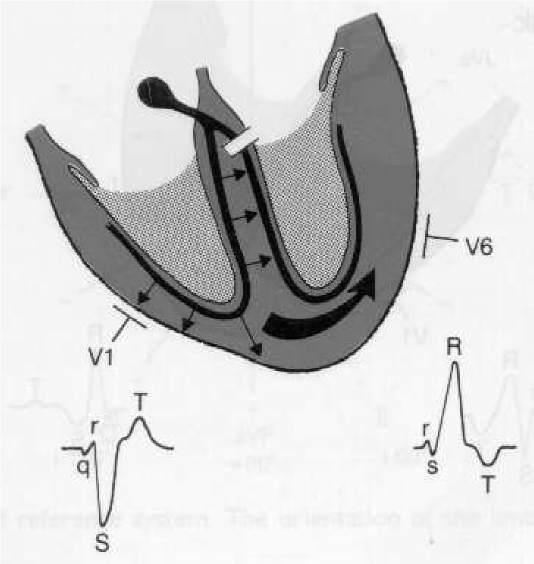

FIGURE 3.19: Left Bundle Branch Block. The inital vector is abnormal in being from right to left in the septum, thus producing an initial R wave in V6 and a Q wave in V1

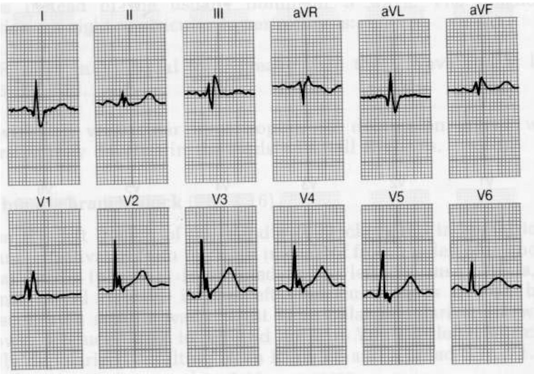

FIGURE 3.20: Right Bundle branch block ECG

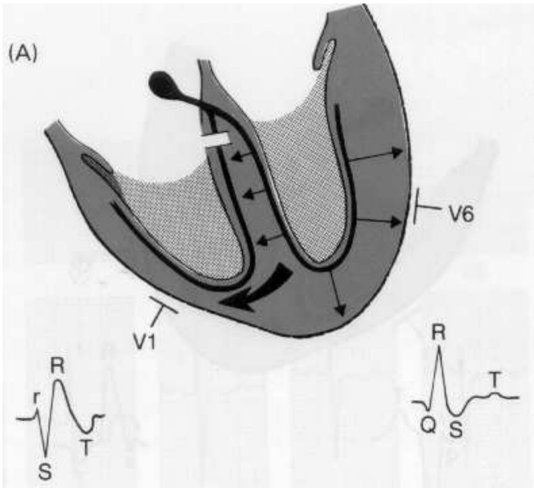

FIGURE 3.21: Right Bundle Branch Block. The septum is depolarised normally from left to right and hence a small Q is present in left ventricular leads and a small R in right ventricular leads. Left ventricular depolarisation causes an S wave in V1 and an R wave in V6. Late depolarisation of the right ventricle results in a prominent R' wave in V1 and broad S wave in V6

What can happen?

Ventricular Tachycardia (VT) - caused by slow conduction, or presence of an infarct. This can lead to Ventricular Fibrillation (VF) where there is no discernable pattern. Death quickly follows if this is not treated.

Treatment - external defibrillation
- internal defibrillator (implantable, onto heart, lasts about 4 years)

The strengths and limitations of the various treatments for ventricular tachyarrhythmias is given in Figure 3.22.

3.6 Usefulness of ECG

The ECG is used to determine what is happening to the heart (how it is performing, etc.). This is an "inverse" problem (inverse problems are very difficult to solve) - i.e. given this set of ECGs, what is the heart doing. (The 'forward' problem would be, given that the heart is doing this (i.e. has a given electrical activation pattern), what is the corresponding ECG - this would be far easier to solve).

The 'inverse' problem is solved largely by pattern recognition. There are books of ECGs which illustrate different problems - just find the right ECG (durations of different waves, heights, etc. give clues to possible irregularities).There is a standard set of steps to reading an ECG Figure 3.23.

In later sections we will consider the underlying mathematical theory behind the ECG. We now discuss a more generalised approach to ECG monitoring - namely body surface potential mapping.

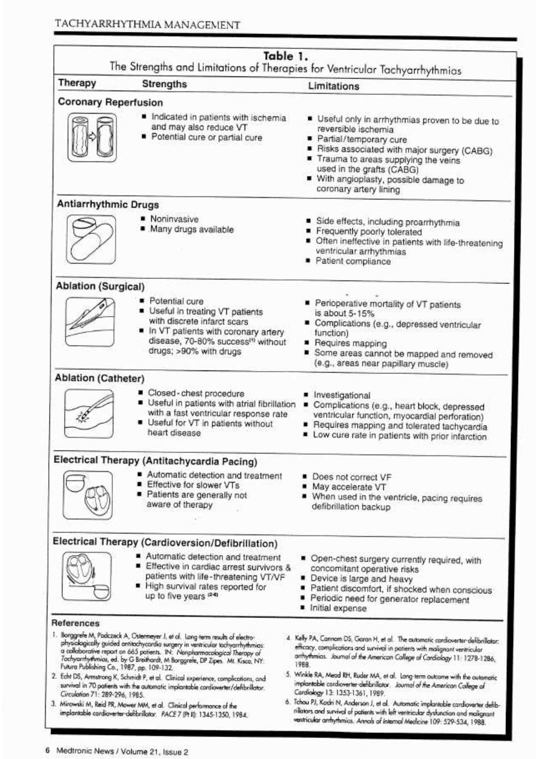

TACHYARRHYTHMIA MANAGEMENT

Table 1.
The Strengths and Limitations of Therapies for Ventricular Tachyarrhythmias

Therapy	Strengths	Limitations
Coronary Reperfusion	■ Indicated in patients with ischemia and may also reduce VT ■ Potential cure or partial cure	■ Useful only in arrhythmias proven to be due to reversible ischemia ■ Partial/temporary cure ■ Risks associated with major surgery (CABG) ■ Trauma to areas supplying the veins used in the grafts (CABG) ■ With angioplasty, possible damage to coronary artery lining
Antiarrhythmic Drugs	■ Noninvasive ■ Many drugs available	■ Side effects, including proarrhythmia ■ Frequently poorly tolerated ■ Often ineffective in patients with life-threatening ventricular arrhythmias ■ Patient compliance
Ablation (Surgical)	■ Potential cure ■ Useful in treating VT patients with discrete infarct scars ■ In VT patients with coronary artery disease, 70-80% success[1] without drugs; >90% with drugs	■ Perioperative mortality of VT patients is about 5-15% ■ Complications (e.g., depressed ventricular function) ■ Requires mapping ■ Some areas cannot be mapped and removed (e.g., areas near papillary muscle)
Ablation (Catheter)	■ Closed-chest procedure ■ Useful in patients with atrial fibrillation with a fast ventricular response rate ■ Useful for VT in patients without heart disease	■ Investigational ■ Complications (e.g., heart block, depressed ventricular function, myocardial perforation) ■ Requires mapping and tolerated tachycardia ■ Low cure rate in patients with prior infarction
Electrical Therapy (Antitachycardia Pacing)	■ Automatic detection and treatment ■ Effective for slower VTs ■ Patients are generally not aware of therapy	■ Does not correct VF ■ May accelerate VT ■ When used in the ventricle, pacing requires defibrillation backup
Electrical Therapy (Cardioversion/Defibrillation)	■ Automatic detection and treatment ■ Effective in cardiac arrest survivors & patients with life-threatening VT/VF ■ High survival rates reported for up to five years [2-6]	■ Open-chest surgery currently required, with concomitant operative risks ■ Device is large and heavy ■ Patient discomfort, if shocked when conscious ■ Periodic need for generator replacement ■ Initial expense

References

1. Borggrefe M, Podczeck A, Ostermeyer J, et al. Long-term results of electrophysiologically guided antitachycardia surgery in ventricular tachyarrhythmias: a collaborative report on 665 patients. IN: *Nonpharmacological Therapy of Tachyarrhythmias*, ed. by G Breithardt, M Borggrefe, DP Zipes. Mt. Kisco, NY: Futura Publishing Co., 1987, pp. 109-132.
2. Echt DS, Armstrong K, Schmidt P, et al. Clinical experience, complications, and survival in 70 patients with the automatic implantable cardioverter/defibrillator. *Circulation* 71: 289-296, 1985.
3. Mirowski M, Reid PR, Mower MM, et al. Clinical performance of the implantable cardioverter-defibrillator. *PACE* 7 (Pt II): 1345-1350, 1984.
4. Kelly PA, Cannom DS, Garan H, et al. The automatic cardioverter-defibrillator: efficacy, complications and survival in patients with malignant ventricular arrhythmias. *Journal of the American College of Cardiology* 11: 1278-1286, 1988.
5. Winkle RA, Mead RH, Ruder MA, et al. Long-term outcome with the automatic implantable cardioverter-defibrillator. *Journal of the American College of Cardiology* 13: 1353-1361, 1989.
6. Tchou PJ, Kadri N, Anderson J, et al. Automatic implantable cardioverter defibrillators and survival of patients with left ventricular dysfunction and malignant ventricular arrhythmias. *Annals of Internal Medicine* 109: 529-534, 1988.

6 Medtronic News / Volume 21, Issue 2

FIGURE 3.22: The strenths and weakenss associated with the various Ventricular Tachyarrhythmia management options

ECG interpretation.

ECG interpretation is largely a matter of experience and pattern interpretation. However, while building experience, it is useful to develop a method of 'systematic' ECG analysis. This is most easily performed by asking oneself a number of questions in a logical sequence about P, QRS and T waves in turn. A simple system is presented in Table 2.2.

Table 2.2 A system of ECG interpretation

Rate and rhythm
What is the rate (see p. 16)?
Is it regular or irregular?

P Wave
Are P waves present?
Is the P wave axis normal (p. 16)?
Is there evidence of left or right atrial enlargement (p. 19)?

PR interval (normal range 0.12–0.20 s)?
Is the PR interval normal?
Is each QRS complex preceded by a P wave?
Is there evidence of a slurred QRS upstroke (delta wave) (pp. 19, 189)?

QRS complex
Is the QRS duration within normal limits (0.08–0.11 s)
Is there evidence of bundle branch block (pp. 20, 26, 29)?
Is the QRS axis normal (p. 29)?
Are pathological Q waves present (p. 21)?
Is there a normal R wave progression across the chest leads (pp. 18, 20)?

ST segment and T wave
Is there abnormal ST elevation or depression (p. 23)?
Are the T waves upright (except aVR and V1)?

QT interval
Is the QT interval normal (in general less than 0.44 s)?

FIGURE 3.23: A procedure for interpreting ECGs

3.7 Body Surface Potential Mapping (BSPM)

ECGs do well, but do not provide the whole answer. e.g. they can tell WPW is present, but not where the accessory pathway is; they can (sometimes) detect infarcts and ischaemic regions, but not identify where these regions are. A famous example is the case of Sir Richard Hadlee Figure 3.24 who had open chest surgery to correct is WPW problem (which was identified with an ECG but could not be localised without more detailed mapping).

BSPM was brought about by the development of full chest lead systems to sample electrical activity at a relatively large number of sites. It began in the early 60s (?) and is not usually used clinically, however, those places that use it get good results. The problems with BSPM are that it can be more time consuming, there are no standard lead sets, it requires more setup time (there is a need to store and view a great deal of data), and an ECG provides a lot of information available on BSPM, suggesting that the extra work is not worth the effort.

Two examples of BSPM systems are given in Figure 3.25, Figure 3.26, Figure 3.27 and Figure 3.28. Figure 3.25 and Figure 3.26 are of the system used in Hobart, Australia and contain a large number of active (dry) electrodes that are embedded between 2 layers of neoprene. This suit can be applied quickly and a recording obtained in about the same time as that needed for a standard 12 lead ECG. The person standing in Figure 3.25 often uses this system in acute patients (in the ER room for instance) in preference to a 12 lead ECG. The other 2 figures, Figure 3.27 and Figure 3.28 are from a system in use in Salt Lake City, Utah. Strips of electrodes are placed over part of the torso at pre-specified locations. Each electrode is full with a conducting gel and contains a surround of adhesive, so they stick to the skin. This 32 lead system was obtain from looking at maps recorded with 120 leads and doing a statistical decomposition and evalue analysis. It was found that an ECG provides approximately 90% of the information available and 32 leads yield approximately 98%.

Schematics of other lead systems are given in Figure 3.29 and Figure 3.30. The first of these shows the location of the standard ECG leads in a uniform electrode array. The other figure shows 2 lead sets that have been proposed which are said to yield almost all the information of the uniform array.

Implantable defibrillators are being widely used instead of fixing the problem. There is a lack of good modelling and diagnostic cabability. However, it is our view that with good modelling

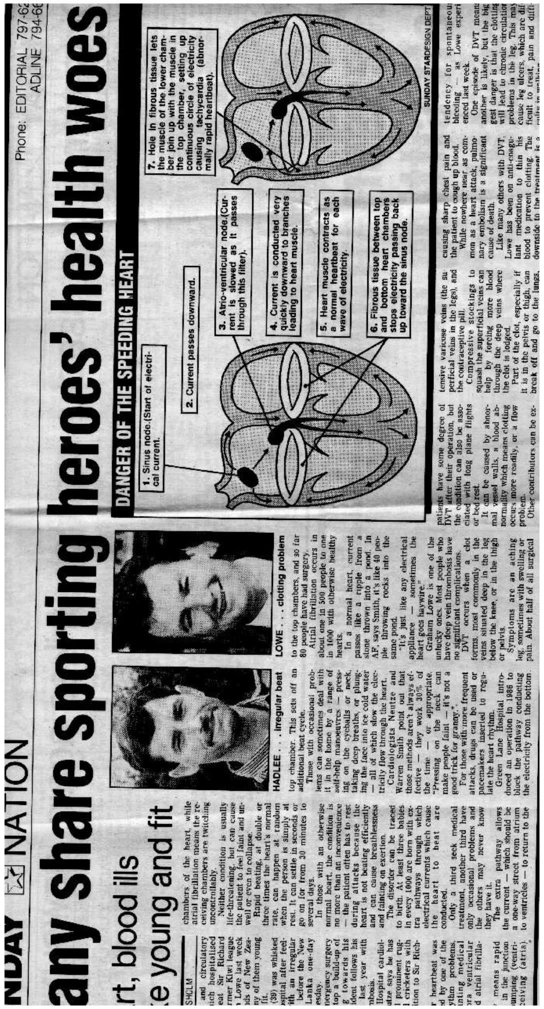

Phone: EDITORIAL 797-62
ADLINE 794-66

NDAY ☆ NATION

any share sporting heroes' health woes

rt, blood ills
e young and fit

DANGER OF THE SPEEDING HEART

1. Sinus node.(Start of electrical current.

2. Current passes downward.

3. Atrio-ventricular node(Current is slowed as it passes through this filter).

4. Current is conducted very quickly downward to branches leading to heart muscle.

5. Heart muscle contracts as a normal heartbeat for each wave of electricity.

6. Fibrous tissue between top and bottom heart chambers stops electricity passing back up toward the sinus node.

7. Hole in fibrous tissue lets the muscle of the lower chamber join up with the muscle in the top chamber, setting up continuous circle of electricity causing tachycardia (abnormally rapid heartbeat).

SUNDAY STAR/DESIGN DEPT

HADLEE . . . irregular beat

LOWE . . . clotting problem

FIGURE 3.24: The newspaper article mentioning Sir Richard Hadlee's WPW problem

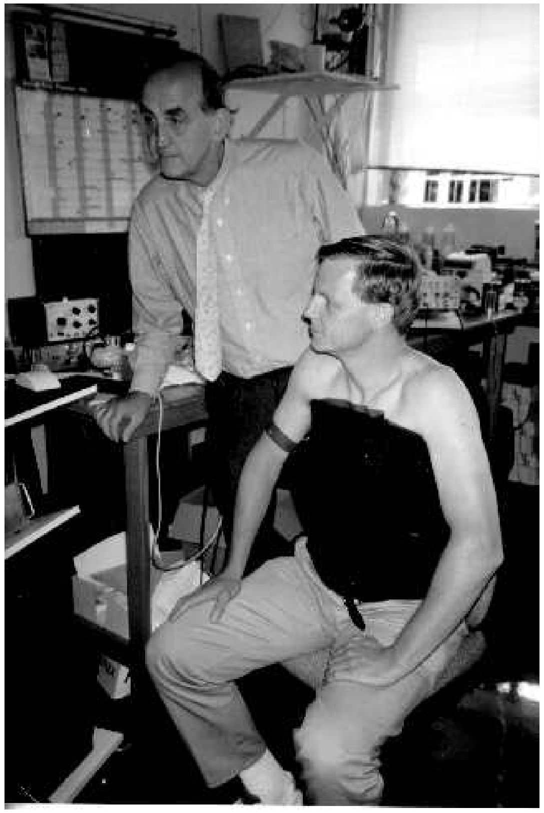

FIGURE 3.25: Hobart Body surface mapping system

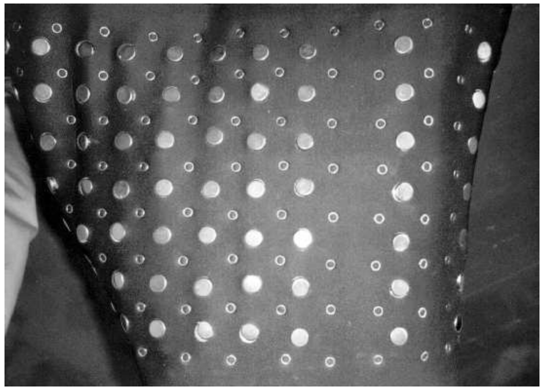

FIGURE 3.26: Hobart Body surface suit

FIGURE 3.27: Utah body surface mapping suit

FIGURE 3.28: Utah body surface mapping suit- another view

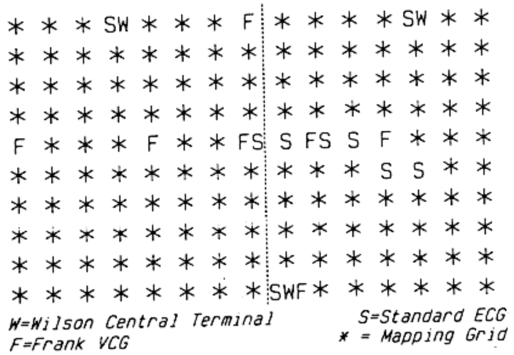

FIGURE 3.29: Comparison of torso electrode locations for vectorcardiography (F), for standard electrocardiography (S) and for body surface potential mapping. The vertical lines marks the sternum.

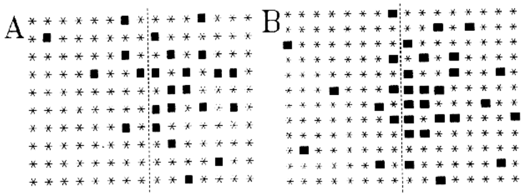

FIGURE 3.30: Utah body surface mapping suit- another view. Electrocardiographics lead sets proposed by Barr (A- Duke) and Lux (B- Salt Lake City)

and new imaging techniques, and the cooperation of clinical staff, a great deal of progress can be made. We currently have our own BSPM system.

3.7.1 BSPM at Halifax, Canada

We present in this section real BSPM maps recorded from patients suffering from WPW in Dalhousie University, Halifax, Canada. The emphasis on this system is due to the availability of the measured maps. As mentioned above, WPW is a condition in which an accesory pathway exists between the atria and ventricles. Although this does not affect a large proportion of the population it is a situation in which BSPM has been very successful since the site of the accessory pathway can, in most cases, be determined before inserting a catheter for ablation (5-10 years ago open heart surgery was required). It is relatively easy to fix (just cut/ablate the tissue involved) once the region has been localised. It is also fairly easy to detect on an ECG Figure 3.31, Figure 3.32 but it cannot be localised using a standard ECG.

Cause	-	breakdown of "insulation" between atria and ventricles. Ventricles are being stimulated from above and below - loss of pumping efficiency.
Cure	-	find accessory pathway and ablate (i.e. burn part of the tissue with a catheter - this is inserted in the leg).

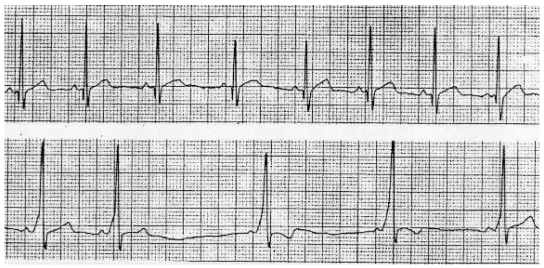

FIGURE 3.31: Part of an ECG of a WPW condition. At slower rates (bottom) a delta wave is more prominent that it is at higher rates

Figure Figure 3.33 illustrates the electrode locations used in the Halifax system (black dots - left hand side is the front). Recordings from a healthy male are given in Figure 3.34 (front) and Figure 3.35 (back). Note that some of the leads given no recording, so are discard in the final analysis. The position of the standard V1 and V2 leads are marked. The recordings given are

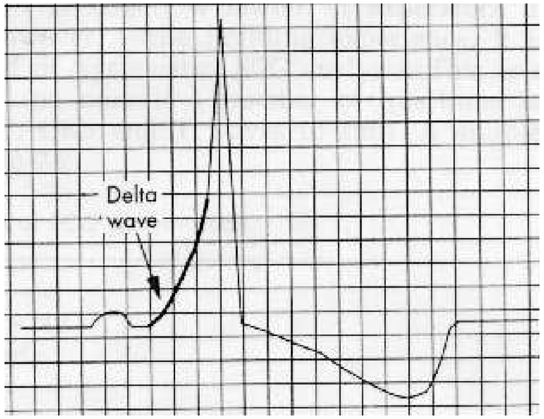

FIGURE 3.32: Scehmatic representation of ECG features of the WPW patten.

based on averages of 10 seconds of recordings.

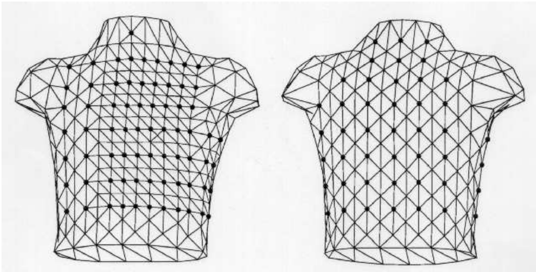

FIGURE 3.33: The location of the electrodes used in the BSPM system at Halifax. The left hand side represents the front, and electrodes are denoted using black dots

Fiducial markers (start and end of QRS etc) are then obtained by looking at the Frank VectorCardiograph leads Figure 3.36 (i.e. looking at the difference in potential across the body, front-back of the body and up/down on the body).

After the fiducial markers have been identified, the data is interpolated to present the body surface potential maps seen in Figure 3.37 to Figure 3.39. These figures are maps of the contours of potential at 10 ms intervals. The first maps are simply just noise (since these are before activation) and the times corresponding to the fiducial markers (RON and ROFF) are identified. RPK corresonds to the peak of the QRS. The location of the extrema are also plotted and negative

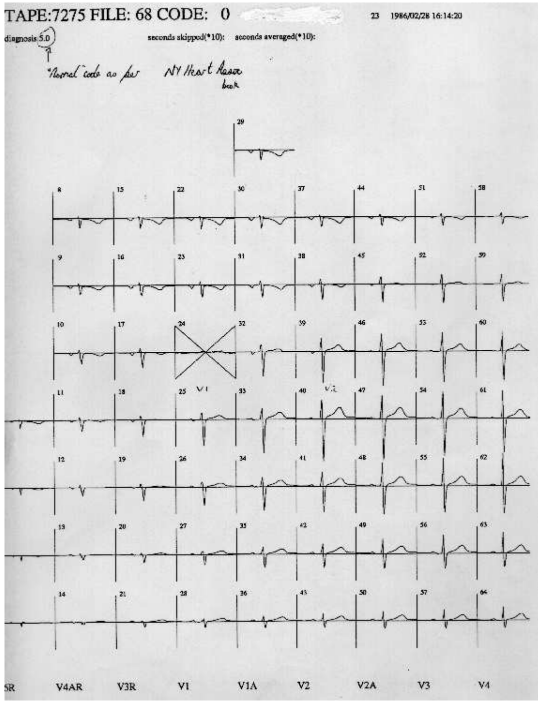

FIGURE 3.34: The front recordings from a normal male using the Halifax BSPM system (10 seconds of recordings that have been averaged. Note that some leads give no recording and are therefore discarded from further analysis. The location of the leads V1 and V2 have been marked. The left hand code is the code as per the NY Heart Association handbook

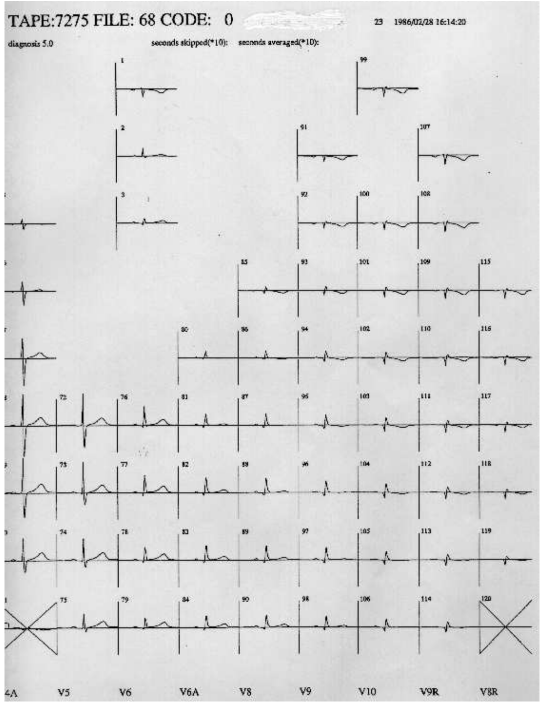

FIGURE 3.35: The back recordings from a normal male using the Halifax BSPM system

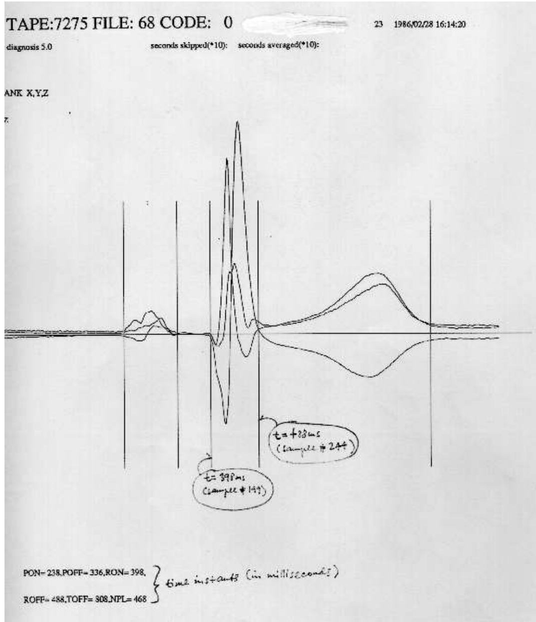

FIGURE 3.36: The VCG used to determine the Fiducial markers. PON is the start of the P wave (in ms) POFF the end of the P wave, RON and ROFF the equivalent times for the R wave and TOFF is end of the T wave.

potentials are given in dashed contour lines.

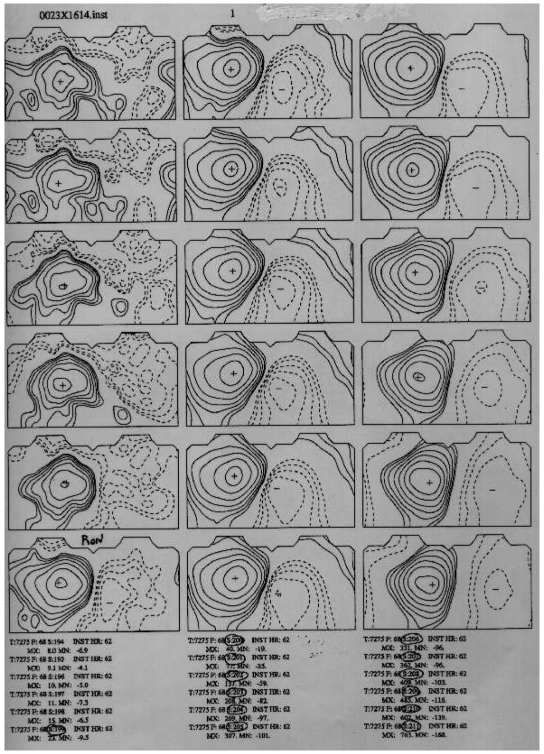

FIGURE 3.37: Isopotential lines for a normal patient at 10 ms intervals. The first maps are simply just noise since these are before activation and the times corresponding to the fiducial markers RON and ROFF are identified. RPK corresonds to the peak of the QRS. The location of the extrema are also plotted and negative potentials are given in dashed contour lines.

Things to look for

-positions of maximum and minimum and how these move (and locations of “zero” line).

-before RONN - noise
-early R - septal activation

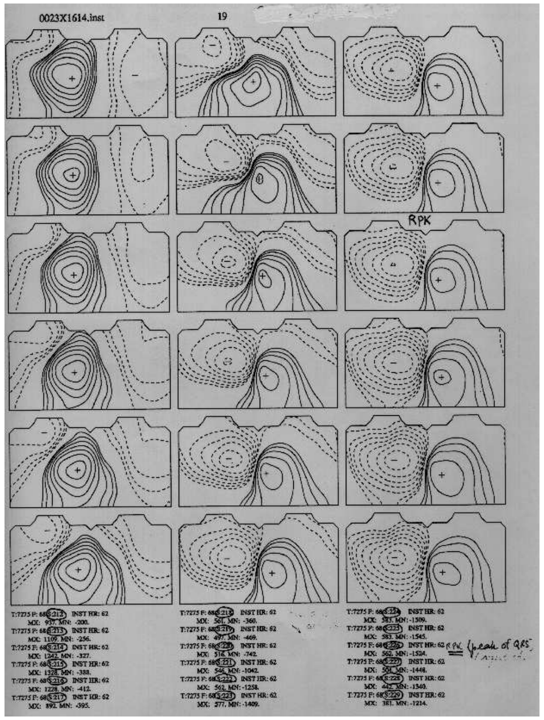

FIGURE 3.38: Normal BSPM maps (b)

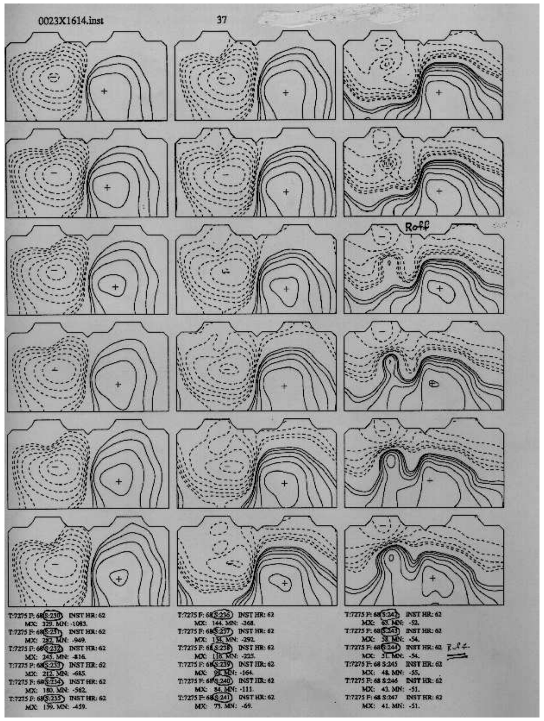

FIGURE 3.39: Normal BSPM maps (c)

As activation reaches the apex, the negative region moves over the right shoulder.

As activation moves up ("deflection" pointing outward?) there is widespread left ventricular and right ventricular epicardial breakthrough. The pattern can become complicated and variable. Usually the maximum moves slowly around the back Figure 3.40.

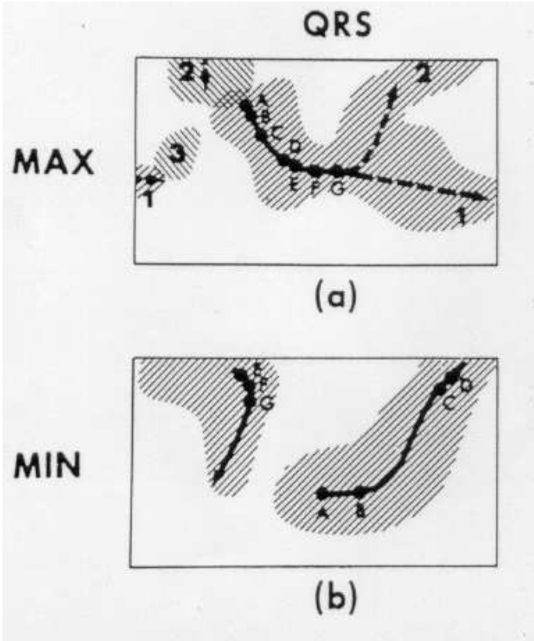

FIGURE 3.40: Trajectory maps depicting postion of the maxima (top) and minima (bottom) during the QRS copmlex. The left half of each map represents the front of the torso. Selected instants, labelled A through G, are shown. During the end of the QRS complex, three variations (1, 2, and 3) are observed

3.7.2 Abnormal Maps

To help in the interpretion of BSPM from WPW patients, Dalhousie University has a model of a human heart (anatomically accurate) in a model of a torso. It had a rule-based activation process (cellular-automata, cells 1mm^3), and each cell had a set of rules about when it will become activated and for how long. This determines epicardial potentials and then a BEM torso model was used to solve for torso potentials (homogenous torso).

They ran a number of simulations for a number of pre-excitation slices (Figure 3.41) and calculated the body surface potentials for each preexcitation (most prominent differences). The results of each of these simulations are shown in Figure 3.42. The locations of the extrema and respective regions of positivity and negativity are used to distinguish each map. These templates are used to help localise the accesory pathway. A patient suffering from WPW (diagnosed from a standard ECG) will have a body surface map taken. This is then compared to the templates and the accessory pathway site estimated. The patient will then undergo catheter surgery to localise the site (starting at the estimated site). In almost all cases, the estimated site corresponds to the site that is ablated. Examples of real maps, and the actual ablation site are given in Figure 3.43 to Figure 3.48. Note how well these sites are predicted using the templates.

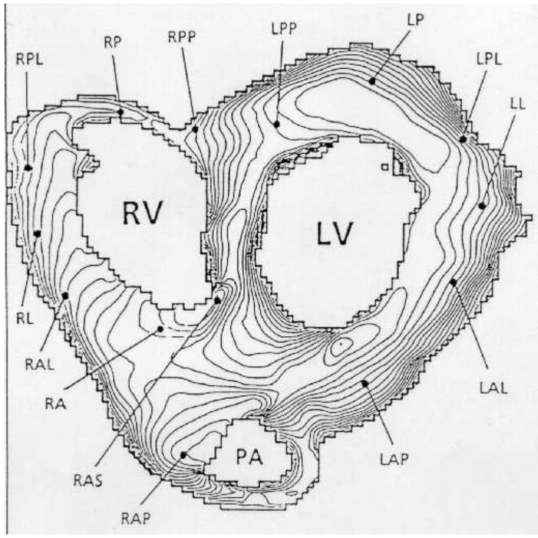

FIGURE 3.41: Top 20 Bassal sections of the ventricular haeart model used at Halifax. There were 14 preexcitation sites. The sections, which are 1 mm apart, are represented by smoothed contour lines to achieve a better rendering of the shape. Note that the ventricular structure is rid of all non-excitable tissues in the atrioventricular ring. RV = right ventricle; LV = left ventricle; PA = pulmonary artery; AP= anterior parseptal; AS - anterior septal; A - anterior, AL = anteropateral; L=lateral; PL = posterolateral; P = posterior; PP = posterior paraseptal

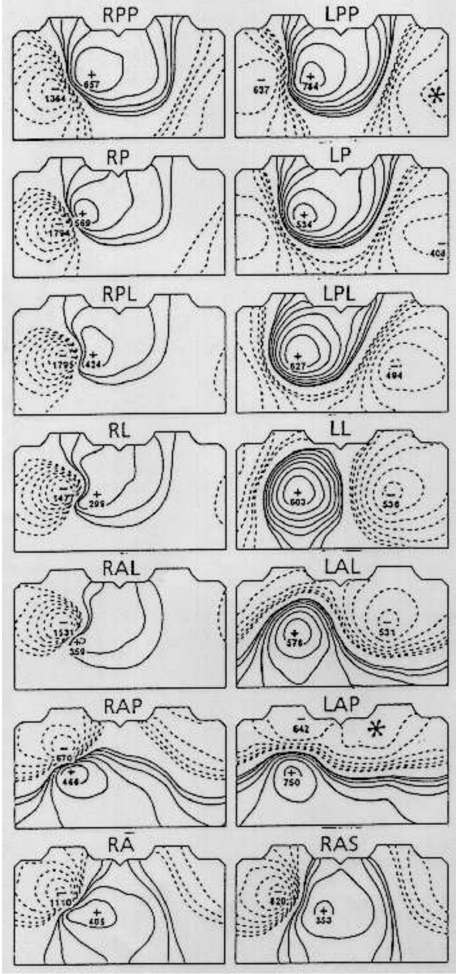

FIGURE 3.42: The simulated BSPMS at 40ms after the onset of stimulation which was individualy applied at the 14 preexcitation sites shown in Figure 3.41. The right and left borders of each map both correspond to the right mid-axillary line; the lower border corresponds to the waist. Isopotential lines progress logarithmically and the principal extrema have their amplitudes marked in microvolts

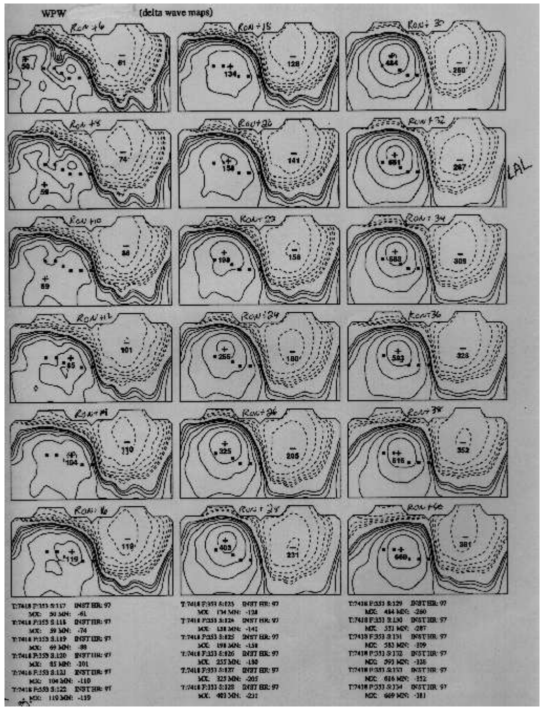

FIGURE 3.43: A real BSPM from a WPW patient. The accesory pathway is at LAL which is predicted using the template

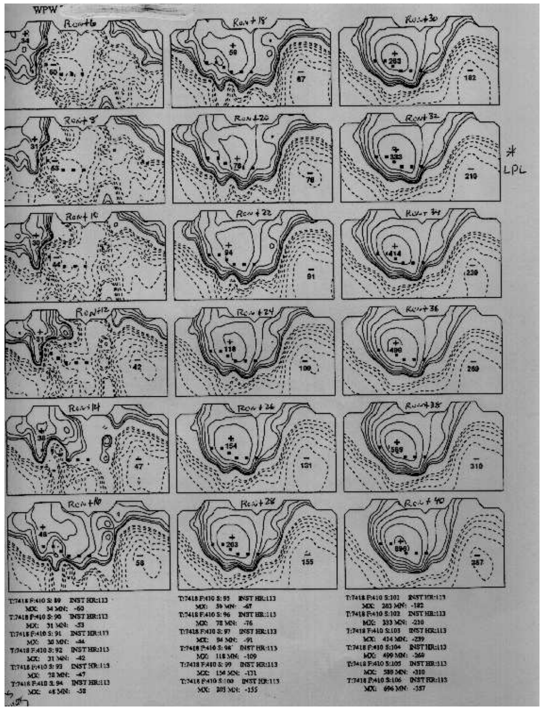

FIGURE 3.44: Real WPW map (b)

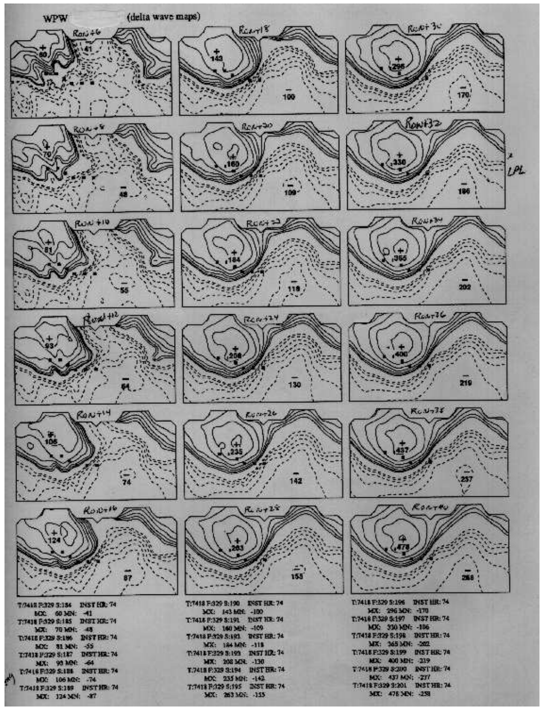

FIGURE 3.45: Real WPW map (c)

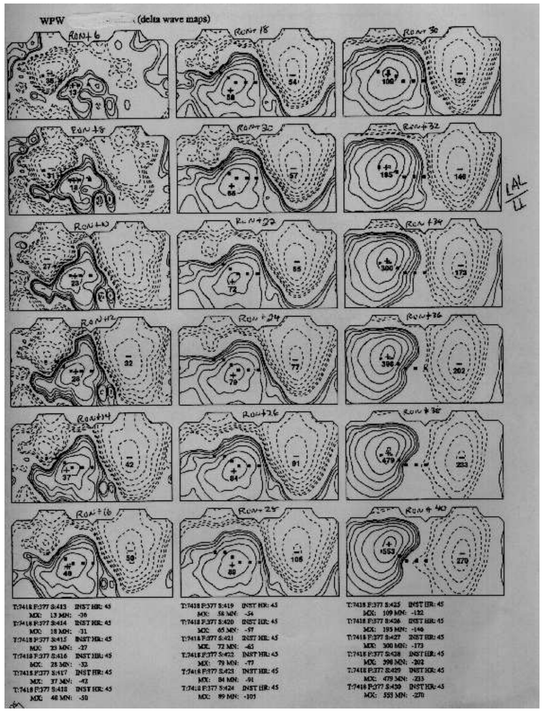

FIGURE 3.46: Real WPW map (d). The best template match was LAL and LL.

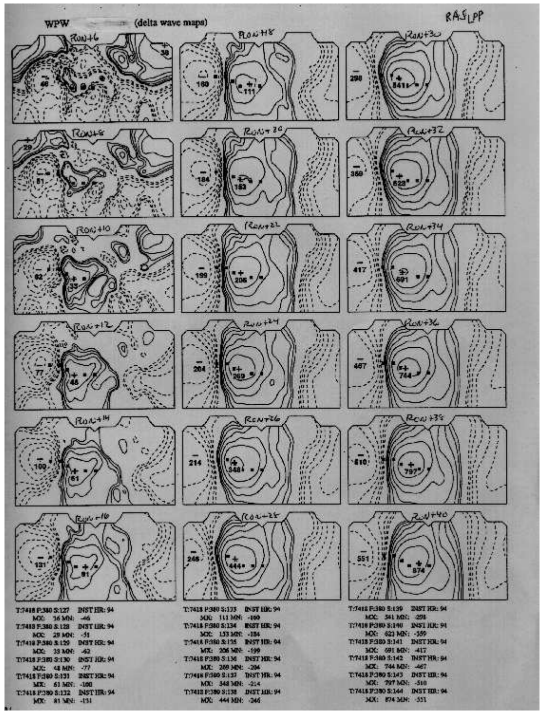

FIGURE 3.47: Real WPW map (e). The best template match was RAS and LPP

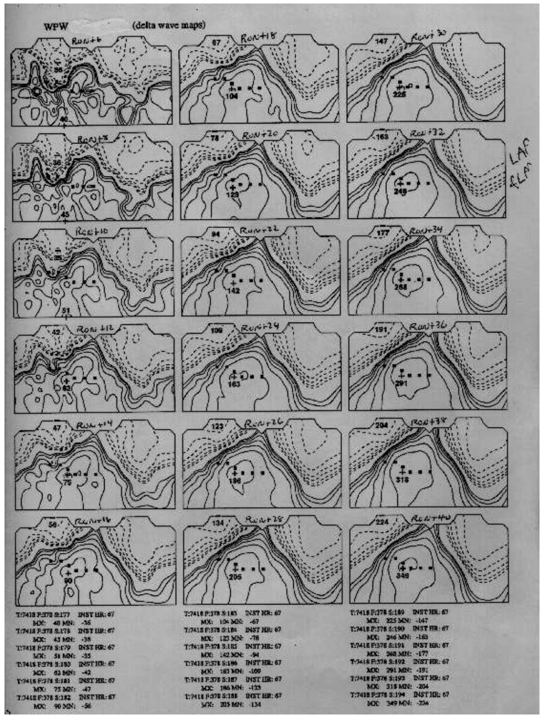

FIGURE 3.48: Real WPW map (f). There were 2 accesory pathways at LAP and LPP

3.8 The Forward and Inverse Problems of Electrocardiography

3.8.1 Introduction

The goal of non-invasive electrical imaging of the heart is to quantitatively reconstruct information about the electrical activity of the heart from densely sampled thoracic ECG signals.

Quantitative interpretation of the densely sampled data in terms of the underlying cardiac electrical activity is an inverse problem, and various mathematical algorithms have been developed over the years in an attempt to solve this electrical imaging problem e.g. (Barr & Spach 1978, Gulrajani, Roberge & Savard 1984, Martin, Pilkington & Morrow 1975, Oster & Rudy 1992). Unless the problem is posed in a particular manner this inverse problem is not uniquely determined i.e. there exist multiple cardiac electrical generator configurations that can give rise to the same thoracic ECG measurements. This non-uniqueness has hampered attempts at solving the inverse problem. Early approaches to the inverse problem overcame the non-uniqueness by modelling the heart as a combination of a small number of fixed or moving dipoles. It has been recognised that posing the problem in terms of trying to reconstruct epicardial potentials from the body surface potential recordings is uniquely determined. However, the reconstruction of epicardial potentials is ill-posed. This means that in the presence of noise (which always exists) a solution to the inverse problem produces a result which may bear no resemblance to that of the true electrical generator. The emergence of a general theory for such ill-posed problems (Tikhonov & Arsenin 1977) and the introduction of the ideas behind constraining the mathematical solutions has resulted in the large number of variants of the inverse algorithms in existence today in the electrical imaging area. However, since they are based on a generic approach, most of the modern algorithms fail to incorporate the underlying physiological processes governing the generation of the body surface potentials (namely an evolving wave of activation). Most of these algorithms also do not impose the constraints in a mathematically correct fashion (Greensite 2001, Greensite & Huiskamp 1998).

A New Approach

Another approach to the inverse problem is to pose the problem in terms of the underlying activation sequence (Huiskamp & van Oosterom 1988). This has significant advantages over the epicardial potential problem formulation, not least in that it deals directly with the underlying physiological process responsible for generating the body surface potentials. However, it introduces additionally difficulties in the modelling process (for instance the need to accurately model the entire heart instead of just modelling the epicardial surface). Because of this, and partly because of the fact that an appropriate algorithm for such a problem formulation had previously not been devised, this approach has not found much favour. However, a powerful new algorithm, based on this activation imaging approach has recently emerged (Greensite 2001, Huiskamp & Greensite 1997).

Both the epicardial and activation source formulations mentioned above have been recognised for twenty to thirty years but as of yet no clinically acceptable imaging techniques have resulted. The two major reasons for this are

1. Previously available mathematical methodologies for computation of the sources were not powerful enough.
2. Adequate procedures for verification of the accuracy of the images were not employed.

For each of the two source formulations there are now powerful imaging algorithms that have not previously been available, e.g. (Greensite 2001, Greensite & Huiskamp 1998, Huiskamp & Greensite 1997). There are also sufficient modelling techniques now available that when combined with these new algorithms should make it possible to produce myocardial electrical source images of sufficient stability and accuracy to be a useful adjunct in the clinical assessment of the heart. However, these new algorthims need to be quantitatively validated before teh clinical worth can be properly assessed.

In order to quantitatively validate the performance of the inverse procedures, one needs to compare any mathematical results against experimentally-obtained *invivo* data, in particular simultaneously recorded densely sampled body surface and cardiac potentials. This has rarely been attempted – rather the worth of various inverse procedures has often been judged by examining the performance on simulated data or in *in vitro* torso tank experiments. As far as is known, only two sets of *invivo* data have ever been collected, one in a chimpanzee (Spach, Miller III, Miller-Jones, Warren & Barr 1979) (in which no inverse solution was attempted) and one in a dog (Barr & Spach 1978). Neither set is currently available. Data from *in vitro* experiments from perfused canine hearts in a homogeneous cylindrical tank have been collected by Taccardi *et. al.* and are in use by that group and others (Oster & Rudy 1992, Oster, Taccardi, Lux, Ershler & Rudy 1997, Oster, Taccardi, Lux, Ershler & Rudy 1998).

We are currently performing experiments on pigs to provide the necessary *invivo* data to validate the new inverse procedures. We present here the details of the underlying theory behind the electrical imaging process and the porcine model development. We also illustrate how the procedure is to be applied in practice by producing an inversely-reconstructed cardiac surface activation map from simulated data.

3.9 Theory

The basic activation inverse algorithm is presented in Huiskamp and Greensite (Huiskamp & Greensite 1997). The procedure revolves around the identification of the critical points and times of the surface activation function (i.e. epi- and endocardial breakthrough/termination points and times) via the use of a modified MUSIC algorithm. To use this method on a given individual/animal requires the construction of an appropriate transfer function or mapping from the activation sequence to body surface potentials.

The proof of the activation imaging algorithm (Greensite 2001) uses source field relationships given in (Yamashita & Geselowitz 1985). These relationships employ a Green's function that takes into account the anisotropy of the myocardium. While the new imaging algorithm proved from these relationships is completely general, the initial use of it has been restricted to using the so-called double layer transfer matrices, which assume a homogeneous and isotropic heart muscle. The traditional construction of such a double-layer transfer matrix begins with the assumption of myocardial homogeneity and isotropy and the use of equations defining the potential due to a dipole in freespace (Cuppen & van Oosterom 1984). We prefer to investigate the transfer matrix construction from a boundary value problem point of view (e.g. from solving the bidomain equations) which avoids explicit reference to dipoles, and makes more explicit the anisotropic/isotropic distinction. This approach also generalises some of the identities presented in (Yamashita & Geselowitz 1985).

3.9.1 Transfer Matrices From A Boundary Value Problem Point of View

Let D_H be the domain of the heart, $S_H = \partial D_H$ (closed), ϕ_i the intracellular potential, ϕ_e the extracellular potential, ϕ_m the transmembrane potential ($= \phi_i - \phi_e$), ϕ the torso potential outside D_H and $\overline{G_i}$ and $\overline{G_e}$ the intracellular and extracellular conductivity tensors.

From bidomain theory we have inside D_H

$$\nabla \cdot ([\overline{G_i} + \overline{G_e}]\nabla \phi_e) = -\nabla \cdot (\overline{G_i}\nabla \phi_m) \tag{3.1}$$

This is a Poisson equation for ϕ_e in which the source term is $-\nabla \cdot (\overline{G_i}\nabla \phi_m)$.

One can solve this partial differential equation using a weighted residuals approach. Let w be a (as-yet-unspecified) weighting function. Then, from weighted residuals

$$0 = \int_{D_H} \nabla \cdot ([\overline{G_i} + \overline{G_e}]\nabla \phi_e) w \, d\Omega + \int_{D_H} \nabla \cdot (\overline{G_i}\nabla \phi_m) w \, d\Omega \tag{3.2}$$

Using Green's theorem we get

$$0 = \int_{S_H} w[\overline{G_i} + \overline{G_e}]\nabla \phi_e \cdot n \, dS - \int_{D_H} [\overline{G_i} + \overline{G_e}]\nabla \phi_e \cdot \nabla w \, d\Omega + \int_{D_H} \{\nabla \cdot (\overline{G_i}\nabla \phi_m)\} w \, d\Omega \tag{3.3}$$

where n is the unit outward normal.

Applying Green's theorem again, one gets

$$\begin{aligned} 0 = & \int_{S_H} w[\overline{G_i} + \overline{G_e}]\nabla \phi_e \cdot n \, dS - \int_{S_H} \phi_e[\overline{G_i} + \overline{G_e}]\nabla w \cdot n \, dS \\ & + \int_{D_H} \nabla \cdot ([\overline{G_i} + \overline{G_e}]\nabla w)\phi_e \, d\Omega + \int_{D_H} \nabla \cdot (\overline{G_i}\nabla \phi_m) w \, d\Omega \end{aligned} \tag{3.4}$$

This is the standard boundary integral equation for Poisson's equation with a general source term. For the special case of the source being given by $-\nabla \cdot (\overline{G_i}\nabla\phi_m)$ we can apply a similar procedure to that above on this term i.e.

$$\begin{aligned}\int_{D_H} \nabla \cdot (\overline{G_i}\nabla\phi_m) w d\Omega &= \int_{S_H} w\overline{G_i}\nabla\phi_m \cdot n dS - \int_{D_H} \overline{G_i}\nabla\phi_m \cdot \nabla w d\Omega \\ &= \int_{S_H} w\overline{G_i}\nabla\phi_m \cdot n dS - \int_{S_H} \phi_m\overline{G_i}\nabla w \cdot n dS \\ &\quad + \int_{D_H} \nabla \cdot (\overline{G_i}\nabla w)\phi_m d\Omega \end{aligned} \tag{3.5}$$

Inserting Equation (3.5) into Equation (3.4) we get

$$\begin{aligned} 0 &= \int_{S_H} w[\overline{G_i} + \overline{G_e}]\nabla\phi_e \cdot n dS - \int_{S_H} \phi_e[\overline{G_i} + \overline{G_e}]\nabla w \cdot n dS \\ &\quad + \int_{D_H} \nabla \cdot ([\overline{G_i} + \overline{G_e}]\nabla w)\phi_e d\Omega + \int_{S_H} w\overline{G_i}\nabla\phi_m \cdot n dS \\ &\quad - \int_{S_H} \phi_m\overline{G_i}\nabla w \cdot n dS + \int_{D_H} \nabla \cdot (\overline{G_i}\nabla w)\phi_m d\Omega \end{aligned} \tag{3.6}$$

which is a generalisation of Equation 31 of (Yamashita & Geselowitz 1985).

This Equation (3.6) is general - no assumptions (apart from differentiability and integrability) have been made on $w, \overline{G_i}$ or $\overline{G_e}$. In (Yamashita & Geselowitz 1985), they assumed that w was a Green's function satisfying

$$\nabla \cdot ([\overline{G_i} + \overline{G_e}]\nabla w) + \delta(P) = 0 \tag{3.7}$$

and

$$[\overline{G_i} + \overline{G_e}]\nabla w \cdot n = 0 \text{ on } S_B \tag{3.8}$$

where $\delta(P)$ is the Dirac delta distribution centred at a point P and S_B is the surface of the torso. This resulted in the removal of the first volume integral in Equation (3.6).

In practice, such a Green's function for the heart cannot be found analytically, since both $\overline{G_i}$ and $\overline{G_e}$ are in general anisotropic and inhomogeneous. If one assumes that they are homogeneous then both conductivity tensors can be represented by a constant 3×3 matrix, which is diagonal in the coordinate system defined by the myocardial fibres and sheets. The fibre/sheet orientation in the heart is very complex, which means that it is not possible in practice to solve Equation (3.7) analytically even under the assumption of homogeneity, or even equal anisotropy ratios (i.e. $G_i = kG_e$ where k is a constant). This is true irrespective of whether we strive for a proper Green's function (i.e. impose Equation (3.8)) or merely look for a freespace Green's function (also known as a fundamental solution) which is a solution of Equation (3.7) with zero boundary conditions at infinity (i.e. the no-flux condition on S_B is ignored).

If one assumes further that the domain is isotropic in both the extra and intracellular domains, then one can apply a standard boundary element procedure to Equation (3.6). For this we take w to be the freespace Green's function i.e. a solution of

$$\nabla \cdot ([(1+k)G_e]\nabla w) + \delta(P) = 0 \tag{3.9}$$

subject to zero boundary conditions at infinity. In three-dimensions, the solution of this equation is

$$w = \frac{1}{4\pi(1+k)G_e R} \tag{3.10}$$

where R is the distance measured from P.

With w defined as above, we get, for P inside D_H

$$\begin{aligned}\int_{D_H} \nabla \cdot ([\overline{G_i} + \overline{G_e}]\nabla w)\phi_e d\Omega &= \int_{D_H} \nabla \cdot ([(1+k)G_e]\nabla w)\phi_e d\Omega \\ &= -\phi_e(P) \end{aligned} \tag{3.11}$$

and

$$\begin{aligned}\int_{D_H} \nabla \cdot (\overline{G_i}\nabla w)\phi_m d\Omega &= \int_{D_H} \nabla \cdot (kG_e\nabla w)\phi_m d\Omega \\ &= -\frac{k}{k+1}\phi_m(P) \qquad (3.12)\end{aligned}$$

So Equation (3.6) becomes

$$\begin{aligned}0 = &\int_{S_H} w(1+k)G_e\nabla\phi_e \cdot ndS - \int_{S_H}\phi_e(1+k)G_e\nabla w\cdot ndS - \phi_e(P) \\ &+ \int_{S_H} wkG_e\nabla\phi_m\cdot ndS - \int_{S_H}\phi_m kG_e\nabla w\cdot ndS - \frac{k}{k+1}\phi_m(P) \qquad (3.13)\end{aligned}$$

The equation of more interest is the case for when $P \in S_H$ (i.e. P is on the boundary of the domain). To derive this equation, consider P at a smooth point on the boundary of D_H and construct a hemispherical region of radius ε centred at P . Let $D_H^{'}$ be the extended region (i.e. D_H with the hemispherical region). Then P is interior to $D_H^{'}$ so Equation (3.13) is valid with S_H replaced by $\partial D_H^{'}$. One now considers this equation in the limit as $\lim_{\varepsilon\downarrow 0}$. If Γ_ε is the boundary of the hemispherical region, and $\Gamma_{-\varepsilon}$ the boundary of that part of D_H that is outside the hemisphere (so $\partial D_H^{'} = \Gamma_\varepsilon \cup \Gamma_{-\varepsilon}$) then we find that

$$\begin{aligned}\lim_{\varepsilon\downarrow 0}\int_{\Gamma_\varepsilon}\phi_e(1+k)G_e\nabla w\cdot ndS &= \lim_{\varepsilon\downarrow 0} -\frac{1}{4\pi R^2}2\pi R^2\phi_e(\gamma) \\ &= -\frac{\phi_e(P)}{2} \qquad (3.14)\end{aligned}$$

where γ is some point on the hemisphere of radius ε (the mean value theorem has been applied).

Similarly

$$\begin{aligned}\lim_{\varepsilon\downarrow 0}\int_{\Gamma_\varepsilon}\phi_m kG_e\nabla w\cdot ndS &= \lim_{\varepsilon\downarrow 0} -\frac{k}{k+1}\frac{1}{4\pi R^2}2\pi R^2\phi_m(\gamma) \\ &= -\frac{k}{k+1}\frac{\phi_m(P)}{2} \qquad (3.15)\end{aligned}$$

It can also be shown that

$$\lim_{\varepsilon\downarrow 0}\int_{\Gamma_\varepsilon} w(1+k)G_e\nabla\phi_e\cdot ndS = 0 \qquad (3.16)$$

and

$$\lim_{\varepsilon\downarrow 0}\int_{\Gamma_\varepsilon} wkG_e\nabla\phi_m\cdot ndS = 0 \qquad (3.17)$$

As $\lim_{\varepsilon\downarrow 0}$ and $\lim_{\Gamma_{-\varepsilon}\downarrow S_H}$ and while the integrands are singular, the integrals exist in the standard sense, so one can write

$$\lim_{\varepsilon\downarrow 0}\int_{\Gamma_{-\varepsilon}}(\text{each integrand})dS = \int_{S_H}(\text{same integrand})dS \qquad (3.18)$$

Using Equation (3.14) to Equation (3.18) together with Equation (3.13) we obtain the general boundary integral equation

$$\begin{aligned}c(P)\phi_e(P) + \frac{k}{k+1}c(P)\phi_m(P) + \int_{S_H}\phi_e(1+k)G_e\nabla w\cdot ndS + \int_{S_H}\phi_m kG_e\nabla w\cdot ndS \\ = \int_{S_H} w(1+k)G_e\nabla\phi_e\cdot ndS + \int_{S_H} wkG_e\nabla\phi_m\cdot ndS \qquad (3.19)\end{aligned}$$

where

$$c(P) = \begin{cases} 1 \text{ if } P \in D_H^0 \\ \frac{1}{2} \text{ if } P \in S_H \text{ and } S_H \text{ smooth at } P \\ \frac{\text{internal solid angle}}{4\pi} \text{ if } P \in S_H \text{ and } S_H \text{ not smooth at } P \\ 0 \text{ if } P \text{ outside } D_H \end{cases} \qquad (3.20)$$

Equation (3.19) relates ϕ_e and ϕ_m at a point to the values of $\phi_e, \phi_m, \nabla\phi_e\cdot n$ and $\nabla\phi_m\cdot n$ everywhere on S_H. On S_H, $\nabla\phi_m\cdot n$ is 0 since transmembrane potentials are confined to the heart, which removes the last integral in Equation (3.19).

Outside the heart, the governing equation is

$$\nabla \cdot (\sigma \nabla \phi) = 0 \tag{3.21}$$

and this can be solved using a coupled Finite Element/Boundary Element procedure (Pullan 1996). Continuity of (extra-cellular) potential and current across the myocardial boundaries provides the links between Equation (3.21) and Equation (3.19). In the usual way, one can discretise the boundaries of all regions involved, and assemble the following matrices

$$\begin{pmatrix} \text{all coefficients} \\ \text{of potentials from} \\ \text{Equation (3.19)} \\ \text{and Equation (3.21)} \end{pmatrix} \begin{pmatrix} \boldsymbol{\phi_m} \\ \boldsymbol{\phi_e^h} \\ \boldsymbol{\phi_e^1} \\ \cdot \\ \cdot \\ \boldsymbol{\phi_e^N} \end{pmatrix} = \begin{pmatrix} \text{all coefficients} \\ \text{of currents from} \\ \text{Equation (3.19)} \\ \text{and Equation (3.21)} \end{pmatrix} \begin{pmatrix} (1+k)G_e \frac{\partial \boldsymbol{\phi_e^H}}{\partial n} \\ \sigma^1 \frac{\partial \boldsymbol{\phi_e^1}}{\partial n} \\ \cdot \\ \cdot \\ \sigma^N \frac{\partial \boldsymbol{\phi_e^i}}{\partial n} \end{pmatrix} \tag{3.22}$$

where

- N is a number of regions outside the heart
- $\boldsymbol{\phi_e^i}$ is a vector of nodal values of ϕ_e in region i
- $\boldsymbol{\phi_m}$ is a vector of nodal values of ϕ_m in the heart
- $\boldsymbol{\phi_e^H}$ is a vector of nodal values in the heart
- σ^i is the conductivity in region i

The coefficient matrices include all the continuity constraints. Also, since $\dfrac{\partial \boldsymbol{\phi_m}}{\partial n}$ is 0 on S_H, this term is not present in Equation (3.22). It is worth noting that the coefficients of $\boldsymbol{\phi_m}$ in Equation (3.19) are just $\frac{k}{k+1}$ times the coefficients of $\boldsymbol{\phi_e}$ in that equation. Use of this fact allows one to speed up the assembly of Equation (3.22)

Equation (3.22) above can be considered to be an implicit relationship between $\boldsymbol{\phi_m}$ and the torso potentials $\boldsymbol{\phi_B}$. To construct an explicit transfer matrix A from $\boldsymbol{\phi_m}$ to $\boldsymbol{\phi_B}$ one simply needs to set $\boldsymbol{\phi_m}$ to be the vector $\boldsymbol{e_k}$ (i.e. a unit vector that is zero everywhere except at the k^{th}

position) and solve Equation (3.22). The resulting solution for $\boldsymbol{\phi_B}$ will correspond to the k^{th} column of A (since $\boldsymbol{\phi_B} = A\boldsymbol{\phi_m}$). Alternatively one can construct a transfer matrix from $\boldsymbol{\phi_m}$ to $\boldsymbol{\phi_e^H}$ by suitable rearrangement of Equation (3.22).

No mention has yet been made of the singular nature or otherwise of Equation (3.22). The physical problem being solved suggests that Equation (3.22) will be singular if $\boldsymbol{\phi_m}$ is the only variable to be specified, since no potential reference has been given. The system can either be solved in a least-squares sense, or a technique such as deflation used.

The construction of the transfer matrix described above has assumed homogeneity and isotropy in the heart muscle from Equation (3.6) onwards. It is worth pointing out that the assumptions of homogeneity and isotropy is not required to use the activation imaging algorithm of (Huiskamp & Greensite 1997). It is also possible to construct a transfer matrix relating activation times to torso potentials without these assumptions as well. However, the transfer matrix construction under anisotropic conditions becomes significantly more difficult. The bidomain equations (or a weak form of them, such as that given in Equation (3.6) have to be solved throughout the heart (using some volume-discretisation procedure representing the full myocardial-fibre orientation) and coupled to solutions of Equation (3.21) outside the heart. Work on this is progressing (Pullan & Buist 1998) but at this stage homogeneity and isotropy is assumed.

3.9.2 Myocardial Inverse Procedure

The activation inverse procedure that is used here is described in detail in (Huiskamp & van Oosterom 1988). We include here a summary of that method for completeness.

The basic idea behind the new approach stems from the observation that when an evolving cardiac activation wavefront intersects the epicardial surface a *hole* develops in the wavefront. This is a signifcant change to the topology of the wavefront and thischange is reflected in the surface potential recordings. If $\tau(x)$ is defined to be the activation time on S_H, then these breakthough points are critical points of of $\tau(x)$; that is $\nabla\tau(x') = 0$ when $\boldsymbol{x'}$ is a breakthough point, i.e. $\tau(x')$ is the breakthough or critical point.

This critical point observation leads, after much mathematical work (Greensite 1995), to the two following important results,

1. $\boldsymbol{x'}$ is a critical point of $\tau(x)$ with critical time $\tau(x') \Longleftrightarrow A(x', y)$ is in the space spanned by the spatial eigenfunctions of ϕ_B, where $\boldsymbol{A}(\boldsymbol{x}, \boldsymbol{y})$ is the transfer matrix from ϕ_m to ϕ_B.

2. With all critical points of $\tau(x)$ determined, the computation of $\tau(x)$ (on both the epicardial and endocardial surfaces) is a well-posed problem.

The key assumption required to prove the first point above is that ϕ_m is modelled as a uniform step jump across the wavefront. i.e.

$$\phi_m = a + bH(t - \tau(x)) \tag{3.23}$$

This assumption is not a practical restriction for normal hearts but it does provide a measure of the expected spatial resultion of this approach.

To compute the critical points and times we require both the signal matrix, $\Phi(\boldsymbol{y}, t)$, recorded from surface electrodes where $t \in [0, T]$ and y is a point on the torso surface and the transfer matrix from ϕ_m to ϕ_B, $\boldsymbol{A}(\boldsymbol{x}, \boldsymbol{y})$. To determine the spactial eigen functions of $\Phi(\boldsymbol{y}, t)$ we used the singular value decomposition.

$$\Phi(\boldsymbol{y}, t) = U \Sigma V^T \quad \text{with an effective rank } R \tag{3.24}$$

Eigen functions corresponding to *small* singular values we discarded. These discarded eigenfunctions are assumed to represent only noise space.

A distance from signal space can be contructed by,

$$M_0^T(x) = \left(1 - \sum_{r=1}^{R} [a(x, y) \cdot U_r(y)]^2\right)^{-1} \tag{3.25}$$

where $a(x, y) = \dfrac{\boldsymbol{A}(\boldsymbol{x}, \boldsymbol{y})}{\|\boldsymbol{A}(\boldsymbol{x}, \boldsymbol{y})\|_y}$.

This distance meaure greately exaggerates points $\boldsymbol{x}$ which are close to signal space. This (near) singularities in $M_0^T(x)$ has no singularities due to noise and error associated with $\boldsymbol{\Phi}$ and $\boldsymbol{A}$.

To find the activation times corresponding to these critical points, we contruct the functions,

$$M^+(x, t) = M_0^t(x) \tag{3.26}$$
$$M^-(x, t) = M_s uaht^T(x) \tag{3.27}$$

where $0 < t < T$. These two functions look at the distance from signal space where signal spaces are restricted to $[0, t]$ and $[t, T]$ respectively.

The zero-crossing function defined by,

$$Z(\boldsymbol{x}, t) = M^+(\boldsymbol{x}, t) - M^-(\boldsymbol{x}, t) \tag{3.28}$$

theoretically crosses zero at the critcal time and has a large gradient about zero.

With critical points and time identified, the process of determinging $\tau(x)$ everywhere is theoretically a well-posed problem. This process was formulated as a minimisation problem, where the objective was to minimise the difference between calculated torso potentials $\hat{\phi_B}$, and the measured potentials, ϕ_B. $\hat{\phi_B}$ was calculated using $\boldsymbol{A}(\boldsymbol{x}, \boldsymbol{y})$ and an initial guess of $\tau(x)$.

In practice, $Z(\boldsymbol{x}, t)$ provides a reasonable initial estimate of $\tau(x)$. Additional constraints on the optimisation process can be imposed, e.g. (Huiskamp & van Oosterom 1988) in which the surface Laplacian of the $\tau(x)$ is also minimised.

$$E(\tau(x)) = \left\|\phi_B - \hat{\phi_B}\right\|_2 + \lambda \cdot \mathfrak{L}(\tau(x)) \tag{3.29}$$

where λ is a parameter controlling the degree of regularisation imposed on the objective function and $\mathfrak{L}$ is the Laplacian of the activation field.

Also there are serveral possibilites for how the critical points are constrained, e.g. the critical points and times could be fixed or the critical points could be constrained to remain local maxima or minima of $\tau(x)$.

Bibliography

Barr, R. C. & Spach, M. S. (1978), 'Inverse calculation of QRS-T epicardial potentials from body surface potential distributions for normal and ectopic beats in the intact dog', *Circ. Res.* **42**, 661–675.

Beeler, G. W. & Reuter, H. (1977), 'Reconstruction of the action potential of ventricular myocardial fibres', *J. Physiol.* **268**, 177–210.

Berne, R. M. & Levy, M. N., eds (1988), *Physiology*, second edn, Mosby, 11830 Westline Industrial Drive, St. Louis, Missouri 63146.

Caulfield, J. B. & Borg, T. K. (1979), 'The collagen network of the heart', *Lab. Invest.* **40**(3), 364–372.

Clerc, L. (1976), 'Directional differences of impulse spread in trabecular muscle from mammalian heart', *J. Physiol.* **255**, 335–346.

Cuppen, J. & van Oosterom, A. (1984), 'Model studies with the inversely calculated isochrones of ventricular depolarization', *IEEE Trans. Biomed. Eng.* **31**, 652–659.

DiFrancesco, D. & Noble, D. (1985), 'A model of cardiac electrical activity incorporating ionic pumps and concentration changes', *Phil. Trans. R. Soc. Lond.* **B307**, 353–398.

Durrer, D., van Dam, R. T., Freud, G. E., Janse, M. J., Meijler, F. L. & Arzbaecher, R. C. (1970), 'Total excitation of the isolated human heart', *Circulation* **21**, 899–912.

Greensite, F. (1995), 'Remote reconstruction of confined wavefront propagation', *Inverse Problems* **11**, 361–370.

Greensite, F. (2001), *Computational Inverse Problems in Electrocardiography*, Advances in Computational Biomedicine, WIT Press, Southampton, UK, chapter Myocardial Activation Imaging, pp. 143–190.

Greensite, F. & Huiskamp, G. (1998), 'An improved method for estimating epicardial potentials from the body surface', *IEEE Trans. Biomed. Eng.* **45**, 98–104.

Gulrajani, R. M., Roberge, F. A. & Savard, P. (1984), 'Moving dipole inverse ECG and EEG solutions', *IEEE Trans. Biomed. Eng.* **31**(12), 903–910.

Henriquez, C. S. (1993), 'Simulating the electrical behaviour of cardiac tissue using the bidomain model', *Crit. Rev. Biomed. Eng.* **21**, 1–77.

Hill, A. V. (1938), 'Heat of shortening and the dynamic constants of muscle', *Proc. Roy. Soc. B* **126**, 136–195.

Hodgkin, A. L. & Huxley, A. F. (1952), 'A quantitative description of membrane current and its application to conductance and excitation in nerve', *J. Physiol.* **117**, 500–544.

Hort, W. (1957), 'Mikrometrische Untersuchungen an verschieden weiten Meerschweinchenherzen', *Verhandl. Deut. Ges. Kreislaufforsch* **23**, 343–346.

Huiskamp, G. & Greensite, F. (1997), 'A new method for myocardial activation imaging', *IEEE Trans. Biomed. Eng.* **44**, 433–446.

Huiskamp, G. J. & van Oosterom, A. (1988), 'The depolarization sequence of the human heart surface computed from measured body surface potentials', *IEEE Trans. Biomed. Eng.* **35**(12), 1047–1059.

Hunter, P. J., McNaughton, P. A. & Noble, D. (1975), 'Analytical models of propagation in excitable cells', *Prog. Biophys. Molec. Biol.* **30**(2/3), 99–144.

Hunter, P. J., Nielsen, P. M. F., Smaill, B. H., Le Grice, I. J. & Hunter, I. W. (1993), An anatomical heart model with applications to myocardial activation and ventricular mechanics, *in* Pilkington, Loftis, Thompson, Woo, Palmer & Budinger (1993), chapter 1, pp. 3–26.

Hunter, P. J., Smaill, B. H., Nielsen, P. M. F. & Le Grice, I. J. (1996), A mathematical model of cardiac anatomy, *in* S. Panfilov & A. V. Holden, eds, 'Computational Biology of the Heart', Wiley, chapter 11.

Huxley, A. F. (1957), 'Muscle structure and theories of contraction', *Prog. Biophys. Chem.* **7**, 255–318.

Huxley, A. F. & Simmons, R. M. (1971), 'Proposed mechansim of force generation in striated muscle', *Nature* **233**, 533–538.

Katz, A. M. (1992), *Physiology of the Heart*, 2nd edn, Raven Press, Ltd., 1185 Avenue of the Americas, New York 10036.

Krassowska, W. & Neu, J. C. (1994), 'Effective boundary conditions for syncytial tissues', *IEEE Trans. Biomed. Eng.* **41**(2), 143–150.

Le Grice, I. J. (1992), A Finite Element Model of Myocardial Structure: Implications for Electrical Activation in the Heart, PhD thesis, The University of Auckland, New Zealand.

Le Grice, I. J., Smaill, B. H., Chai, L. Z., Edgar, S. G., Gavin, J. B. & Hunter, P. J. (1995), 'Laminar structure of the heart: Ventricular myocyte arrangement and connective tissue architecture in the dog', *Am. J. Physiol.* **269**(38), H571–H582.

Luo, C. & Rudy, Y. (1991), 'A model of the ventricular cardiac action potential: Depolarisation, repolarisation, and their interaction', *Circ. Res.* **68**, 1501–1526.

Luo, C. & Rudy, Y. (1994), 'A dynamic model of the cardiac ventricular action potential: I. Simulations of ionic currents and concentration changes', *Circ. Res.* **74**(6), 1071–1096.

MacCallum, J. B. (1900), 'On the muscular architecture and growth of the ventricles of the heart', *Johns Hopkins Hosp. Rep.* **9**, 307–335.

MacKenna, D. A. (1994), Contribution of the Extracellular Collagen Matrix to the Mechanics of Ventricular Myocardium, PhD thesis, U.C.S.D.

Mall, F. P. (1911), 'On the muscular architecture of the ventricles of the human heart', *Am. J. Anat.* **11**(3), 211–266.

Marieb, E. N. (1992), *Human Anatomy and Physiology*, The Benjamin/Cummings Publishing Company Inc., Menlo Park, California.

Martin, R. O., Pilkington, T. C. & Morrow, M. (1975), 'Statistically constrained inverse electrocardiography', *IEEE Trans. Biomed. Eng.* **22**, 487–492.

McLean, M. R. & Prothero, J. (1987), 'Coordinated three-dimensional reconstruction from serial sections at macroscopic and microscopic levels of resolution; the human heart', *Anat. Rec.* **219**, 434–439.

McLean, M. R., Ross, M. A. & Prothero, J. (1989), 'Three-dimensional reconstruction of the myofiber pattern in the fetal and neonatal mouse heart', *Anat. Rec.* **224**, 392–406.

Miller, III, W. T. & Geselowitz, D. B. (1978), 'Simulation studies of the electrocardiogram I. The normal heart', *Circ. Res.* **43**(2), 301–314.

Nielsen, P. M. F. (1987), The Anatomy of the Heart: A Finite Element Model, PhD thesis, The University of Auckland, New Zealand.

Nielsen, P. M. F., Le Grice, I. J., Smaill, B. H. & Hunter, P. J. (1991), 'Mathematical model of geometry and fibrous structure of the heart', *Am. J. Physiol.* **260**(Heart Circ. Physiol. 29), H1365–H1378.

Oster, H. & Rudy, Y. (1992), 'The use of temporal information in the regularization of the inverse problem of electrocardiography', *IEEE Trans. Biomed. Eng.* **39**, 65–75.

Oster, H., Taccardi, B., Lux, R., Ershler, P. & Rudy, Y. (1997), 'Noninvasive electrocardiographic imaging. Reconstruction of epicardial potentials, electrograms, and isochrones and localization of single and multiple electrocardiac events', *Circulation* **96**, 1012–1024.

Oster, H., Taccardi, B., Lux, R., Ershler, P. & Rudy, Y. (1998), 'Electrocardiographic imaging. Noninvasive characterization of intramural myocardial activation from inverse-reconstructed epicardial potentials and electrograms', *Circulation* **97**, 1496–1507.

Pilkington, T. C., Loftis, B., Thompson, J. F., Woo, S. L.-Y., Palmer, T. C. & Budinger, T. F., eds (1993), *High-Performance Computing in Biomedical Research*, CRC Press Inc.

Plonsey, R. & Barr, R. C. (1984), 'Current flow patterns in two-dimensional anisotropic bisyncytia with normal and extreme conductivities', *Biophys. J.* **45**, 557–571.

Plonsey, R. & Barr, R. C. (1987), 'Mathematical modelling of electrical activity of the heart', *J. Electrocardiol.* **20**(3), 219–226.

Pollard, A. E., Hooke, N. & Henriquez, C. S. (1993), Cardiac propagation simulation, *in* Pilkington et al. (1993), chapter 12, pp. 319–358.

Pullan, A. J. (1996), 'A high-order coupled finite element/boundary element torso model', *IEEE Trans. Biomed. Eng.* **43**(3), 292–298.

Pullan, A. J. & Buist, M. L. (1998), The effect of external tissue impedance on extracellular potentials, *in* 'Electrocardiology '98. Proceedings of the XXV International Congress on Electrocardiology', World Scientific, Singapore, pp. 85–88.

Rogers, J. M. & McCulloch, A. D. (1994), 'A collocation-Galerkin finite element model of cardiac action potential propagation', *IEEE Trans. Biomed. Eng.* **41**(8), 743–757.

Schmitt, O. H. (1969), Biological information processing using the concept of interpenetrating domains, *in* K. N. Leibovic, ed., 'Information Processing in the Nervous System', Springer-Verlag, New York.

Skouibine, K., Trayanova, N. & Moore, P. (1999), 'Anode/cathode make and break phenomena during defibrillation: Does electroporation make a difference', *IEEE Trans. Biomed. Eng.* **46**, 769–777.

Smaill, B. H. & Hunter, P. J. (1991), Structure and function of the diastolic heart: Material porperties of passive myocardium, *in* L. Glass, P. J. Hunter & A. D. McCulloch, eds, 'Theory of Heart', Springer-Verlag, New York, pp. 1–29.

Spach, M. S. & Heidlage, J. F. (1993), A multidimensional model of cellular effects on the spread of electrotonic currents and on propagating action potentials, *in* Pilkington et al. (1993), chapter 11, pp. 289–317.

Spach, M. S., Miller III, W. T., Miller-Jones, E., Warren, R. B. & Barr, R. C. (1979), 'Extracellular potentials related to intracellular potentials during impulse conduction in anisotropic cardiac muscle', *Circ. Res.* **45**, 188–204.

Streeter, Jr., D. D. (1979), Gross morphology and fibre geometry of the heart, *in* R. M. Berne, N. Sperelakis & S. R. Geigert, eds, 'Handbook of Physiology (Section2: The Cardiovascular System. Vol. 1: The Heart)', Am. Physiol. Soc., Williams and Wilkins Company, Baltimore, chapter 4, pp. 61–112.

Streeter, Jr., D. D. & Bassett, D. L. (1966), 'An engineering analysis of myocardial fiber orientation in pig's left ventricle in systole', *Anat. Rec.* **155**, 503–511.

Streeter, Jr., D. D., Spotnitz, H. M., Patel, D. P., Ross, Jr., J. & Sonnenblick, E. H. (1969), 'Fibre orientation in the canine left ventricle during diastole and systole', *Circ. Res.* **24**, 339–347.

Tikhonov, A. & Arsenin, V. (1977), *Solution of ill-posed problems*, John Wiley & Sons, Washington, D.C.

Tung, L. (1978), A Bidomain Model for Describing Ischemic Myocardial D-C Potentials, PhD thesis, M.I.T., Boston, MA.

van Capelle, F. J. L. & Durrer, D. (1980), 'Computer simulation of arrhythmias in a network of coupled excitable elements', *Circ. Res.* **47**, 454–466.

Waller, A. D. (1887), 'A demonstration on man of electromotive changes accompanying the heart's beat', *J. Physiol.* **8**, 229–34.

Weidmann, S. (1970), 'Electrical constants of trabecular muscle from mammalian heart', *J. Physiol.* **210**, 1041–1054.

Yamashita, Y. & Geselowitz, D. (1985), 'Source-field relationships for cardiac generators on the heart surface based on their transfer coefficients', *IEEE Trans. Biomed. Eng.* **32**(11), 964–970.